Stony Brook University

The official electronic file of this thesis or dissertation is maintained by the University Libraries on behalf of The Graduate School at Stony Brook University.

Strong Electronic Correlations in Manganese Pnictide Compounds

A Dissertation Presented

by

Daniel McNally

to

The Graduate School

in Partial Fulfillment of the Requirements

for the Degree of

Doctor of Philosophy

in

Physics

Stony Brook University

December 2015

Stony Brook University

The Graduate School

Daniel McNally

We, the dissertation committee for the above candidate for the Doctor of Philosophy degree, hereby recommend acceptance of this dissertation.

Meigan Aronson – Dissertation Advisor
Professor, Department of Physics and Astronomy

Mengkun Liu – Chairperson of Defense
Assistant Professor, Department of Physics and Astronomy

John Parise
Professor, Department of Geosciences and Department of Chemistry

Philip Allen
Professor, Department of Physics and Astronomy

Gabriel Kotliar
Board of Governor's Professor, Department of Physics and Astronomy
Rutgers, The State University of New Jersey

This dissertation is accepted by the Graduate School.

Charles Taber
Dean of the Graduate School

Abstract of the Dissertation

Strong Electronic Correlations in Manganese Pnictide Compounds

by

Daniel McNally

Doctor of Philosophy

in

Physics

Stony Brook University

December 2015

Electron-electron interactions must be considered to understand the electronic ground states of many crystalline solids. The work presented here addresses the effects of electronic correlation in several manganese pnictide compounds. These results contribute to our understanding of the conditions under which high temperature superconductivity and spin liquid behavior can occur.

First, we find that the intra-atomic Hunds coupling between electrons is crucial for the stabilization of an insulating ground state in LaMnPO and $BaMn_2As_2$, which are isostructural to the parent compounds of the high temperature iron-based superconductors. Second, we find that competing inter-atomic exchange interactions frustrate the long range magnetic order in the corrugated honeycomb lattice compound $CaMn_2Sb_2$. Finally, we find signatures of an orbitally selective Mott phase in $LaMn_xSb_2$.

To arrive at these results, we performed and analyzed inelastic neutron scattering, x-ray and neutron diffraction, transport, specific heat and magnetization measurements on bulk single crystals and powders that we synthesized. We also collaborated extensively with groups that performed optical spectroscopy measurements on single crystals that we provided and electronic structure calculations on input crystal structures that we provided.

iii

Contents

List of Figures

List of Tables

Chapter 1

Introduction

1.1 Strongly Correlated Systems

Electron-electron interactions must be considered to understand the ground states of many different compounds, in particular 3d, 4d or 5d transition metal compounds, and compounds containing 4f (lanthanides) or 5f electrons (actinides). In these systems, the band theory for independent electrons that classifies materials into metals and insulators fails dramatically [1]. For example, according to independent electron band theory, the transition metal oxide NiO should be metallic as the d band of the nickel is partially filled [2]. However, experiments show that NiO is most definitely insulating. Electron-electron interactions governed by the Coulomb interaction U must be taken into account to understand why NiO is insulating. These materials are called Mott insulators [3]. The Hubbard Hamiltonian frames the problem of correlated electrons as a lattice of sites with a competition between the onsite Coulomb repulsion U and kinetic hopping between sites t ($\propto$ bandwidth W) (see Figure 1.1). Approximate solutions of this Hamiltonian can successfully account for the metal-insulator transition in many systems where independent electron band theory fails as outlined in Figure 1.1.

The appearance of magnetic ordering in a compound often indicates that electron-electron interactions are important. It has been well established that the parent compounds of the copper oxide high temperature superconductors (HTSC), e.g. La_2CuO_4, are antiferromagnetic Mott insulators [1]. The introduction of chemical dopants suppresses the long range antiferromagnetic order and reveals a superconducting state, e.g. $La_{1.85}Sr_{0.15}CuO_4$ (see Figure 1.2a). The ground state properties of the cuprates are well described by a single orbital Hubbard model, as the Cu^{2+} atoms are in a d^9 configuration and a Jahn-Teller-type distortion of the oxygen octahedron co-ordinating the
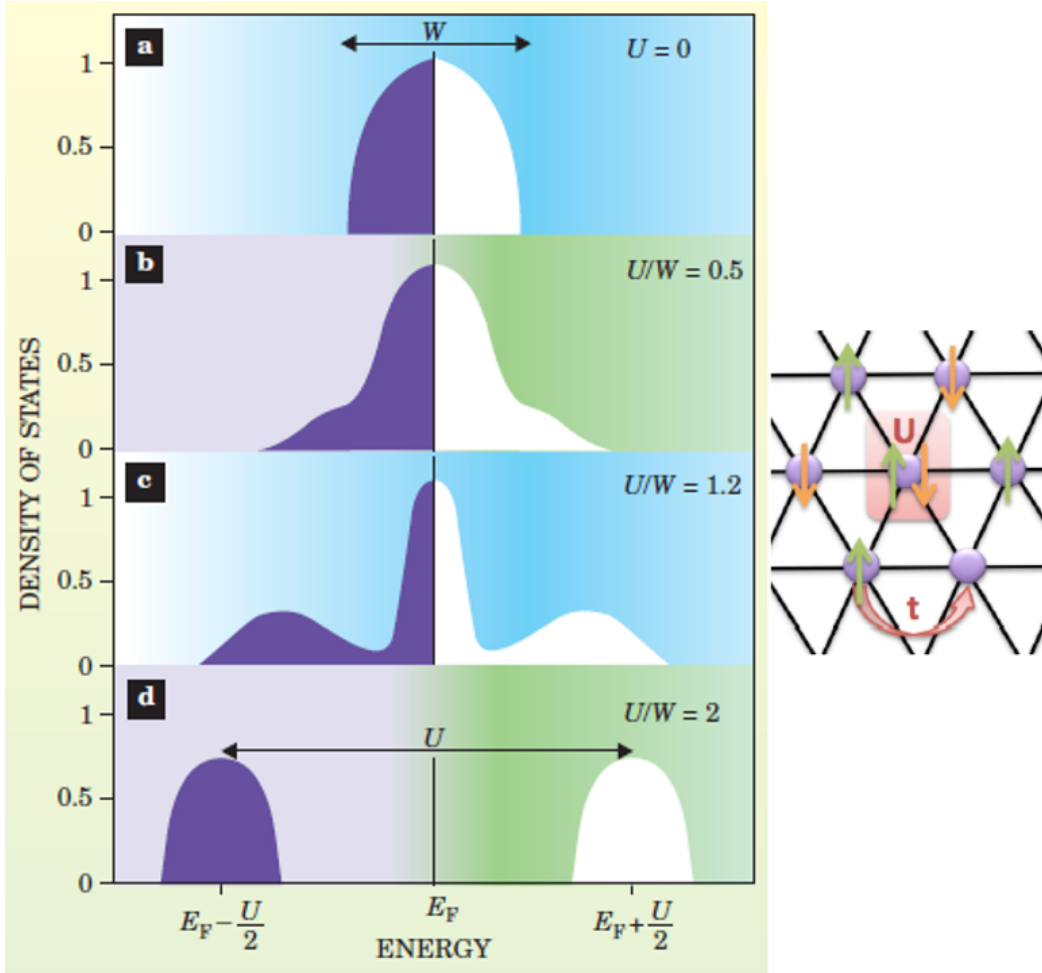
Figure 1.1: (left) The density functional theory plus dynamical mean field theory (DFT+DMFT) [4] solution of the single orbital Hubbard model can well account for the properties of systems where electron-electron interactions, defined by the ratio of the Coulomb interaction to electron bandwidth U/W, are important. (a) Density of states (DOS) for a system of non-interacting electrons. (b) DOS for weak electron-electron interactions. The narrowing of the peak can be described by Fermi liquid theory of mass enhanced quasiparticles. (c) DOS for stronger electron-electron interactions. Upper and lower Hubbard bands originate from local atomic excitations and there is a quasiparticle peak near the Fermi level (d) For sufficiently strong electronic correlations a band gap opens at the Fermi level and a metal-insulator transition has occurred. These spectral features may be observed by photoemission experiments. Figure reproduced from [5] (right) Triangular lattice showing the onsite Coulomb interaction U and the kinetic hopping t ∝ W. Figure reproduced from [6]

Cu lifts the degeneracy of the e_g orbital so that the half-filled $d_{x^2-y^2}$ orbital dominates near the Fermi level.

The paradigm of doping a Mott insulator to realize HTSC was challenged by the discovery of superconductivity in iron pnictide compounds, whose parent compounds are antiferromagnetic metals, e.g. LaFeAsO [7]. The introduction of chemical dopants suppresses the long range antiferromagnetic order and reveals a superconducting state, e.g. $LaFeAsO_{0.89}F_{0.11}$ (see 1.2b). The importance of electron-electron interactions in iron pnictide compounds is a topic of much current debate [8]. The temperature-doping phase diagram presented in Figure 1.2 shows similar behavior between iron and copper based superconductors. However, an important distinction between these materials is that multiple orbitals may contribute to the ground state properties of the iron pnictides as Fe^{2+} is nominally in a d^6 configuration, with experiments and theory showing that the three t_{2g} orbitals dominate the Fermi level. In such multiorbital systems Hund's coupling, discussed further below, can lead to orbital decoupling and different degrees of correlation in different orbitals: the closer an orbital is to half-filling, the more correlated it will be [9]. Thus one or more orbitals may be in a Mott insulating phase while the other orbitals become metallic. This is called orbitally selective Mottness and allows for the co-existence of both weakly and strongly correlated electrons in iron pnictide compounds(Figure 1.3).
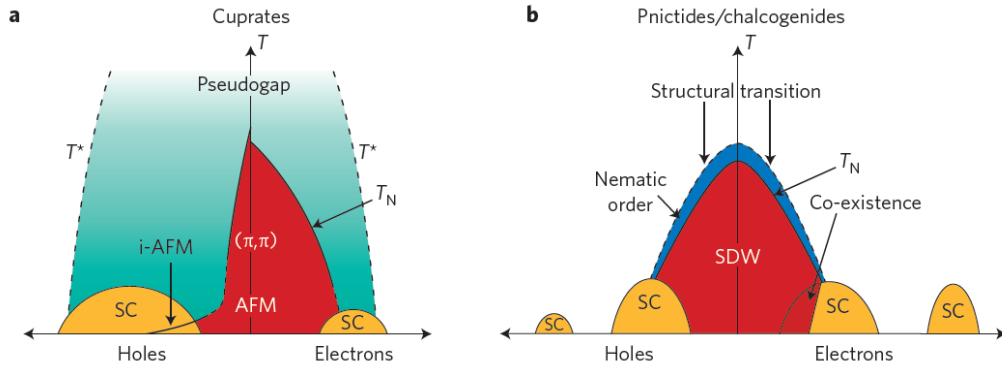
Figure 1.2: Phase diagram of cuprate (a) and iron pnictide (b) superconductors. Superconductivity emerges out an antiferromagnetic case for both classes of high temperature superconductors. However, the parent compounds of the cuprates are Mott insulators while the parent compounds of the iron pnictides are Hund's metals. Figure reproduced from [10].

3
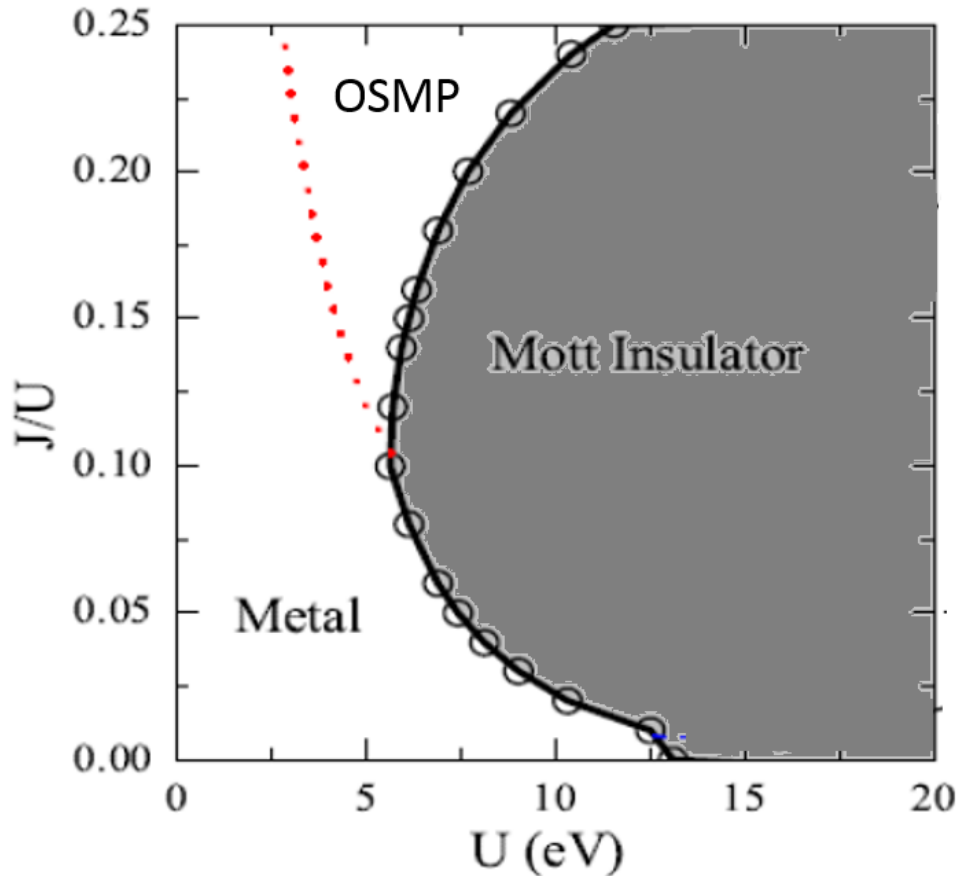
Figure 1.3: Phase diagram for a three band model with four electrons and band fillings (1, 1.5, 1.5) where the band degeneracy is lifted by adjusting the crystal field within slave spin mean field theory. The presence of Hund's coupling J in multi-orbital systems can lead to the emergence of an orbitally selective Mott phase (OSMP). Figure reproduced from [11].

In this thesis, I examine the interplay between the electronic, magnetic and structural properties of antiferromagnetic manganese compounds that are isostructural with the iron pnictide compounds discussed above. To provide further background for the results that will be presented later in this thesis, I now briefly describe the magnetic interactions between electrons in solids. In particular, I emphasize how these interactions can lead to short and long range magnetic order, and the interplay between the spin, charge, orbital and lattice degrees of freedom in solids.

1.2   Hund's rules

The combination of angular momentum quantum numbers that minimize the energy of an isolated magnetic ion can be estimated by the empirical Hund's rules [12] given in order of decreasing importance as:

(1) The wavefunction of the ion should be arranged so as to maximize the total spin S.

(2) The wavefunction of the ion should be arranged so as to maximize the total orbital angular momentum L.

(3) The total angular momentum J = ||L - S|| if the shell is less than half-filled and J = ||L + S|| if the shell is more than half-filled. This rule is associated with spin-orbit coupling, which we shall not consider in this thesis although its physical effects have attracted considerable attention recently.

These empirical rules result from the minimization of the energy governed by the Coulomb interaction between electrons. The fluctuating moment $\mu_1 = g_J\sqrt{J(J+1)}$ (g_J is the Landé g-factor) calculated using Hund's rules yields very good agreement with experiment for 4f ions, whose orbitals are very localized. However, for the more extended orbitals in 3d ions the effect of the local crystal field environment is more important than the spin-orbit coupling and Hund's third rule is no longer valid. The crystal field effect leads to orbital quenching such that L = 0, $g_J = 2$ and $\mu_2 = 2\mu_B\sqrt{S(S+1)}$. With this modification, the magnetic ground states of 3d ions calculated using Hund's rules is in very good agreement with experiment as shown in Table 1.1.

ion	shell	S	L	J	μ_1	μ_{exp}	μ_2
Ti^{3+}, V^{4+}	$3d^1$	1/2	2	5/2	1.55	1.70	1.73
V^{3+}	$3d^2$	1	3	2	1.63	2.61	2.83
Cr^{3+}, V^{2+}	$3d^3$	3/2	3	3/2	0.77	3.85	3.87
Mn^{3+}, Cr^{2+}	$3d^4$	2	2	0	0	4.82	4.90
Fe^{3+}, Mn^{3+}	$3d^5$	5/2	0	5/2	5.92	5.82	5.92
Fe^{2+}	$3d^6$	2	2	4	6.70	5.36	4.90
Co^{2+}	$3d^7$	3/2	3	9/2	6.63	4.90	3.87
Ni^{2+}	$3d^8$	1	3	4	5.59	3.12	2.83
Cu^{2+}	$3d^9$	1/2	2	5/2	3.55	1.83	1.73
Zn^{2+}	$3d^{10}$	0	0	0	0	0	0

Table 1.1: The experimental values of the fluctuating moment μ_{exp} taken from measurements of paramagnetic salts. These values are in excellent agreement with those expected from Hund's rules when orbital quenching is considered

1.3 Hund's Coupling

While the appropriateness of Hund's rules in determining the magnetic ground states of localized ions has long been established, it is only more recently that the role of Hund's coupling in systems with extended hybridized orbitals, even displaying metallic behavior, has been considered. These studies of the electronic correlation effects associated with Hund's coupling have been motivated by the discovery of high temperature superconductivity when the antiferromagnetic metallic state of the layered multi-orbital iron pnictide compounds is suppressed by pressure or doping [13]. Density functional theory plus dynamical mean-field theory (DFT+DMFT) calculations have revealed that Hund's coupling is critical to understanding basic properties of the parent compounds, such as enhanced Pauli-like susceptibility and a linear temperature dependence of the resistivity (Figure 1.4).

The effect of Hund's coupling has been termed "Janus-faced" (two-faced) because while it enhances electronic correlations that would be expected to localize electrons, it actually promotes a metallic state in non half-filled multi-orbital systems [15]. To put this statement on a firmer footing I now show that the charge gap is decreased by Hund's coupling away from half filling following the outline and notation presented in [15]. The simplest model in which the Janus behavior occurs is the Hubbard-Kanamori model of three degenerate bands described by the Hamiltonian:
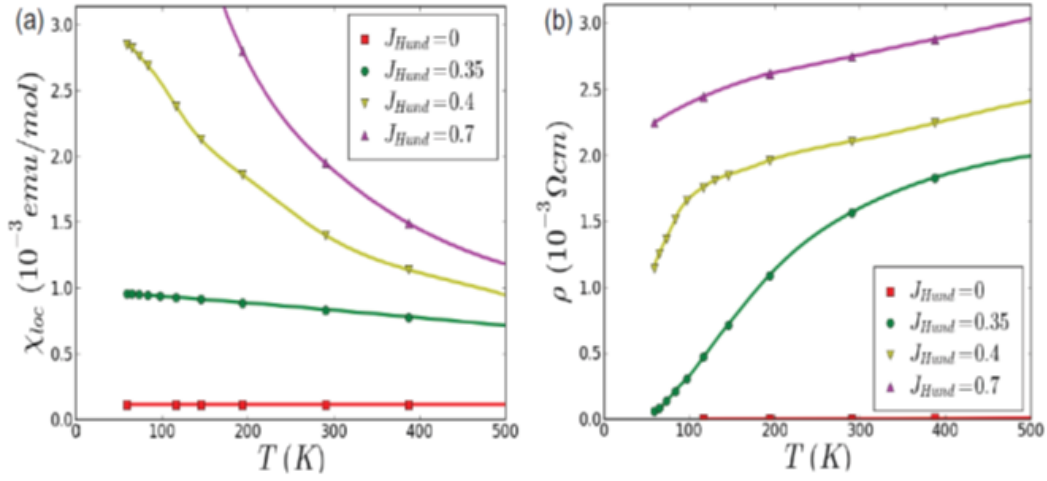
Figure 1.4: DFT+DMFT calculations show that Hund's coupling suppresses the coherence temperature for the formation of a Fermi liquid. (a) The introduction of Hund's coupling J_H transforms the static susceptility from a temperature-independent Pauli-like behavior ($J_H = 0$) to local moment Curie-Weiss-like behavior ($J_H = 0.7$). For intermediate values of J_H the system displays enhanced Pauli-like susceptibility. (b) In the presence of J_H the resistivity shows bad metal behavior with a small electron mean free path and a linear temperature dependence. These calculations are in reasonable agreement with experiments and emphasize the importance of Hund's coupling in multi-orbital magnetic systems. Figure reproduced from [14].

7

$$H_K = U \sum_m \hat{n}_{m\uparrow}\hat{n}_{m\downarrow} + U' \sum_{m\neq m'} \hat{n}_{m\uparrow}\hat{n}_{m'\downarrow} + (U' - J_H) \sum_{m<m',\sigma} \hat{n}_{m\sigma}\hat{n}_{m'\sigma}$$

$$- J_H \sum_{m\neq m'} d^\dagger_{m,\uparrow}d_{m,\downarrow}d^\dagger_{m',\downarrow}d_{m',\uparrow} + J_H \sum_{m\neq m'} d^\dagger_{m,\uparrow}d^\dagger_{m,\downarrow}d_{m',\downarrow}d_{m',\uparrow} \quad (1.1)$$

The first three terms involve density-density Coulombic interactions, between electrons with opposite spins in the same orbital m (U), opposite spins in different orbitals (U' = U - $2J_H$) and parallel spins in different orbitals (U - $3J_H$) where J_H is the Hund's coupling. The fourth and fifth terms are the exchange interaction and pair hopping.

Consider an isolated atom with N electrons and M orbitals. We are interested in the energetic cost Δ of changing the valence of two isolated atoms from their nominal electron numbers N to the state with N-1, N+1, i.e. transferring one of the electrons from one atom to the other. This corresponds to the difference of the affinity and ionization energies:

$$\Delta = [E_0(N + 1) - E_0(N)] - [E_0(N) - E_0(N - 1)] \quad (1.2)$$

where E_0 is the ground state energy of the atom. When the number of electrons N is less than the number of orbitals M, the ground state energy involves only the pairwise interactions between parallel spins:

$$E_0(N) = (U - 3J_H)N(N - 1)/2 \quad (1.3)$$

Hence U - $3J_H$ plays the role of the effective Hubbard interaction and the gap Δ is reduced

$$\Delta = U - 3J_H \ (N < M \text{ or } N > M) \quad (1.4)$$

with the expression for N > M resulting from particle-hole symmetry. In contrast, for a half-filled shell (N=M), the excited state with N + 1 = M + 1 involves one doubly-occupied orbital and has a higher energy. Considering each type of pair, that is parallel spins on different orbitals and antiparallel spins on same orbital and antiparallel spins on different orbitals, the expression for the ground state energy of the N + 1 excited state reads:

$$E_0(N + 1) = (U - 3J_H)M(M - 1)/2 + U + (U - 2J_H)(M - 1) \quad (1.5)$$

and the other energies may be calculated as before, yielding a gap

$$\Delta = U + (M - 1)J_H, \ N = M \quad (1.6)$$

It is clear that this Hubbard Hamiltonian predicts that Hund's coupling has a dramatic effect on the energetics of the gap, increasing the gap for half-filling while decreasing the gap for all other fillings.

1.4   Exchange Interaction

We now consider the interaction between two electrons on different atoms. The exchange symmetry requires that the eigenstates formed by the two electrons must be symmetric or antisymmetric under particle exchange. The difference between the resulting singlet (S=0) and triplet (S=1) states gives the strength of the direct exchange interaction between two electrons on different atoms occupying orbital states with wave function ψ_a and ψ_b:

$$J = -\int \psi_a^*(r_1)\psi_b^*(r_2)\frac{e^2}{r_{12}}\psi_a(r_2)\psi_b(r_1)dr_1dr_2 \qquad (1.7)$$

which measures the frequency with which two electrons exchange their orbital states. The Hamiltonian describing the interaction between the spin degree of freedom between electrons on different atoms can be written:

$$H = JS_1S_2 \qquad (1.8)$$

For localized orbitals the integral is always positive and the direct exchange coupling is negative J < 0, resulting in parallel, ferromagnetic alignment of spins. This is the origin of the first of Hund's empirical rules for electrons on an isolated atom presented above. However, the direct exchange mechanism usually cannot account for the experimentally observed co-operative magnetic behavior between collections of atoms. This is a consequence of the magnetic ions being too far apart in solids so that there is insufficient direct overlap between neighboring magnetic orbitals and the direct exchange interaction is very weak.

The indirect superexchange interaction is usually the dominant cause of antiferromagnetism in Mott insulators, such as the parent compounds of the cuprate superconductors. This interaction is mediated by the hybridization of the wave functions of the magnetic ions with those of an intervening anion (Figure 1.5). Because superexchange involves anion orbitals as well as the orbitals of the magnetic ions, it is a second order effect and can be derived from the Hubbard Hamiltonian with second order perturbation theory. The exchange energy is then the square of the hopping term divided by the Hubbard U:

$$J \approx \frac{t^2}{U} \tag{1.9}$$

In this case, the intersite exchange interaction mediated by superexchange can result in an antiferromagnetic configuration of spins (J > 0) that minimizes energy compared to a ferromagnetic configuration of spins or independently fluctuating spins as in a paramagnet. Thus, charge transport between atomic sites becomes energetically unfavorable and the exchange interaction should contribute to a charge gap $\Delta \approx$ J.

1.5   Long Range Magnetic Order

The exchange interactions presented above can apply between all neighboring localized atoms in a solid. In the limit U >> t the Hubbard Hamiltonian then reduces to the Heisenberg model:

$$H = \sum_{ij} J_{ij} S_i S_j \tag{1.10}$$

where J_{ij} is the exchange interaction between the ith and j^{th} spins. This can result in the formation of a long range magnetically ordered ground state when the exchange interaction is greater than the thermal fluctuations J > k_B T.

Generally, the existence of a periodic potential can open a charge gap in solids as in a band insulator such as silicon. The formation of a long range ordered magnetic state can modify the periodic potential that may then open a charge gap. This is the situation in a Slater insulator, such as $NaOsO_3$ [16] or perhaps Na_2IrO_3 [17].

Here we follow the outline and notation in [18] to show that a periodic potential can open a charge gap. In the nearly free electron approximation the lattice potential is treated as a perturbation. The starting point for the calculation is a set of electronic wavefunctions in the form of plane waves:

$$\psi_k^0 = e^{ik.r} \tag{1.11}$$

and the energies are E = $\hbar^2 k^2 / 2m$. In the presence of an external potential V(r) we search for the wavefunction in the form of a linear combination of plane waves:

$$\psi_k = \sum_G C_{k-G} e^{i(k-G)r} \tag{1.12}$$

where the G's are reciprocal lattice vectors. Inserting this wavefunction into
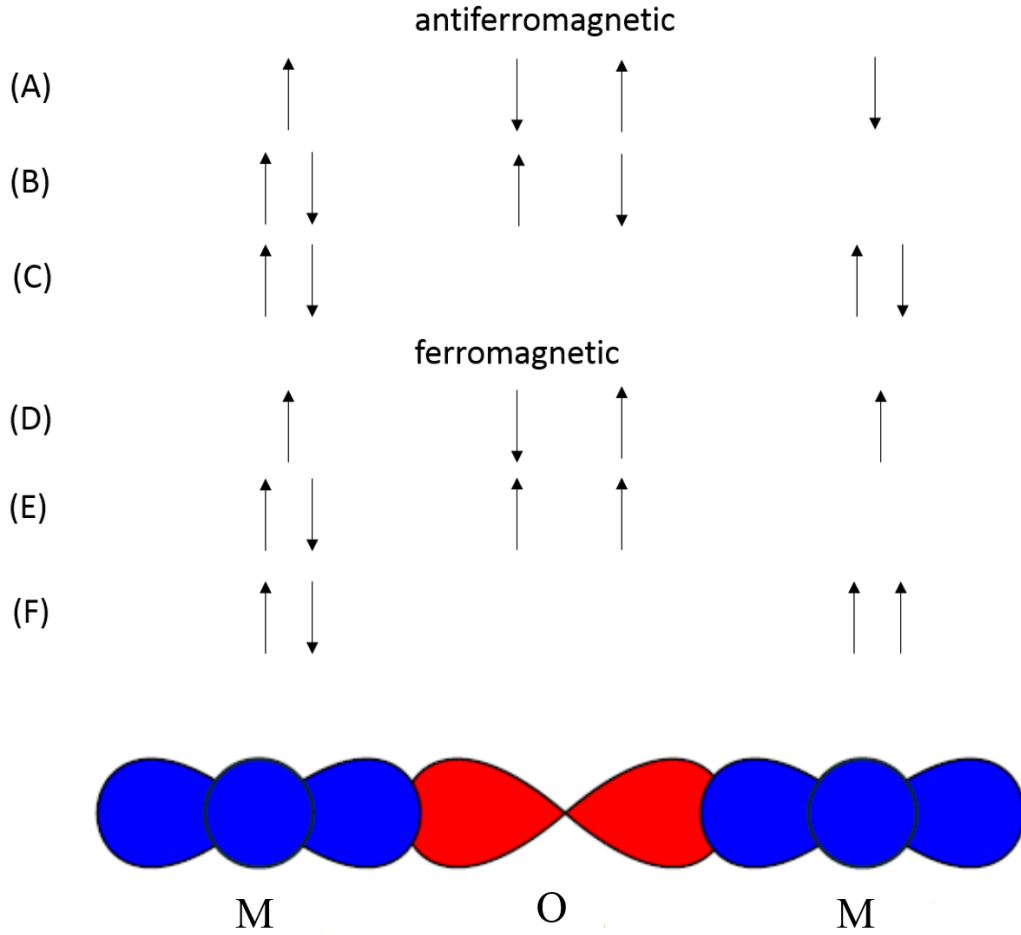
Figure 1.5: Superexchange mediated between the transition metal $d_{x^2-y^2}$ orbital and the oxygen p_x orbital [12]. Such a situation may arise in an octahedral environment where the crystal field increases the energy of the $d_{x^2-y^2}$ orbital relative to other d orbitals. The arrows show the spins of the four electrons and how they are distributed over the magnetic d orbital M and the anion 2p orbital O. Ground state antiferromagnetic coupling between magnetic ions such as in (A) can mix with excited configurations such as (B) and (C) thus delocalizing the electrons over the M-O-M unit and lowering the kinetic energy. Here, the kinetic energy is lowered because the electron's wavefunction becomes more spread out and thus its momentum, which is the spatial derivative of the wavefunction, decreases. If the moments on the M atoms are coupled ferromagnetically then the ground state (D) cannot mix with excited configurations like (E) and (F) because they are not allowed by the Pauli exclusion principle. The ferromagnetic configuration therefore costs more energy.

11

the Schrodinger equation leads to a set of linear equations:

$$[E - E(k - G)]C_{k-G} = \sum_{G'} C_{k-G'}V_{G-G'} \qquad (1.13)$$

where V_G is the Fourier component of the lattice potential V(r). If we assume that a weak periodic potential has its major effects only on those free electron levels whose wavevectors are close to ones at which Bragg reflections can occur, i.e. only the G-G' component of $V_{G-G'}$ is non-zero, the result is:

$$E^{\pm} = 1/2(E_k + E_{k-G_0}) \pm 1/2\sqrt{(E_k - E_{k-G_0})^2 + 4V_{G_0^2}} \qquad (1.14)$$

This is plotted in Figure 1.6.

The tight-binding model starts in the other extreme, where wavefunctions are localized on the atoms. The gap at the zone boundary for a weak potential in the tight binding model is the same as that for the nearly free electron model.
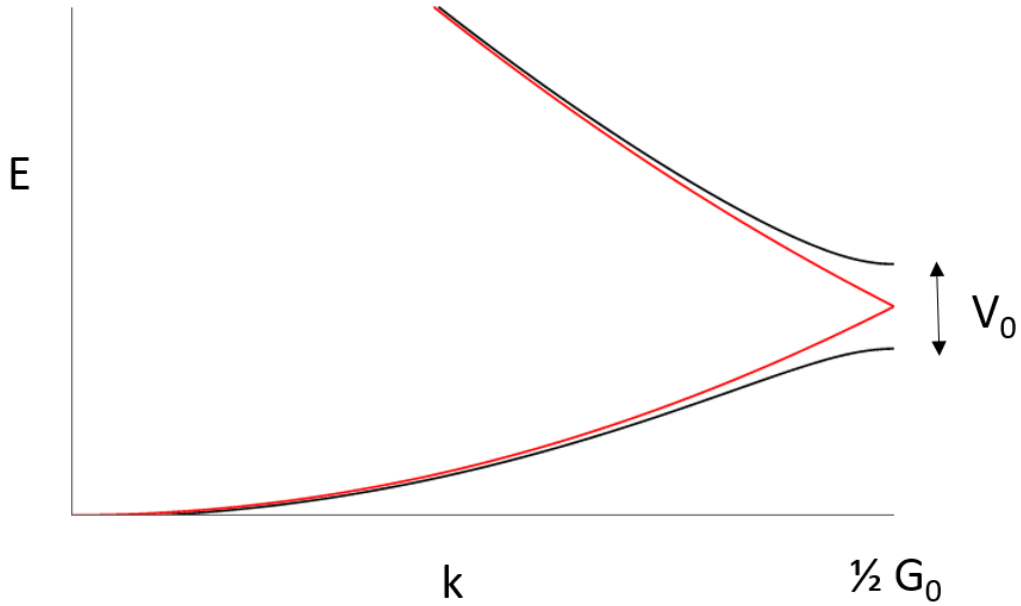
Figure 1.6: Energy bands for the free electron model (black) and the nearly free electron model with a periodic potential calculated using a linear combination of plane waves approach. A gap is opened at the zone boundary in the presence of a periodic potential.

1.6 Frustrated Magnetism

Sometimes, the presence of local moments and a sufficiently strong exchange interaction between them is not sufficient to drive long range magnetic order. An interaction-mediated frustration between spins, through geometric constraints or multiple exchange pathways, can create a large degeneracy of ground states among which the spins fluctuate. An example of the degeneracy of ground states present for a triangular lattice of spins is presented in Figure 1.7.

Magnetic frustration can lead to the formation of novel co-operative magnetic states with short range ordering of spins such as spin glass, spin ice or spin liquid. A spin glass may be defined as a random, mixed interacting (ferromagnetic and antiferromagnetic interactions) magnetic system characterized by a random, yet cooperative, freezing of spins at a well defined temperature T_f below which a highly irreversible, metastable frozen state appears but without magnetic long range ordering [12]. An example of a site-random spin glass system is the alloy $Cu_{1-x}Mn_x$ where small amounts of Mn atoms randomly occupy sites and the oscillatory RKKY interaction mediated by Cu ions yields mixed magnetic interactions between Mn sites. An example of a bond-random spin glass system is $Rb_2Cu_{1-x}Co_xF_4$ [19] where the superexchange pathway and hence the exchange interaction varies depending on whether Cu or Co occupy a site. Pyrochlore systems, such as $Ho_2Ti_2O_7$, may be considered as spin ice systems where there are local constraints on the directions of spins imposed by the geometry and exchange interactions on this lattice, known as the 'ice rules' [20]. Unlike in a spin glass or spin ice, for a spin liquid there is no local freezing of the spins and the spins continue to fluctuate down to the lowest measured temperatures, as in herbertsmithite [21].

The degree of magnetic frustration may be conveniently quantified as the ratio of the Weiss temperature θ_{CW} (or mean-field ordering temperature) to the ordering temperature T_N:

$$f = \frac{\theta_{CW}}{T_N} \tag{1.15}$$

where f is the frustration parameter [22].

1.7 Scope of this Work

In Chapters 3 and 4 of this thesis, we investigate the importance of electron-electron interactions in the manganese pnictide compounds LaMnPO and $BaMn_2As_2$, which are isostructural with the iron pnictide superconductors.
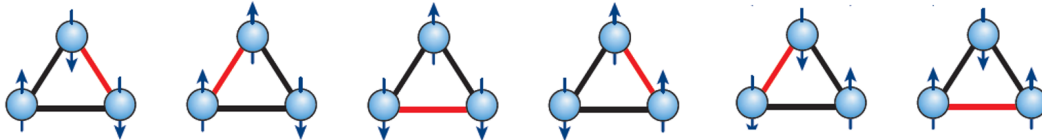
Figure 1.7: A triangle of antiferromagnetically coupled Ising spins is the simplest example of magnetic frustration. All three spins cannot be antiparallel. As a result, instead of the two ground states allowed by Ising symmetry, there are six degenerate ground states through which the spins fluctuate. These degeneracies can persist on 2D and 3D lattices, enhancing fluctuations and suppressing order. This produces exotic magnetic ground states such as spin glass, spin ice or spin liquid. Geometrical frustration is not a necessary condition: competing interactions may also enhance fluctuations and frustrate magnetic order.

Unlike their metallic Fe counterparts, both of these materials are antiferromagnetic insulators, like the cuprate parent compounds. We present a combined experimental and theoretical approach to determine the importance of electronic correlations for the formation of an insulating ground state in these two compounds. Inelastic neutron scattering is used to determine the magnitude of exchange interactions and the mean field ordering temperature in LaMnPO. Optical spectroscopy measurements at high temperature are used to show the charge gap persists even in the absence of exchange-coupled spins. We shared this experimental input with our theoretical colleagues who performed DFT+DMFT calculations that show Hund's coupling, as well as Coulomb U, is crucial to understand the origin of the charge gap in LaMnPO. We find similar behavior in $BaMn_2As_2$. This experimental work directly probes the interplay between the spin and charge degrees of freedom in these systems. Our results support the view that electronic correlations are important in both manganese and iron pnictide systems, with the strong Hund's coupling in these multi-orbital systems playing a critical role.

Our work on LaMnPO has been published as [23] and our work on $BaMn_2As_2$ has been published as [24].

In Chapter 5 of this thesis, we present inelastic neutron scattering measurements of the antiferromagnetic insulator $CaMn_2Sb_2$, in which the Mn atoms form a corrugated honeycomb lattice. At low temperature T = 5 K we observe sharp dispersive spin wave excitations. We model these spin waves using a Heisenberg model to determine the magnetic exchange interactions. Using these experimentally determined exchange parameters we situate $CaMn_2Sb_2$ on the theoretical phase diagram of the honeycomb lattice and find

14

it lies very close to a tricritical point, where three different types of magnetic order co-exist. We suggest that this proximity frustrates the magnetism in $CaMn_2Sb_2$ leading to a reduced magnetic ordering temperature.

Our work on $CaMn_2Sb_2$ has been published as [25].

In Chapter 6 of this thesis, we investigate the metallic state in $LaMn_xSb_2$, that is isostructural with the insulators LaMnPO and $BaMn_2As_2$ discussed above. Resistivity and specific heat measurements reveal a correlated metallic state with the presence of significant local moments inferred from high temperature magnetic susceptibility measurements. Neutron diffraction revealed these moments order in a canted magnetic structure below 130 K with an ordered moment of 2.9 μ_B at T = 5 K. The presence of strong electronic correlations in a metal with a large ordered moment is suggestive of an orbitally selective Mott phase. DFT+DMFT calculations revealed the Mn d_{xy} band is shifted away from the Fermi level when electronic correlations are included. This result supports our experimental findings and hints at the importance of orbital selectivity via Hund's coupling in multi-orbital systems.

Chapter 2

Experimental Methods

Most of the experiments presented here were performed on single crystals of compounds that were prepared using the flux method. We first present an overview of the flux growth technique and then outline the application of this method to the preparation of single crystals of multinary manganese pnictide compounds.

2.1   Flux Growth

The description presented here largely follows that of [26] and references therein. To synthesize a multinary single crystal compound (product) from starting materials (reactants), necessary conditions must be provided to minimize the Gibbs free energy G = H - TS of the desired product, making it an equilibrium phase. One approach is to heat the reactants, which serves to increase the energy of the system and to promote mixing, thus increasing the enthalpy H and entropy S until a liquid state is reached (Figure 2.1a). Slow cooling this liquid results in an entropy decrease until a solid phase precipitates out of the melt. The composition of the solid phase is a function of the initial fractions of the reactants and the temperature T(Figure 2.1b). Often, the melting temperature of the reactants is prohibitively large or the reactants melt incongruently, such that the solid decomposes into a mixture of a solid and liquid, each with a different composition to that of the original solid (see Figure 2.1c, point B). These difficulties may be overcome by the use of an appropriate eutectic 'flux' to dissolve the reactants at low temperature (see Figure 2.1c, point A) or by finding a congruent melting point (see Figure 2.1c, point C). A good flux allows for reasonable diffusivity, does not contaminate the product as inclusions or chemical substitutions, and is easy to remove.

Various pieces of apparatus are required for the implementation of the
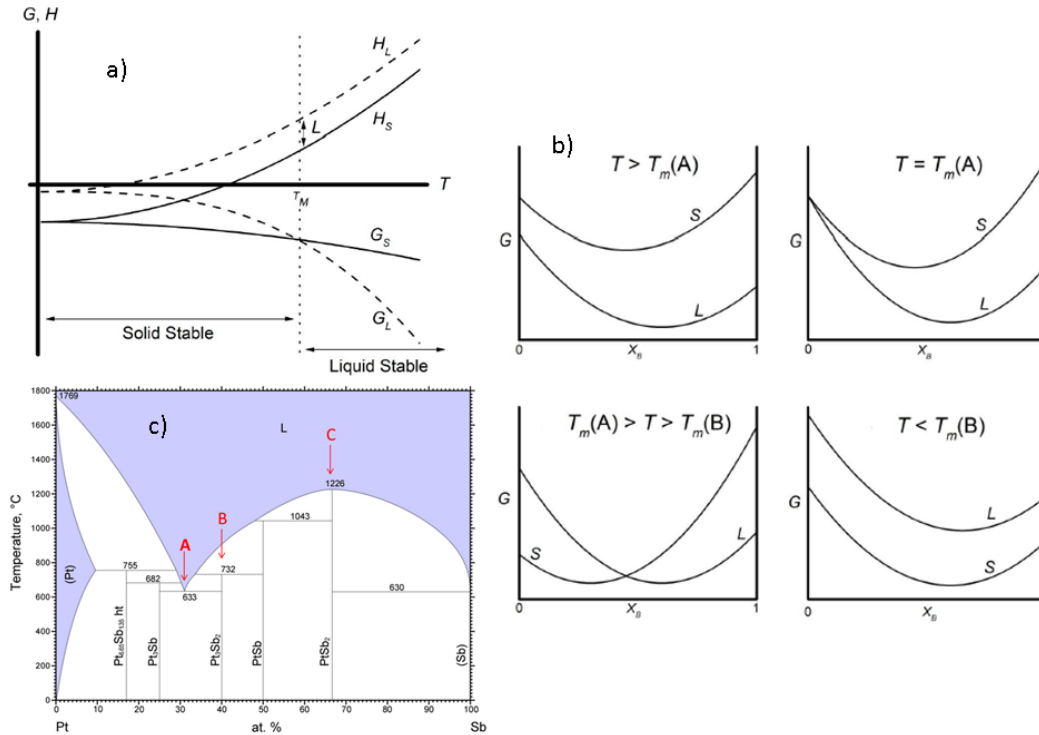
Figure 2.1: a) Gibbs free energy G = H - TS and enthalpy H as a function of temperature T. The liquid phase has a larger entropy and is favorable at higher temperatures. b) Gibbs energy G as a function of composition for different temperatures. Figures a) and (b) are reproduced from [26] c. The binary phase diagram of platinum and antimony. Eutectic point is a minima in the liquid region marked A. Point of incongruent melting is indicated by B. Here, a solid decomposes on heating to a two-phase mixture of solid and liquid, each with a different composition to that of the original solid. Congruent melt from a homogeneous solid to a homogeneous liquid is marked C. Figure c) reproduced from online resource Springer Materials

flux growth technique (Figure 2.2). Starting materials are purchased directly from Alfa Aesar and Sigma-Aldrich, used as received, all with a stated purity higher than 99.9%. Materials are mixed using a mortar and pestle and/or pelletized using a hydraulic press. This work involves the use of a glove box if oxygen or moisture sensitivity is an issue. Materials are loaded into an appropriate non-reactive vessel (e.g. α-Al_2O_3, tantalum) and sealed under gas in the glove box or left open to air. Often, an evacuated container is desirable in which case the materials, perhaps already in an auxilliary vessel, are loaded into a fused quartz ampoule. The quartz ampoule is held in rubber tubing and evacuated using a rotary pump and back-filled using Ar gas. The quartz ampoule is then sealed under vacuum or partial pressure of Ar using an oxyhydrogen torch. With the materials in an appropriate container, a temperature cycle is performed to transform these reactants into our desired product. Furnaces with silicon carbide heating elements can reach temperatures as high as 1500 °C, but syntheses using fused quartz are usually performed below the devitrification temperature ≈ 1200°C. Excess flux is decanted by removing the container from the furnace above the flux melting temperature and spinning in a centrifuge or removed using an appropriate etch such as HCl for many metals.

2.1.1   LaMnPO

Molten salt fluxes are used to synthesize many metal-oxide single crystals [27]. The use of a binary combination of NaCl and KCl reduces the melting point of these salts to 650 °C, lowers the viscosity, and allows us to synthesize single crystals of LaMnPO (Figure 2.3). We found the optimal recipe for growing LaMnPO to be La:MnO:InP:(NaCl+KCl) = 5:5:5:80 (atomic ratios). These starting materials were placed in an alumina crucible and sealed in an evacuated quartz tube under argon, that was then heated to 1100 °C in 4 hours, held at 1100°C for 4 hours and subsequently cooled to 800 °C in 57 hours. The crucible was then removed from the oven and the salt was washed away with water, revealing thin, dark plate-like crystals. Single crystal x-ray diffraction was performed on these crystals to confirm the previously reported ZrCu-SiAs structure [28]. A solid state reaction method was utilized to grow gram amounts of polycrystalline LaMnPO powder used for neutron scattering measurements. The optimal recipe was La:La_2O_3:MnP = 1:1:3. These starting materials were ground together and pressed into a pellet that was placed in an alumina crucible and sealed in an evacuated quartz tube under argon. The tube was then heated to 800 °C in 2 hours, held at 800°C for 24 hours, heated to 1100 °C in 2 hours, held at 1100°C for 24 hours and subsequently quenched in liquid nitrogen.
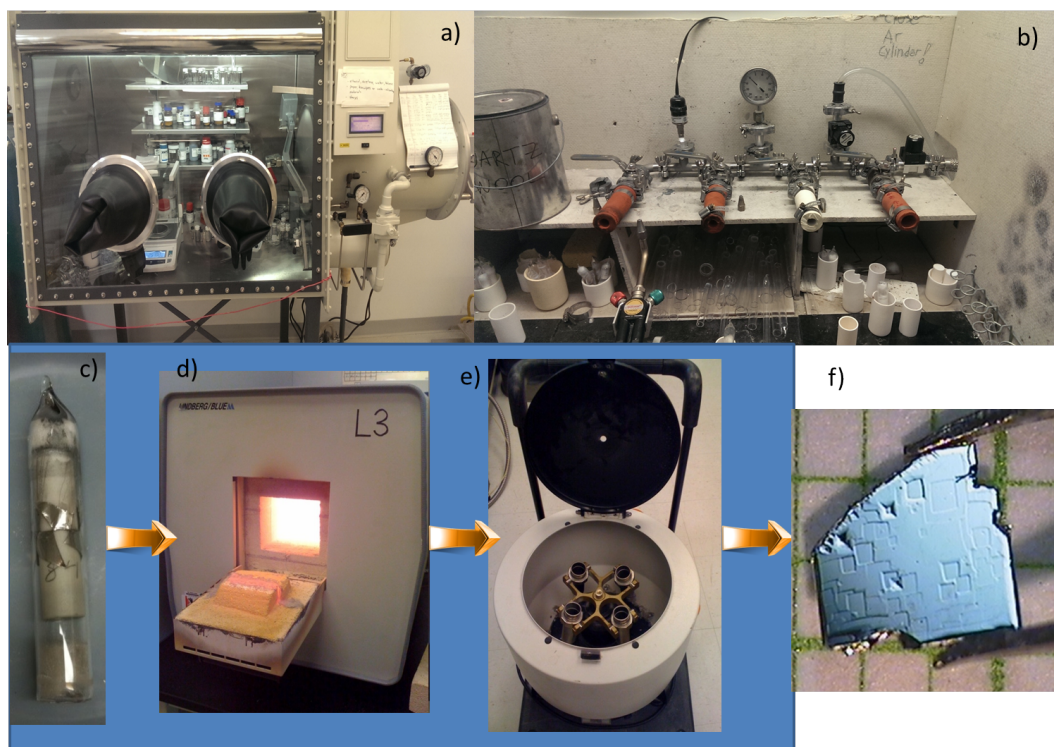
Figure 2.2: (a) Argon-filled glove box used to manipulate oxygen and moisture sensitive materials. (b) Vacuum manifold used to seal evacuated quartz tubes. (c) Alumina crucibles loaded in a sealed quartz tube with tantalum filter to separate flux from crystals while spinning in centrifuge. (d) Box furnace with SiC heating element to reach temperatures up to 1500°C. (e) Centrifuge to decant flux. Figure c), d), e) used with permission of J.W. Simonson. (f) Single crystal of YMn_2Ge_2 grown using In flux.
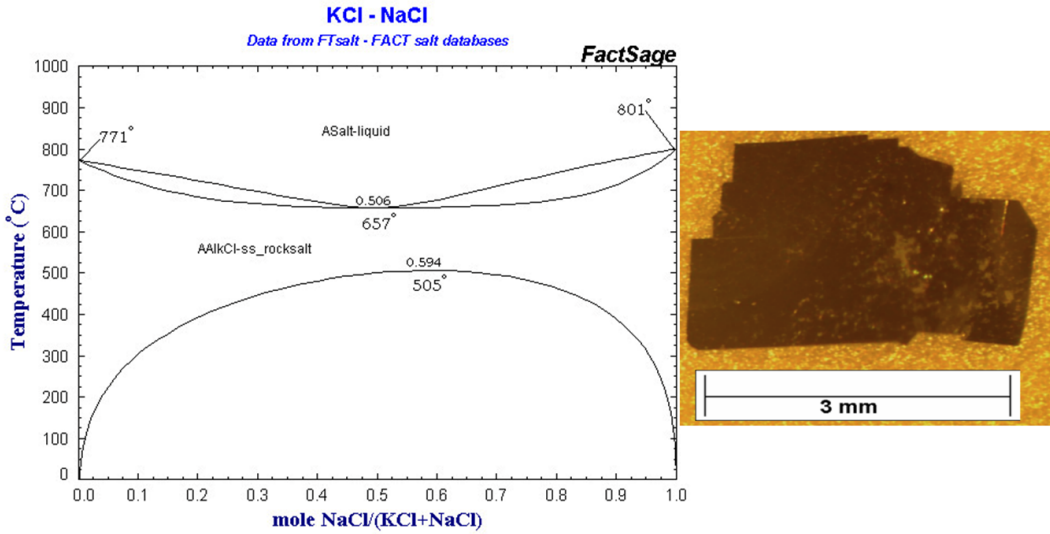
Figure 2.3: (left) Phase diagram of NaCl and KCl from online resource Fact-Sage FTSalt. (right) LaMnPO single crystal grown from NaCl-KCl flux, courtesy of J.W. Simonson.

2.1.2 $Ba_{1-x}K_xMn_2As_2$

A Sn flux was utilized for the synthesis of single crystals of $Ba_{1-x}K_xMn_2As_2$ (x=0, 0.02). Sn readily dissolves the reactants (Figure 2.4) and the optimal recipe for single crystal growth was found to be K+Ba:Mn:As:Sn = 1:2:2:35. The use of a glove box was required for air sensitive potassium and barium and the reactants were heated slowly to allow K and As to dissolve fully. The starting materials for the K doped samples were placed in a tantalum tube that was sealed in an arc furnace under argon. The middle of the tantalum tube was carefully pressed tight to allow for decanting of the Sn flux with a centrifuge. The tantalum crucible was required to prevent the reaction of K with quartz and alumina; for undoped crystals an alumina crucible was used. The tantalum tube was then placed in a quartz tube and sealed under Ar to prevent the oxidation of the Ta at high temperature. The materials were then heated to 500 °C in 3 hours, held at 500°C for 24 hours, heated to 1000°C in 6 hours, held at 1000 °C for 4 hours and subsequently cooled to 500 °C. The quartz tube was then removed from the oven and quickly inverted and dropped in a centrifuge and spun at 1000 rpm to remove the Sn flux. This synthesis typically yielded ≈ 10 mg crystals with dimensions 2 mm × 2 mm × 0.3 mm. The presence of K in the crystals was confirmed by energy dispersive x-ray spectroscopy as shown and described later in Figure

20

2.7b,c and the previously reported $ThCr_2Si_2$ structure was confirmed by single crystal x-ray diffraction [29].
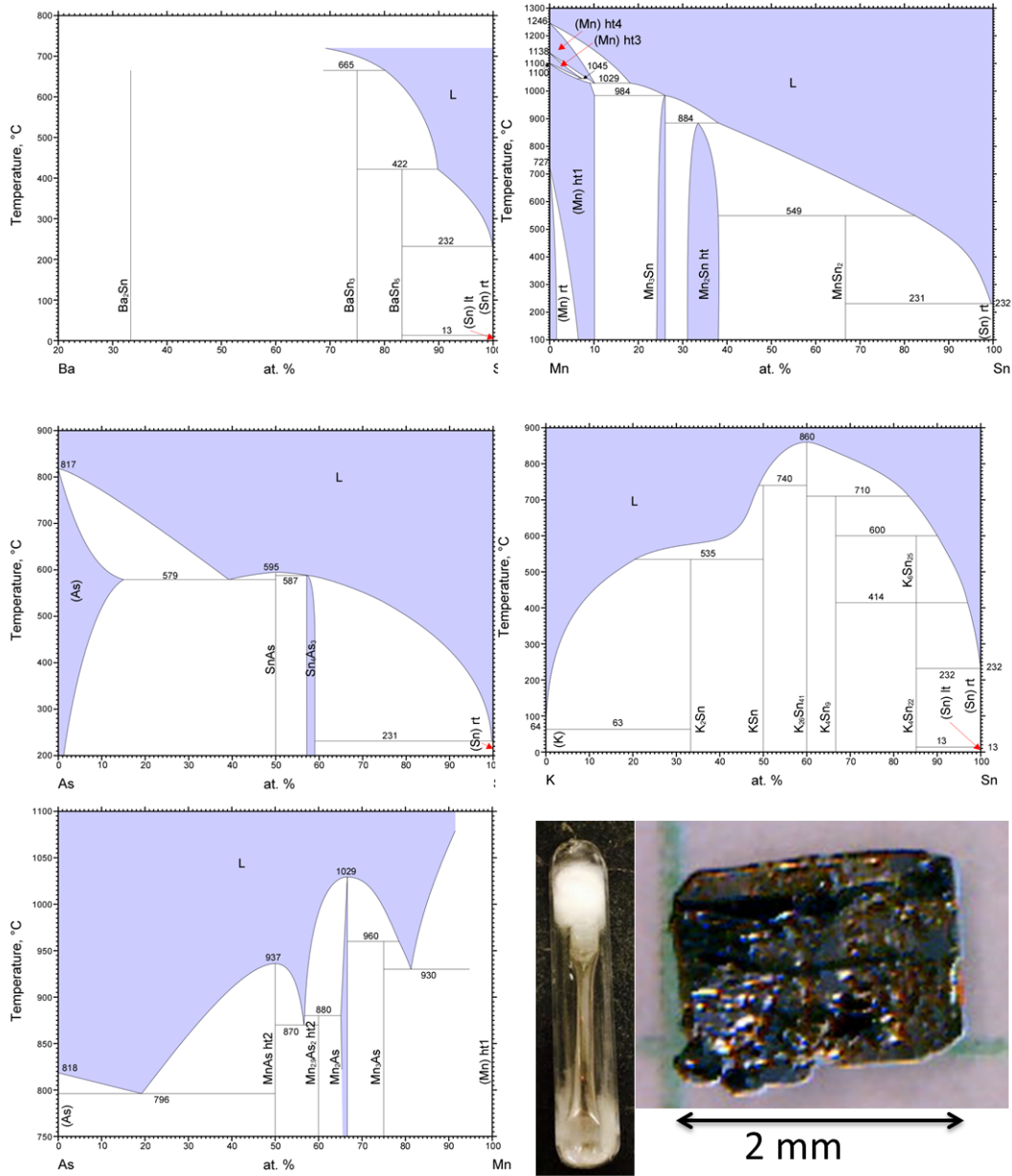
Figure 2.4: Relevant phase diagrams for the synthesis of $Ba_{1-x}K_xMn_2As_2$ from a Sn flux, reproduced from online resource Springer Materials. (bottom right) Tantalum tube containing the starting elements sealed inside a quartz tube (courtesy of S. Zellman) and a typical crystal of 2 % K doped $BaMn_2As_2$

2.1.3 $CaMn_2Sb_2$

We grew single crystals of $CaMn_2Sb_2$ as large as $5 \times 10 \times 3$ mm^3 (mass ≈ 1 g) from a Sn flux, following a procedure similar to the established method [30]. Operations with Ca were carried out in an Ar-filled glove box to minimize oxidation. An initial composition of 2:4:4:15 Ca:Mn:Sb:Sn was found to result in the largest and highest-quality crystals.

$CaMn_2Sb_2$ was initially reported as a metal [30] (Figure 2.5). However, the crystals contained inclusions of Sn which may effectively short-circuit the resistivity measurements of a bulk insulator. In our case, great care was taken to pick out clean $CaMn_2Sb_2$ single crystals. The crystals were then etched in a 1% nital solution (1% nitric acid, 99% ethanol) and Meissner measurements showed our crystals had between 0 - 3% Sn inclusions by volume. Electrical resistivity measurements in Figure 2.5b shows the resistance of our single crystals of $CaMn_2Sb_2$ increases as temperature decreases, consistent with insulating behavior. Figure 2.5c presents our optical transmission measurements. The transmission presents a sharp drop around 1 eV, thus confirming $CaMn_2Sb_2$ is a bulk insulator with a charge gap ≈ 1 eV. These results emphasize the importance of crystal quality when measuring the physical properties of intermetallic compounds.
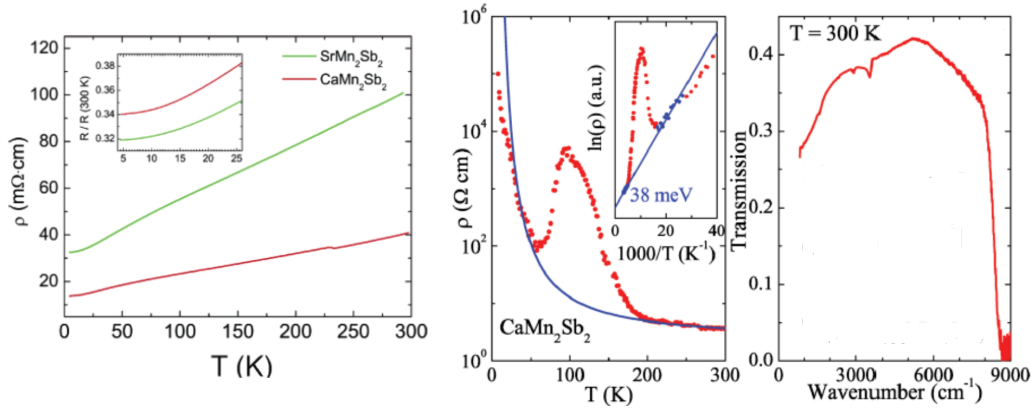
Figure 2.5: (left) Electrical resistivity as a function of temperature on single crystals that contained significant Sn inclusions [30] (right) Resistivity and optical transmission on high quality single crystals of $CaMn_2Sb_2$, showing it is in fact an insulator [31]

2.1.4 LaMn$_{0.7}$Sb$_2$

We grew large ($\approx$ 1 g) single crystals of LaMn$_x$Sb$_2$ from a Mn-Sb flux. An initial composition of 10:33.5:56.5 was found to result in the largest and highest-quality crystals. The previously reported ZrCuSiAs structure [32] was confirmed by single-crystal x-ray diffraction and the occupancy 'x' of the Mn site was found to be $\approx$ 0.71 from energy dispersive x-ray spectroscopy and neutron diffraction measurements, presented in Chapter 6. Despite several efforts, these crystals consistently were contaminated by MnSb inclusions. Mn$_x$Sb (x = 0.96 - 1.1) is a ferromagnet with a saturation magnetization per Mn atom of 3.6 μ_B - 2.4 μ_B and a Curie temperature from 600 K - 420 K [33]. The magnetic susceptibility as a function of temperature T measured on the LaMn$_x$Sb$_2$ crystals shows a ferromagnetic transition around T = 600 K (Figure 2.6). The magnetization as a function of field measured at 300 K reveals a ferromagnetic signal with a magnetic moment of 0.2 μ_B per Mn atom. However, our neutron diffraction measurements, which probe the bulk of the sample, show that LaMn$_x$Sb$_2$ is not ferromagnetic but antiferromagnetic with an ordering temperature T = 130 K. These results emphasize great care must be taken even when measuring single crystals, as the presence of a small amount of ferromagnetic impurities can greatly affect the results of magnetization measurements.
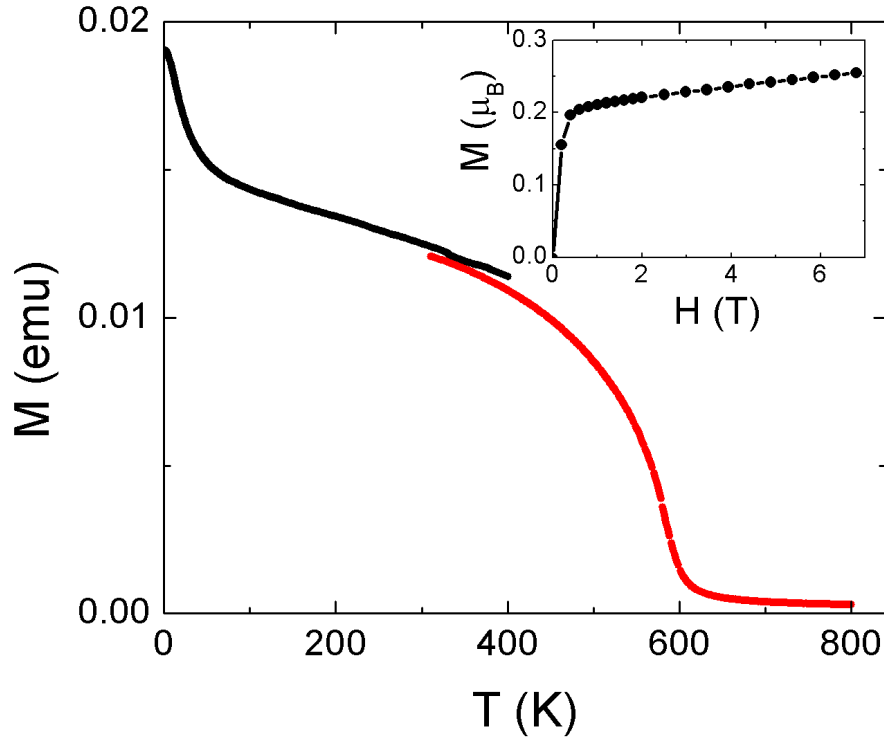
Figure 2.6: Magnetic susceptibility of a LaMn$_x$Sb$_2$ crystal with mass = 4.55 mg measured in a field of 1 T measured between 1.8 K and 400 K (black) in a Quantum Design Magnetic Property Measurement System (MPMS) and between 300 K and 800 K (red) using the Vibrating Sample Magnetometer (VSM) option of a Quantum Design Physical Property Measurement System (PPMS). Inset shows the magnetization as a function of field for the same crystal. These measurements reveal non-linear field dependence at low fields and a saturation at higher fields due to the presence of ferromagnetic MnSb impurities. Neutron diffraction measurements presented in Chapter 6 show that LaMn$_x$Sb$_2$ is in fact antiferromagnetic with an ordering temperature of 130 K.

2.2 Structure, Magnetization, Transport and Heat Capacity Measurements

Structural characterization at room temperature was performed using x-ray diffraction on powders using the Bruker D8 Advance and on single crystals using the Bruker APEX II system. Elemental composition was confirmed using energy dispersive x-ray spectroscopy on a JEOL 7600F. The magnetization, electrical resistivity and specific heat measurements presented in this thesis were all performed in Quantum Design Magnetic Property Measurement System (MPMS) and Physical Property Measurement System (PPMS), using the Vibrating Sample Magnetometer (VSM) option. These instruments provide temperature control from 1.8 K - 400 K (MPMS) and 50 mK - 1000 K (PPMS) and allow for the application of magnetic fields up to 7 T (MPMS) and 14 T (PPMS). We provide below a brief description of these measurement techniques.

The Bruker D8 Advance powder diffractometer, using Cu Kα radiation ($\lambda_{K\alpha 1} = 1.5406$ $\overset{\circ}{A}$, $\lambda_{K\alpha 2} = 1.54439$ $\overset{\circ}{A}$), was used primarily for rapid phase identification immediately following sample synthesis. A fine powder is ground using a mortar and pestle. A thin layer of this powder is mounted on a glass slide, often using Apezion N grease as an adhesive so the powder remains fixed while it spins in the diffractometer. Phases can usually be adequately identified with scans less than 1 hour. An example of a 30 minute scan on a powder of crushed single crystals of $CaMn_2Bi_2$ is presented in Figure 2.7a. The major Bragg peaks may be clearly identified thus confirming the previously reported $CaAl_2Si_2$-type structure [34]. In the mainly tetragonal systems that generally form the platelike crystals studied here, it was also often useful to look for (00l) reflections with the crystals lying flat on the glass slide to quickly confirm the phase before proceeding with further measurements. These type of scans only take 1 minute.

If crystals are present after a synthesis procedure, the APEX II diffractometer, using Mo Kα radiation ($\lambda_{K\alpha 1} = 0.709$ $\overset{\circ}{A}$), was used to quickly determine the unit cell. A small ($\approx$ 100-200 micron on side) crystal is mounted with super glue and oriented in the crosshairs of the camera. If relatively heavy atoms are present, the collection of about 30 frames is usually sufficient to give good estimate of the unit cell. This scan takes about 5 minutes. One can then quickly search the Pearsons or ICSD crystallographic databases using the determined unit cell parameters to see if this is a known phase. If one then wishes to determine the structure more completely, a strategy can be developed with the Bruker software to determine the structure down to a certain resolution in d-spacing, say 0.7 $\overset{\circ}{A}$. Our strategy assumed a triclinic
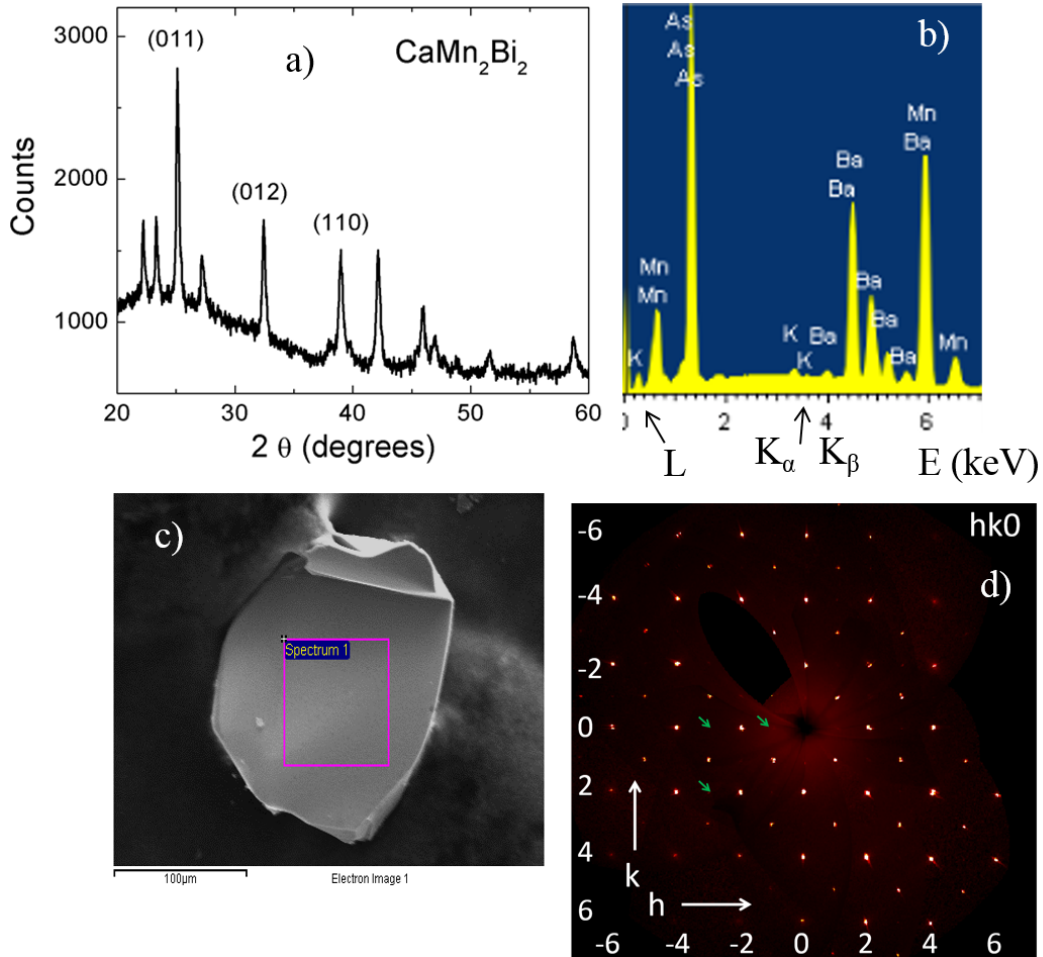
Figure 2.7: (a) Powder XRD scan performed on crushed single crystals of $CaMn_2Bi_2$ using a Bruker D8 advance with wavelength 1.54 $\mathring{A}$. (b) EDX scan performed on a single crystal of K-doped $BaMn_2As_2$ using 10 keV xrays with JEOL 7600 F. (c) SEM image of the crystal measured in (b). (d) Integrated image of the Bragg reflections in the hk0 plane of a $LaMn_xSb_2$ single crystal. Green arrows indicate the absence of intensity at wavevectors with h + k = odd, thus confirming the ZrCuSiAs structure.

crystal system, even if the initial unit cell determination was of higher symmetry. This strategy usually involves the collection of several thousand reflections within several hundred frames and can take $\approx$ 12 hours. Once completed, the reflections are integrated using Bruker software and .hkl and .p4p files are generated. An example of a precession image generated using the Bruker software is presented in Figure 2.7d. This image is from a single crystal of $LaMn_xSb_2$ that was previously reported to crystallize in the ZrCuSiAs structure [32]. Indeed, in this structure type the reflections h + k = odd for l = 0 should be forbidden, and we do not observe Bragg intensity at these positions, thus confirming the structure. These .hkl and .p4p files can be further analyzed within the Jana2006 software to look at the electron charge density and determine atomic positions, etc. within the unit cell.

Energy dispersive x-ray spectroscopy using the JEOL 7600F was used to determine the presence and relative amounts of elements within a crystal. Here, an incident beam of high energy electrons is used to knock core-shell electrons out of the atoms, with the subsequent emission of radiation that can be analyzed to uniquely identify heavy elements. This provides complementary information to single crystal x-ray diffraction. Crystals are mounted on carbon tape and either 10 keV or 20 keV incident energy is used, depending on the size of the atoms. An example of an EDX analysis of a K-doped $BaMn_2As_2$ is presented in Figure 2.7b that was performed on the region of the crystal shown in the SEM image of Figure 2.7c. The presence of potassium is readily deduced from the enhanced x-ray intensity corresponding to the K and L edges of potassium.

DC magnetization as a function of temperature was measured in a MPMS or in a PPMS using the vibrating sample magnetometer (VSM) option usually on single crystals. Care must be taken in the selection of clean single crystals as the presence of a small amount of an impurity phase can drastically modify the results as shown in Figure 2.6. The mass of the crystal should be recorded. Single crystals should be aligned in a sample holder that does not have a significant magnetic signal (e.g. a plastic straw). The direction of the magnetic field with respect to a crystalline axis can be used to determine whether magnetic anisotropy is present, as is commonly found in the strongly correlated materials of interest. For VSM measurements, the sample is rigidly mounted on a heater using high temperature alumina or silica-based cement. If one is uncertain of the remnant field in the superconducting magnet a magnetization curve is measured on palladium standard to find the zero field. A Hall sensor can also be used to zero the field in a PPMS. The sample is then inserted into the bath at 30 K. A small field ($<$ 100 Oe) is applied to center the sample in the coil. The field is then turned off and the sample cooled to 1.8 K. The

magnetization as a function of temperature may then be recorded in a chosen field from 1.8 K to 1000 K and this is a zero-field cooled measurement. These measurements can often reveal whether a material is paramagnetic, superconducting, antiferromagnetic or ferromagnetic and whether local moments are present [12]. An example of a magnetization measurement as a function of temperature on a single crystal of YMn_2Ge_2 in both the MPMS and VSM is presented in Figure 2.8a. A sharp feature is observed at $T_N = 425$ K, indicating the presence of long range antiferromagnetic order below this temperature. Figure 2.8b presents the inverse of the high temperature magnetic susceptibility revealing Curie-Weiss like behavior with a fluctuating moment of $\mu_{eff} = 3.27$ μ_B/Mn.

Resistivity as a function of temperature was measured in a PPMS, usually on single crystals to avoid intergranular effects potentially present in polycrystalline samples. The standard four-probe technique was used, with silver epoxy used to contact thin platinum wires to the crystal which are mounted on the sample pucks provided by Quantum Design. The dimensions of the contacts on the crystals should be noted to calculate the sample independent resistivity $\rho = RA/l$, where R is resistance, l is the distance between contacts, and A is the cross sectional area of the crystal. A schematic of the four-probe setup is presented in the inset to Figure 2.8c Care must be taken in the selection of clean single crystals as the presence of a small impurity can drastically modify the results as shown in Figure 2.5. The puck is then carefully inserted into the PPMS and resistivity or AC transport option chosen. For insulating samples, the DC resistivity measurement option was used so that a smaller current may be applied to avoid heating while measuring large resistances. For metallic samples, the AC resistivity option was used as it can provide greater measurement sensitivity by using signal filtering. First, a small current should be chosen, the current may then be slowly increased until a steady Ohmic resistance is recorded. On the most basic level, measurement of the magnitude of the resistivity will quickly tell us whether a material is metallic or insulating [1]. Figure 2.8c presents an example of an AC resistivity measurement of a single crystal of YMn_2Ge_2 as a function of temperature. The resistivity is rather small and increases as the temperature T increases, indicating YMn_2Ge_2 is metallic. Figure 2.8 presents the resistivity as a function of T^2. The linear trend indicates electron-electron scattering may be dominant over a very large range of temperatures.

Specific heat as a function of temperature was measured in a PPMS, usually on single crystals. The sample puck used for these measurements is presented in Figure 2.9a,b. The sample stage is thermally isolated and supported by eight fine wires, which are also used to provide heater power and measure
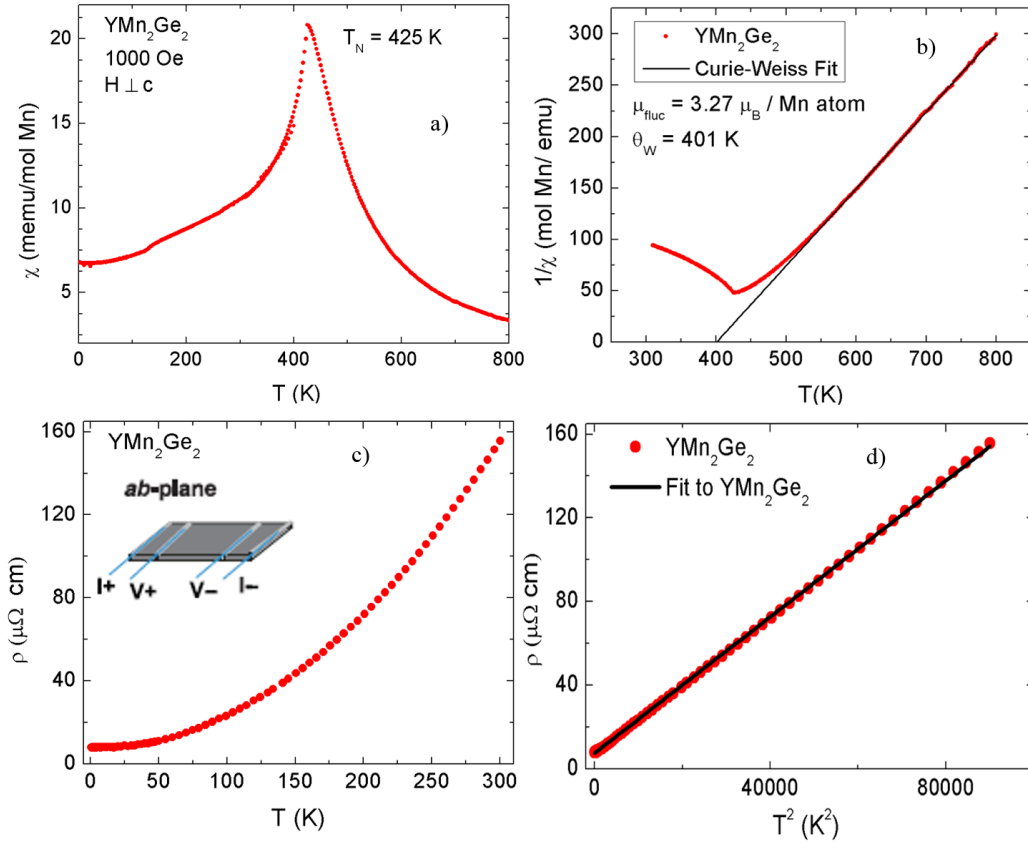
Figure 2.8: (a) Magnetic susceptibility as a function of temperature T performed on a single crystal of YMn_2Ge_2 with the magnetic field applied in the ab plane (b) High-T inverse magnetic susceptibility as a function of temperature with Curie-Weiss fit (c) Electrical resistivity ρ as a function of temperature performed in the ab plane of a single crystal of YMn_2Ge_2. (d) ρ as a function of T^2 performed on a single crystal of YMn_2Ge_2.

the sample temperature. First, the sample stage is allowed to equilibrate with the surroundings. Then a heat pulse is applied to induce a sample temperature increase of 2%. The heater power is then turned off and the sample allowed to return to equilibrium. This is termed the 'thermal relaxation method'. A typical plot of heater power, thermometer resistance and sample temperature versus time is shown in Figure 2.9c,d. With knowledge of the thermal conductance of the wires, these data may be fit with heat transport equations to determine the heat capacity of the sample (further details may be found in [35]). For these measurements it is very important for there to be good thermal contact between the sample and the platform. Thus an 'addenda' should be measured on a small amount of N grease deposited on the sample platform of the puck provided by Quantum Design. The sample is then carefully deposited on the grease. This allows for measurement from 1.8 K to 300 K. For compounds of molecular weight 400 g/mol a crystal mass of 4 mg is often ideal for specific heat measurements. Specific heat measurements as a function of temperature performed on single crystals of YMn_2Ge_2 and YRu_2Ge_2 are presented in Figure 2.9e. From Figure 2.8 we know that YMn_2Ge_2 is magnetic and that electron-electron interactions may be important. Indeed the specific heat of YMn_2Ge_2 is greather than that of its non-magnetic isostructural analog due the contribution of the mass-enhanced electrons at the Fermi surface, as well as spin wave excitations. Figure 2.9f presents the low temperature specific heat C/T as a function of T^2. The y-axis intercept is the Sommerfeld coefficient γ and provides a measure of the strength of the electronic correlations. We find that γ is significantly larger in the Mn compound that its non-magnetic isostructural Ru analog.
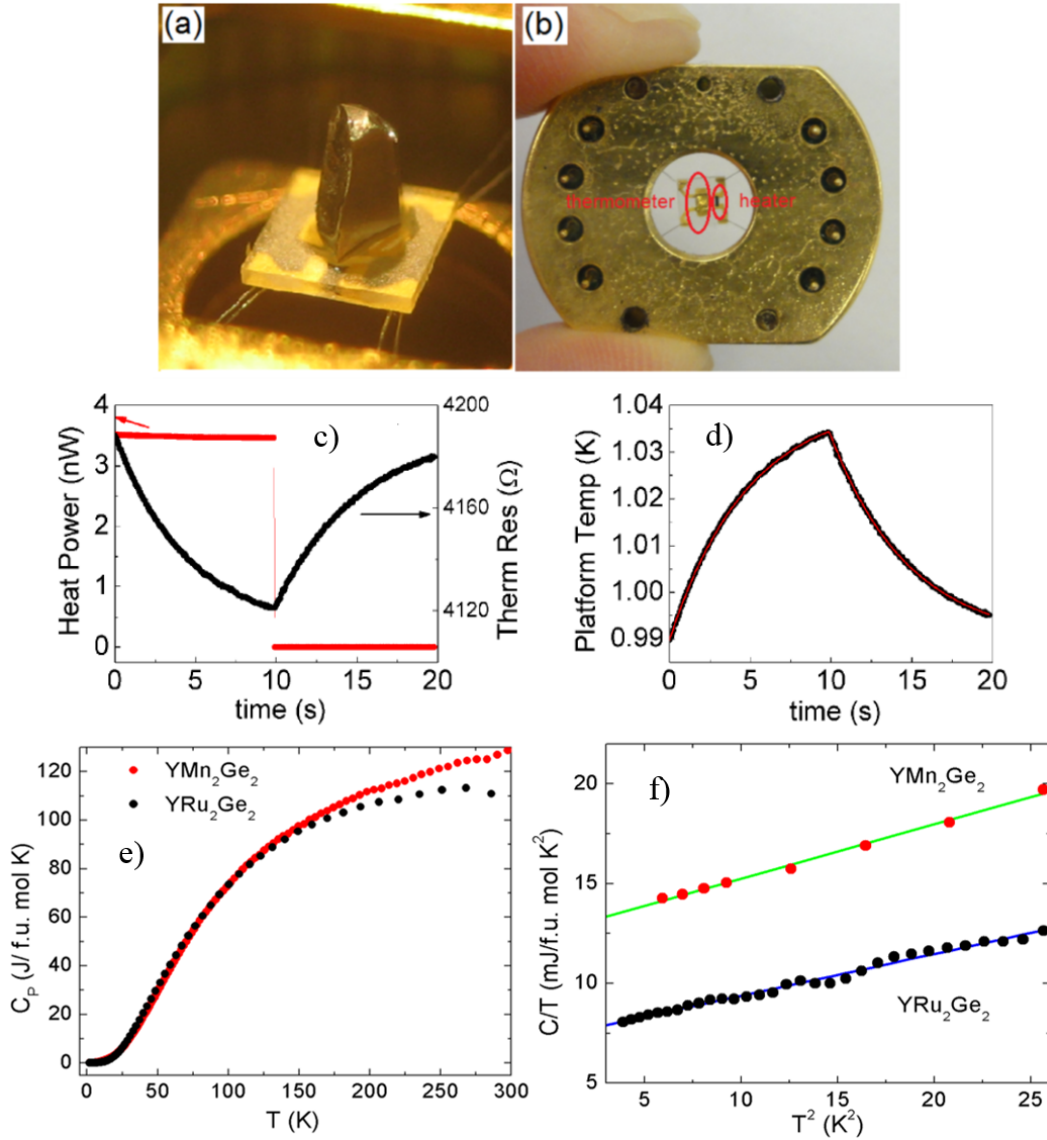
Figure 2.9: (a) Single crystal of YFe_2Al_{10} mounted on N grease on the sample platform of a specific heat puck. (b) View of the underside of the puck with the heater and thermometer indicated. (c-d) Heater power, thermometer resistance, and sample temperature as a function of time. Figures (a-d) were reproduced with permission from [36]. (e) Specific heat C measured as a function of temperature T on a single crystal of YMn_2Ge_2 and a polycrystalline pellet of YRu_2Ge_2. (f) C/T as a function of T^2 with linear fit

31

2.3   Neutron Scattering

Neutron scattering is a powerful probe of the static and dynamic magnetic properties of crystalline solids. The neutron is an uncharged particle with a magnetic dipole moment. It interacts with the nuclei in a solid via the strong nuclear force and with the magnetic spins of the nuclei or electrons via the electromagnetic force. These interactions are comparable and relatively weak so that the neutron interaction with matter may often be considered as non-perturbative, with a very well understood cross-section [37]. A traditional challenge presented by this relatively weak interaction is the need to grow rather large single crystals to provide a measurable cross-section. However, with the advent of higher intensity spallation sources and low background instruments, the utility of neutron scattering measurements is extending to ever smaller samples. In this thesis, inelastic neutron scattering (INS) is used to measure the spin wave excitations in the antiferromagnetic insulators LaMnPO and $CaMn_2Sb_2$. We performed measurements at high temperature to determine where spin correlations vanish and compared the measured spin wave dispersion at low temperature to the dispersion expected for a Heisenberg model of spins on a lattice to determine the magnetic exchange interactions in these compounds. In addition, neutron diffraction of the metal $LaMn_xSb_2$ was performed to determine its magnetic structure.

2.3.1   Magnetic Scattering Cross-section

Consider a flux Φ of incident neutrons, with certain incident energy E and momentum k, that scatters from a sample into a solid angle dΩ with energy E+dE (see Figure 2.10), with resolution determined by experimental setup. The quantity measured by the detector in a neutron scattering experiment is then the partial differential scattering cross-section:

$$\frac{d^2\sigma}{d\Omega dE} = \begin{array}{l}\text{(number of neutrons scattered per unit time into a}\\ \text{small solid angle d}\Omega \text{ in the direction } \theta, \phi \text{ with final}\\ \text{energy between E and E + dE)/ } \Phi \text{ d}\Omega \text{ dE}\end{array} \quad (2.1)$$

The measured partial differential scattering cross-section reflects transitions in the state of the combined neutron (momentum k, spin state σ) and sample system (λ) from $|k\sigma\lambda\rangle$ to $|k'\sigma'\lambda'\rangle$ with energy conservation. Applying Fermi's golden rule the cross-section for magnetic scattering can be written in the form [38]:

$$\frac{d^2\sigma}{d\Omega dE} = \frac{k'}{k}\left(\frac{m}{2\pi\hbar^2}\right)^2 |< k'\sigma'\lambda'|V_m|k\sigma\lambda >|^2 \delta(E_\lambda - E'_\lambda + \hbar\omega) \qquad (2.2)$$

where V_m consists of a magnetic potential between the dipole moment of the neutron and the spin and orbital parts of the magnetic field of the electrons in the scattering system.

To obtain the expression relevant for the work presented in this thesis, we can average over the spin states of the neutron (unpolarized beam), assume the scattering system is crystalline with electrons localized at lattice sites (shown by x-ray diffraction), and that magnetic scattering is due to spin only (quenched orbital moments in 3d transition metal elements and application of Hund's rules to Mn d^5 configuration). The expression is most useful in the form of a two-time correlation function [38]:

$$\frac{d^2\sigma}{d\Omega dE} = \frac{(\gamma r_0)^2}{2\pi\hbar}\frac{k'}{k}N[1/2gF(\kappa)]^2 \sum_{\alpha,\beta}(\delta_{\alpha,\beta} - \kappa_\alpha\kappa_\beta)\sum_l exp(i\kappa l)$$
$$\times \int_{-\infty}^{\infty}\langle exp[-i\kappa.u_0(0)]exp[-i\kappa.u_l(t)]\rangle$$
$$\times \left\langle S_0^\alpha(0)S_l^\beta(t)\right\rangle exp(-i\omega t)dt \qquad (2.3)$$

where $F(\kappa)$ is the magnetic form factor, $u_l(t)$ is the displacement of nucleus l from its atomic position and α, β label spin orientation. From this expression, one can see that when there are infinite time correlations between spins (t $\to \infty$) we observe magnetic Bragg scattering and that when spins precess in time we observe inelastic scattering. See [38] for a more detailed discussion. From an application of the Heisenberg model to the spin waves observed in the inelastic channel we may determine the strength of the magnetic exchange interactions. This will be discussed further for the case of an antiferromagnetic square lattice (Chapter 3) and antiferromagnetic corrugated honeycomb lattice (Chapter 5).

2.3.2 Instrumentation

Neutrons are especially abundant in nuclei of high atomic number, where they can significantly exceed the number of protons. To create a neutron beam, the first challenge is to extract neutrons from the nuclei. The first practical source was the nuclear reactor, in which neutron bombardment of ^{235}U nuclei induces fission, a process that releases several neutrons per incident neutron, thus allowing for a self-sustaining chain reaction. H_2O can be used to moderate
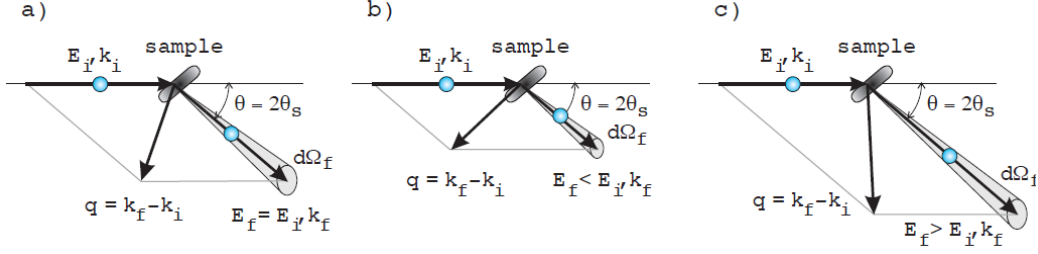
Figure 2.10: Schematics of the scattering process in a neutron scattering experiment, (a) elastic, (b), inelastic, neutron energy loss, (c), inelastic, neutron energy gain. Image reproduced from [37]

or cool the reactor yielding slow-moving (thermal) neutrons that have a higher fission cross section:

$$^{235}\text{U} + \text{n} \rightarrow 2.4 \text{ n} + \text{fragments} + 192.9 \text{ meV} \tag{2.4}$$
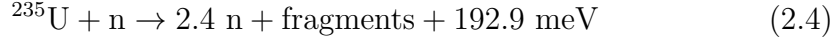
In research reactors such as NCNR at NIST, MD and HFIR at ONRL, TN we would like to extract some of the neutrons from the reactor core and the moderator to scatter from our samples. To achieve this we can use D_2O to make the moderator more transparent to neutrons and insert cylindrical thimbles poking into this heavy water to provide an escape path for the neutrons.

Another increasingly popular approach to the production of neutrons is the use of spallation sources. Here, neutrons are knocked out of heavy nuclei with high-energy protons from an accelerator. The Spallation Neutron Source (SNS) at ORNL uses a liquid mercury target that allows for adequate heat removal. The very high energy neutrons produced require a moderator to provide a neutron beam with the desired wavelength for the properties you wish to study. For condensed matter systems we usually want to use neutrons to study phenomena at the atomic scale. Therefore a moderator at room temperature is appropriate considering the Maxwell-Boltzmann distribution of velocities for a neutron at a temperature ≈ 300 K (see Figure 2.11a) where the energy of a neutron $E_n \approx 81.81/\lambda^2 = 1/2 \text{ mv}^2$ and the Maxwell Boltzmann distribution of velocities is given by the well-known expression

$$f(v) = \sqrt{(\frac{m}{2\pi k_B T})^3} 4\pi v^2 exp(\frac{-mv^2}{2k_B T}) \tag{2.5}$$

Spallation sources can produce pulsed beams allowing for time-resolved studies on millisecond timescales, in contrast to reactor sources that produce continuous beams. The SNS currently provides the highest neutron intensity of all operating neutron sources (see Figure 2.11) and therefore is the facility

34
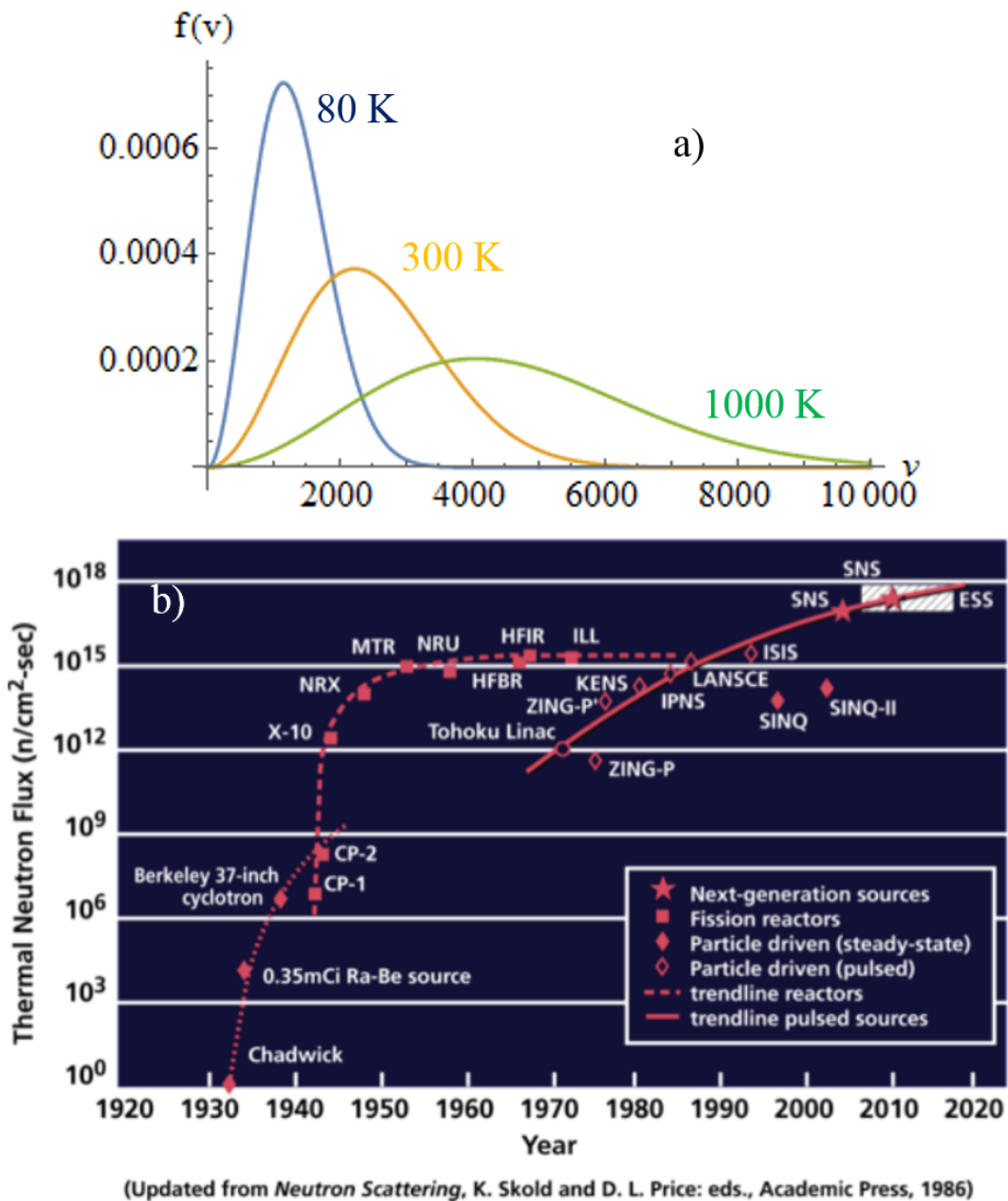
Figure 2.11: (a) Maxwell-Boltzmann distribution of velocities for moderators at different temperatures. At 300 K, the most probable velocity of a neutron is 2200 m s^{-1} corresponding to a wavelength $\lambda = 1.8$ Å and energy E = 25 meV. (b) Flux at neutron sources worldwide.

of choice for probing e.g. weakly magnetic materials or for examining smaller crystals or for techniques that require a high flux such as pair distribution function measurements.

There are two commonly used spectrometers to measure inelastic neutron scattering, the triple-axis spectometer and the time-of-flight spectometer (Figure 2.12). In a triple-axis spectrometer, the three axes correspond to monochromator, sample, and analyzer where incident/final energies are selected by Bragg diffraction from an appropriate grating. We used the triple-axis spectometer BT-7 at NIST for high temperature inelastic neutron scattering measurements presented in Chapter 3.
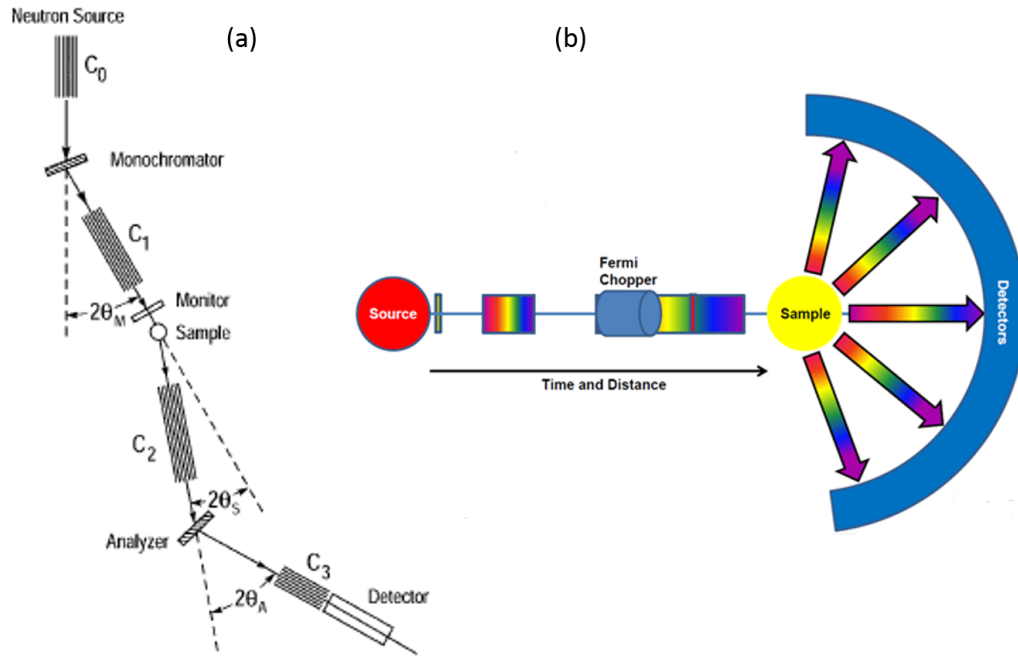
Figure 2.12: Schematic of a triple axis spectrometer (a) reproduced from [39] and time-of-flight spectrometer (b)

In a time-of-flight instrument at a spallation source, the energy transfer is determined by the time it takes a neutron to travel from the sample to the detector, while the incident energy is selected from the white beam using a rapidly rotating cylinder with a single slit, i.e. a Fermi chopper. The time-of-flight measurements presented in this thesis were performed at the SEQUIOA time-of-flight instrument at Oak Ridge [40] and the sample geometry used with single crystals of $CaMn_2Sb_2$ as described in Chapter 5.

The large detector banks of ^{3}He linear position sensitive tubes at SE-QUIOA enable the sampling of large regions of energy-wavevector space, gen-
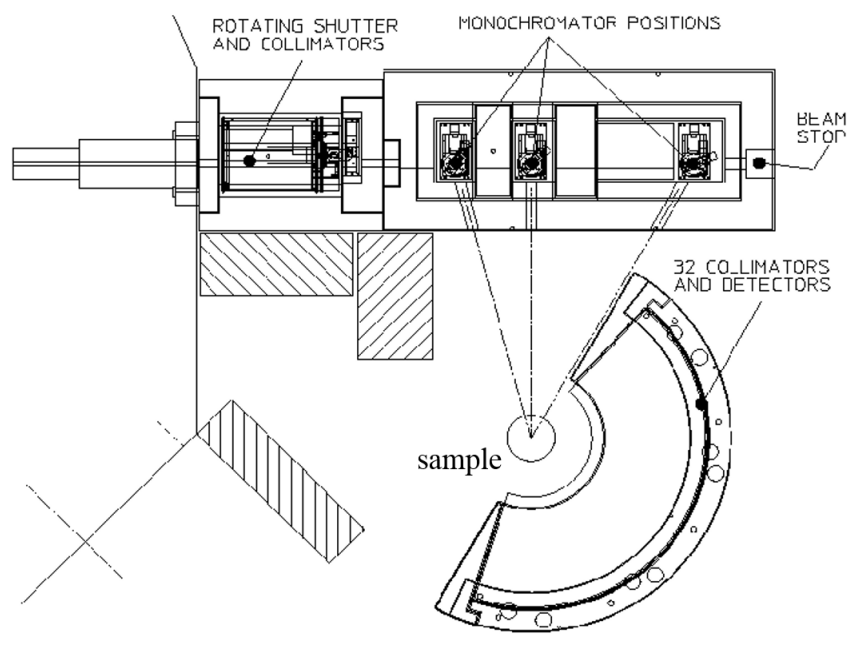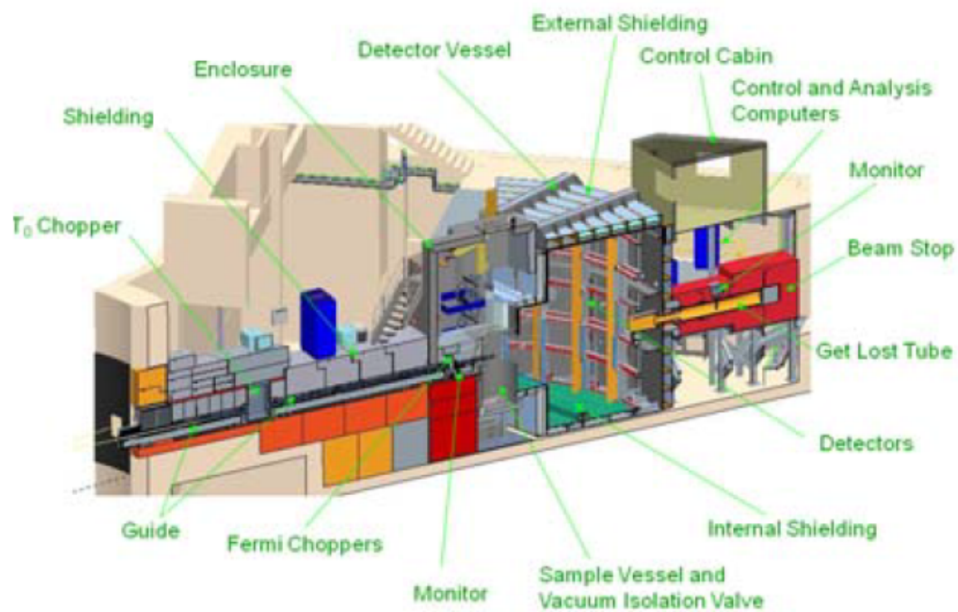
Figure 2.13: Schematics of the SEQUIOA time-of-flight instrument at SNS (top [40]) and the BT1 diffractometer at NIST (bottom)

erating a large amount of data (see Figure 2.13 for schematic of the SEQUIOA instrument). An example of the region of reciprocal space at one energy transfer sampled at SEQUIOA for one orientation of the crystal with respect to the incident beam is provided in Figure 2.14a. The final measured cross-section over a large region of reciprocal space is obtained by summing all these angles, and the result is presented in Figure 2.14b. The Horace software developed at the ISIS neutron source in the UK was used within Matlab to generate the sum of the measured cross sections at different orientations of the crystal with respect to the incident beam. The u-v matrix that defines the orientation of the crystal in the beam and the unit cell of the crystal must be provided, as well as the parameter file of the instrument. The file used for this data reduction and summing for a temperature of 5 K for $CaMn_2Sb_2$ may be found on the SNS cluster in the directory /SEQ/IPTS-8138/shared/ak7/gen_sqw_50meV_5K.m. Similar files for different temperatures may be found in this directory where IPTS-8138 corresponds to the sample identifier assigned to $CaMn_2Sb_2$ by the SNS. The measurements on a powder sample of LaMnPO were assigned the same IPTS-8138. A summary of the parameters for each experimental run may be found in /SEQ/IPTS-8138/shared/autoreduce/experiment_summary.csv.
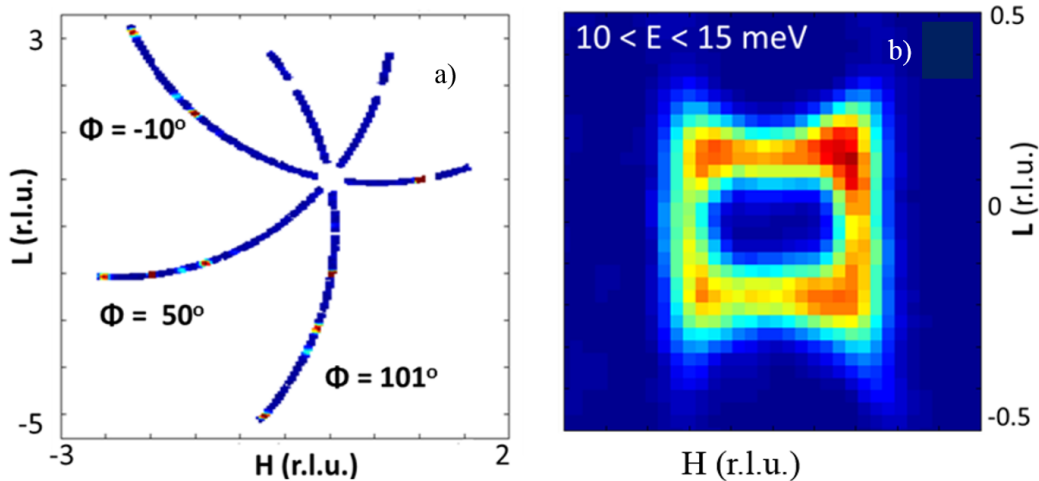
Figure 2.14: (a) H-L space sampled at fixed energy transfer for different orientations of the sample with respect to the incident beam. (b) Final H-L coverage after integrating over all angles.

High resolution neutron diffraction measurements on $LaMn_xSb_2$ were performed at the BT1 high resolution powder diffractometer at NCNR, NIST utilizing the mail-in service. A schematic of the diffractometer is presented in Figure 2.13 showing the choice of three different monochromators depending

on whether higher flux or better resolution is desired. For our experiments we used the Ge(311) ($\lambda = 2.078$ Å) monochromator which provides the highest flux and is ideal for looking at magnetic samples, where most intense Bragg reflections occur at low angles. For a complete description of the BT1 instrument see www.ncnr.nist.gov/instruments/bt1 which provides detailed information.

Chapter 3

LaMnPO

We present here experimental and theoretical evidence that together clarifies the relative importance of the Hubbard U, Hund's J_H and Heisenberg J for stabilizing the charge gap Δ in LaMnPO. Our inelastic neutron scattering measurements determine the nearest and next-nearest exchange interactions $J_{1,2}$, which are much smaller than Δ. LaMnPO is found to be a quasi-two dimensional antiferromagnet with magnetic correlations persisting to $\approx$ 700 K, far above the Néel temperature T_N = 375 K. Optical measurements indicate that Δ has decreased by only 10% at $\approx$ 700 K, where magnetic correlations have vanished, compared to its value deep in the antiferromagnetic phase T $<<$ T_N. This is evidence that $J_{1,2}$ play only minimal roles in setting the size of Δ in LaMnPO. Density functional theory plus dynamical mean field theory (DFT+DMFT) calculations show instead that a large J_H as well as U is required to reproduce the charge gap observed in both the antiferromagnetic and paramagnetic states. The Mn-pnictide LaMnPO is thus a Mott-Hund's insulator, analog to the Hund's metal from which superconductivity emerges in the Fe-pnictides. The results presented in this chapter have been published as [23]

3.1   Introduction

The metal-insulator transition in correlated electron systems, where electron states transform from itinerant to localized, has long been one of the central themes of condensed matter physics [1]. In a prototypical Mott transition [3], increasing the ratio U/t of the onsite Hubbard U to the kinetic hopping t leads to the enhancement of the effective mass of initially itinerant electrons and to spin fluctuations that can drive magnetic order. When U/t surpasses a critical value, the electrons become spatially localized and a metal-insulator

transition (MIT) occurs, driven by the formation of a charge gap. Often, the localized electrons are moment-bearing, and magnetic order accompanies the MIT. Thus, electronic localization transitions often involve two different instabilities: magnetic order, involving spontaneous symmetry breaking, and a metal-insulator transition (MIT) that connects an electronic structure with a non-zero density of states at the Fermi surface to an electronic structure with a charge gap.

Recently, Mn-pnictide compounds have received widespread attention because they are magnetic insulators [31, 41–43] like the parent compounds of the cuprate high temperature superconductors (HTSC) [44] while adopting the same crystal structures as the metallic parent compounds of the Fe-based HTSC (Figure 3.4a) [7, 45]. Suppressing the magnetic order and driving an insulating Mn-pnictide across a MIT could lead to a more correlated version of their Fe-based counterparts, where even higher temperature superconductivity may be observed [43, 46, 47]. However, it is only very recently that superconductivity has been observed in any Mn-based compound: the itinerant magnet MnP becomes superconducting below $T_c \approx 1$ K at pressure of 8 GPa [48]. As outlined in the introduction to this thesis, in multi-orbital compounds such as the Fe and Mn-pnictides the origin of the charge gap may be not only the Hubbard U, but also the Hund's interaction J_H and possibly Heisenberg exchange interaction J. In these systems, antiferromagnetic (AF) correlations can stabilize an insulating state when the spin flip energy $\propto$ J, is comparable to the charge gap Δ [49]. In addition long range AF order alone can stabilize a gap in a Slater insulator, with the gap vanishing at T_N [16]. The importance of these interactions has been established in the metallic Fe-pnictides [50], but so far their impact on the isostructural and insulating Mn compounds is not well understood.

Previous measurements show that LaMnPO can be driven through a metal-insulator transition using pressure but not doping [43]. Optical transmission and photoemission measurements show that ambient pressure LaMnPO is an insulator with $\Delta = 1.3$ eV [43, 51, 52]. The magnitude of the charge gap is much larger than the activation gap of 100 meV determined from electrical resistivity measurements, suggesting that $\rho(T)$ is dominated by excitations from in-gap states to the conduction band edge [52]. Neutron diffraction measurements reveal a checkerboard-type antiferromagnetic structure below the Néel temperature $T_N = 375$ K with a $T \rightarrow 0$ K ordered moment of 3.2 μ_B/Mn, much reduced from the high spin value of 5 μ_B/Mn predicted by Hund's rules when all the spins of the Mn d electrons are parallel [43, 53]. The low value of the ordered moment, coupled with significant valence fluctuations detected in x-ray absorption measurements and also in density functional theory plus dy-

namical mean field theory (DFT+DMFT) calculations, suggests that ambient pressure LaMnPO is near a metal-insulator transtion [43]. However, doping 28% fluorine into $LaMnPO_{1-x}F_x$ had a minimal effect on the charge gap and ordered moment and no other suitable dopant (e.g. As, Ca, Sr, vacuum treatment, H_2/Ar gas flow) has been identified that can drive an insulator-metal transition, as judged by electrical resistivity measurements [52]. In contrast, pressure drives a MIT in LaMnPO at 20 GPa, followed by AF order collapse at $\approx$ 30 GPa (Figure 3.1) [54]. This separation of charge and magnetic instabilities in pressurized LaMnPO adds new urgency to uncovering the origin of the charge gap and its relationship to magnetic order.

In this chapter, we present a combined experimental and theoretical approach to determine the origin of the charge gap in insulating antiferromagnetic ambient pressure LaMnPO. We present inelastic neutron scattering measurements over a range of temperatures T from 5 K to 600 K to determine the magnitude of the exchange interactions in LaMnPO and the temperature where the magnetic moments become de-coupled. We then compare these results to complementary high temperature optical transmission measurements. These spectroscopic methods decisively show that both short and long range mangetic ordering play only a small role in opening a charge gap. We then present DFT+DMFT calculations that are in agreement with our experimental results and further show that Hund's coupling, as well as Hubbard U, can account for the insulating ground state of LaMnPO.

3.2 Experimental Details

High temperature T > 300 K inelastic neutron scattering measurements were performed at the BT-7 triple-axis spectrometer using the reactor source at NIST Center for Neutron Research [55] on a powder sample of LaMnPO. PG(002) crystals were used as monochromators and analyzers with a fixed final energy E = 14.7 meV and the reactor collimation was open. Inelastic neutron scattering measurements at T = 5 K were performed at the SEQUIOA time of flight instrument using the Spallation Neutron Source at Oak Ridge National Laboratory [40] on a powder sample of LaMnPO. An incident energy of 250 meV was used, with the Fermi 2 chopper set to 600 Hz and the T0 chopper set to 120 Hz.
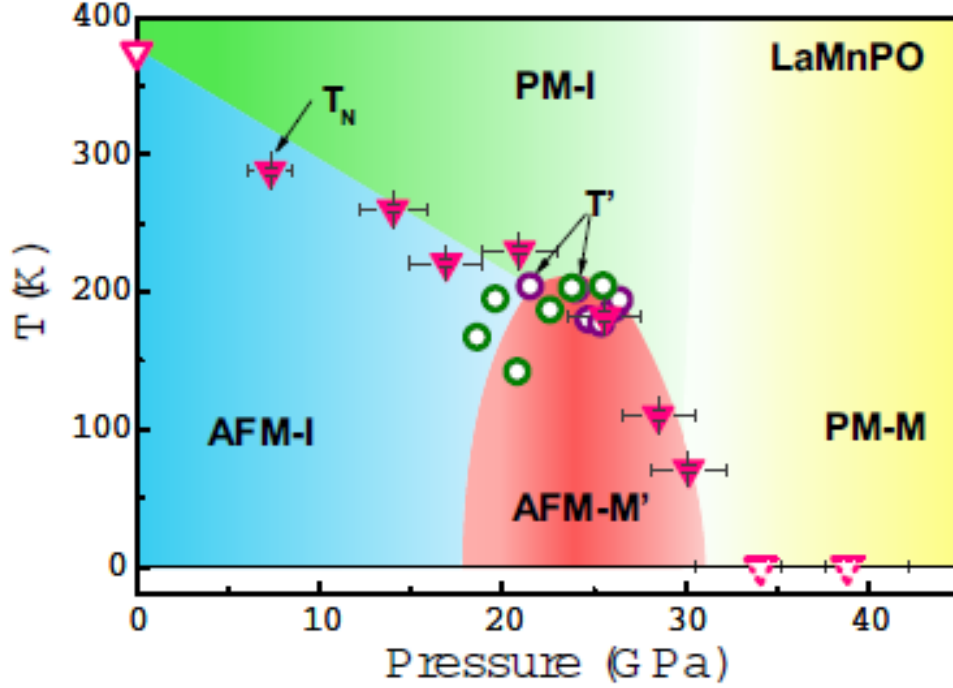
Figure 3.1: The pressure-temperature electronic phase diagram of LaMnPO taken from [54]. The open triangle represents the antiferromagnetic ordering temperature $T_N = 375$ K at ambient pressure, taken from neutron diffraction measurements [43, 53]. The filled triangles correspond to values of T_N obtained from high pressure ac susceptibility measurements. The open circles represent temperatures T, where the resistance is at a maximum, taken from different independent runs. There is no indication of antiferromagnetic order at 34 GPa, as displayed by the dashed open triangles. The acronyms AFM-I and AFM-M stand for antiferromagnetic insulating and antiferromagnetic mixed state regimes, respectively. PM-I and PM-M represent paramagnetic insulating and paramagnetic metallic states, respectively.
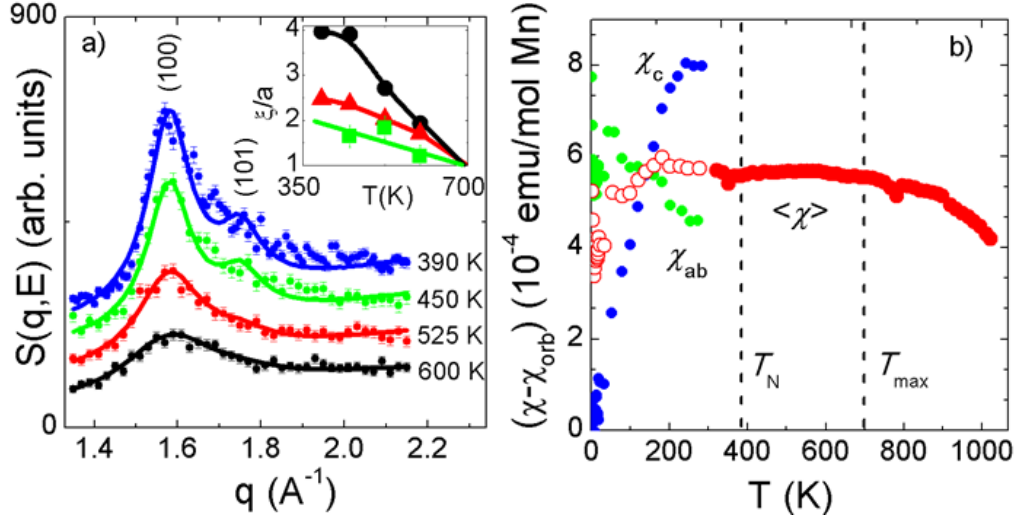
Figure 3.2: (Color online)(a) Wavevector q dependence of the scattered neutron intensity $S(\mathbf{q},E)$ for constant energy transfer $E = 5$ meV at temperatures T indicated. Solid lines are fits as described in the main text. Inset: T-dependence of the spatial correlation length ξ in units of the lattice constant a, for $E = 5$ meV ($\bullet$), 10 meV ($\blacktriangle$), 15 meV ($\blacksquare$). (b) Magnetic susceptibility $\langle\chi\rangle$ of a collection of single crystals ($\circ$) $\langle\chi\rangle = 2/3$ (χ_{ab}) $+1/3$ (χ_c) where χ_{ab} ($\bullet$) and χ_c ($\bullet$) were measured with a 1 T field applied in the ab plane and c plane respectively. The magnetic susceptibility at high temperatures was measured on a powder sample ($\bullet$). Orbital susceptibility $\chi_{orb} = 1.7\mathrm{e}{-4}$ emu/mol Mn is subtracted from all data. Dashed lines indicate the Néel temperature T_N and mean-field ordering temperature T_{max}.

3.3 Experimental Results and Analysis

Inelastic neutron scattering provides a detailed picture of the development of the antiferromagnetic correlations above $\mathrm{T}_N = 375$ K. Fig 3.2a presents the wavevector q dependence of the scattered neutron intensity for temperatures $T > T_N$ and energy transfer E = 5 meV. We observe two overlapping peaks centered at the antiferromagnetic ordering wavevectors $q_{100} \approx 1.6$ $\mathring{A}^{-1}$ and $q_{101} \approx 1.75$ $\mathring{A}^{-1}$, and we ascribe this enhanced scattering to antiferromagnetic spin correlations in the paramagnetic state.

We wish to determine the maximum temperature at which the spin correlations are confined to the unit cell and the moments are freely fluctuating so as to determine the effect of antiferromagnetic correlations on the charge gap in LaMnPO. For this purpose, it is crucial to account for the instrumental resolution function of the BT-7 triple-axis spectrometer. The Matlab-based

software ResLib [56] allows one to calculate the resolution function at each point, given the spectrometer configuration and sample parameters, and can accept a theoretical structure factor S(Q) that is convoluted with the resolution function and fit to the experimental data. The resulting expression for the inelastic neutron scattering intensity:

$$\frac{d^2\sigma}{d\Omega dE} = R_0(q) \int d^4Q S(Q) \exp[-1/2(Q^i - q^i)(Q^j - q^j)M_{ij}(q)] \qquad (3.1)$$

where Q is a 4-D vector in energy momentum space and M is the Cooper-Nathans resolution matrix[57, 58].

We will assume the Lorentzian form for the wavevector dependence of the critical scattering that was originally proposed by Ornstein and Zernicke [59]. The structure factor S(q) is then the sum of two Lorentzian functions and a linear background:

$$S(q) = \sum_{i=1}^{2} \frac{A_i}{(q - q_i)^2 + \Gamma^2} + Bq \qquad (3.2)$$

Here, i indexes the $q_{100,101}$ peaks, Γ is the width of the peaks and A_i, B are constants.

We fit the resulting expression for the expected neutron cross-section to our high temperature S(q, E = 5 meV, 10 meV, 15 meV) (shown for E = 5 meV in Figure 3.2a) and find that the spin correlation length $\xi = 1/a\Gamma$, in units of the lattice parameter $a = 4.054$ Å, decreases with increasing temperature for energy transfers E = 5, 10, 15 meV (inset of Figure 3.2a). Furthermore, we can estimate the temperature where the antiferromagnetic spin correlations have vanished using the approximate value of the critical exponent for the three-dimensional Heisenberg model $\xi \approx t^{-\nu}$ where $\nu \approx 0.707$ and t = (T-T_N)/T_N. We find that $\xi \rightarrow a$ at $T_{max} \approx 700$ K (inset of Fig 3.2a), evidence that the intersite exchange interactions are no longer strong enough to keep the Mn moments coupled above this temperature due to the strong thermal fluctuations.

In Figure 3.3a we present inelastic neutron scattering measurements of LaMnPO at T = 5 K. The measured cross-section has been transformed into the imaginary part of the dynamic susceptibility χ(q,E) that is related to the scattering cross-section by the fluctuation-dissipation theorem:

$$\chi''(q, E) = \frac{d^2\sigma}{d\Omega dE}(1 - \exp(\frac{\hbar\omega}{k_B T})) \qquad (3.3)$$

The data have also been corrected for the magnetic form factor of Mn^{2+} that is obtained from the Fourier transform of the magnetization distribution
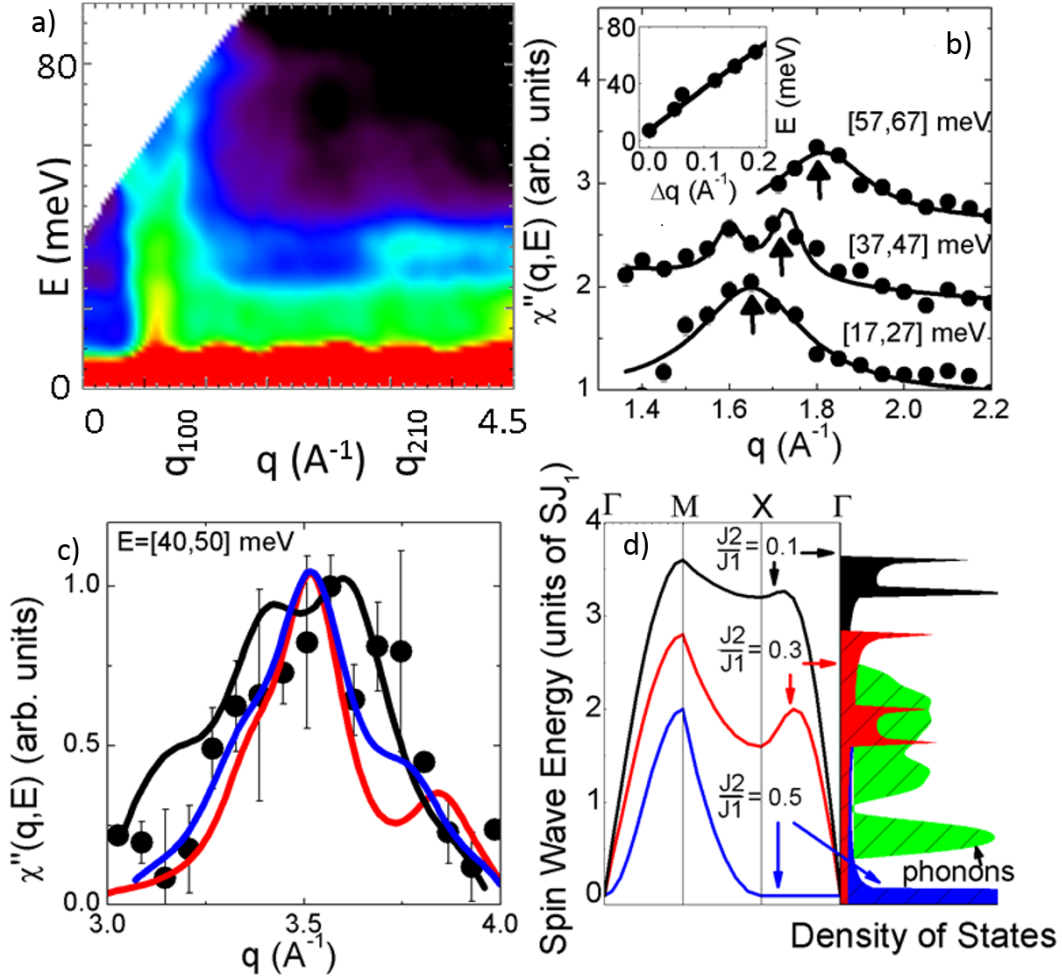
Figure 3.3: (a) The dynamic susceptibility $\chi(q,E) = S(q,E)$ $(1-\exp(-E/k_BT))$ measured at 5 K. (b) E-cuts near the (100) AF zone center summed over the indicated ranges. Solid lines are fits to the sum of two Lorentzians. Inset: Δq, measured relative to q_{100}, for different E. Solid line is theoretical expression for $\epsilon(q)$ in Γ-X direction, with $SJ_1 = 34$ meV. Error bars are smaller than points. (c) E-cut near (210) averaged on the interval 40-50 meV. Solid lines is the resolution-convoluted intensity expected from a powder-averaged Heisenberg model for $SJ_1 = 18$ meV (-), 34 meV (-), 48 meV (-). (d) Left: Calculations of $\epsilon(q)$ along different directions in reciprocal space for values of J_2/J_1 indicated. Right: Comparison of the experimental density of states DOS (green shaded area) to the powder average of $\epsilon(q)$ for values of J_2/J_1 indicated. The low energy part of the DOS is attributed to phonons.

of an isolated atom and has been tabulated in [60] for L = 0 as:

$$F(q) = (0.422\ \mathrm{e}^{-17.684q^2} + 0.5948\ \mathrm{e}^{-6.005q^2} + 0.0043\ \mathrm{e}^{0.609q^2} - 0.00219)^2 \quad (3.4)$$

F(q) falls off at higher q as shown in Figure 3.4d.

The most prominent features of the magnetic scattering are the intense dispersive arches of excitations centered near $q_{100} = 1.6\ \AA^{-1}$ and $q_{210} = 3.5$ $\AA^{-1}$. We attribute this scattering to spin waves from the ordered Mn moments and note that the spin waves merge near (q,E) = $(3\ \AA^{-1}, 80\ \mathrm{meV})$. In Figure 3.3b we present Q-cuts through Figure 3.3a at different energies χ(q,E) to quantify the dispersion of the spin waves at the q_{100} position. Here we observe that q_{100} is flanked by two peaks at $q_{100} \pm \Delta q$, which we fit with Lorentzian functions to determine the spin wave dispersion E(Δq), plotted in the inset. The intense scattering at all q below ≈ 20 meV is attributed to phonon excitations.

The Heisenberg model for localized spins should be applicable to LaMnPO as it is an insulator:

$$H = 2J \sum_{m,m+r} S_m S_{m+r} \quad (3.5)$$

when only the exchange interaction between nearest neighbors separated by the vector r are included.

The expected spin wave dispersion for an antiferromagnet considering only nearest-neighbor interactions between the two sublattices is [61]:

$$\omega(Q) = 2S\sqrt{J(0)^2 - J(Q)^2} \quad (3.6)$$

where S is the total spin on the atom and the exchange interaction term:

$$J(Q) = \sum_{r_{NN}} J_1 \mathrm{e}^{iQr_{NN}} \quad (3.7)$$

The reciprocal lattice vector Q = (q_x, q_y) and there are four nearest neighbors for the square lattice r_{NN} = [(a/2,a/2), (-a/2,a/2), (a/2,-a/2), (-a/2,-a/2)] where a is the lattice parameter yielding the expression:

$$E(Q) = 4SJ_1\sqrt{\left(1 - \cos^2(q_x\frac{a}{2})\cos^2(q_y\frac{a}{2})\right)} \quad (3.8)$$

This expression was fit to the experimental spin wave dispersion as shown in Figure 3.3b to determine the nearest neighbor exchange interaction $SJ_1 = 34 \pm 4$ meV. The fits were performed above the spin gap of 7 meV that was
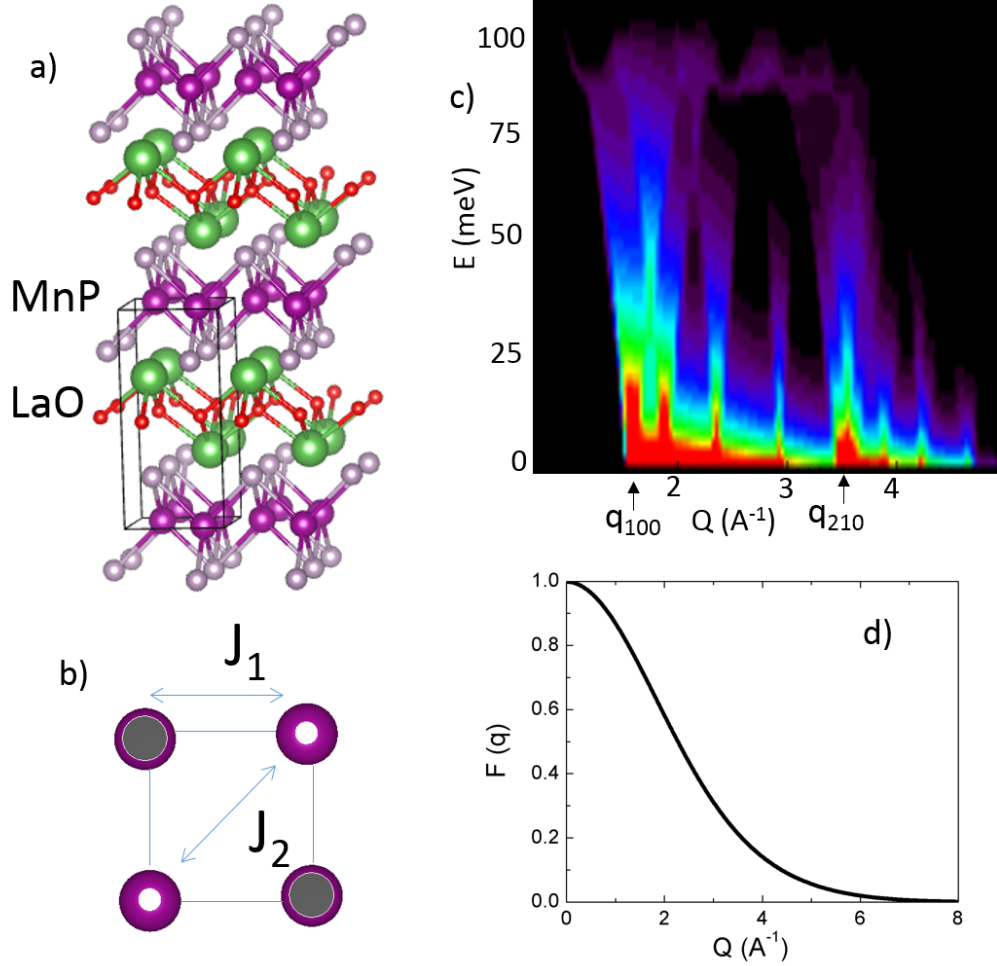
Figure 3.4: (a) The crystal structure of LaMnPO which consists of square nets of Mn atoms (Mn-Mn = a/$\sqrt{2}$ = 2.87 $\mathring{A}$) that are tetrahedrally co-ordinated by P atoms. This forms a layers of edge sharing Mn-P tetrahedra that are well separated by a LaO charge transfer reservoir layer with c = 8.83 $\mathring{A}$. (b) First and second neighbor exchange interactions on the square lattice. (c) Calculated neutron scattering cross-section for LaMnPO. The columns of scattering centered at q_{100} = 1.6 $\mathring{A}^{-1}$ and q_{210} = 3.5 $\mathring{A}^{-1}$ and the overlap of scattering near 90 meV are well reproduced. (d) The magnetic form factor for neutrons scattering from Mn^{2+} ions.
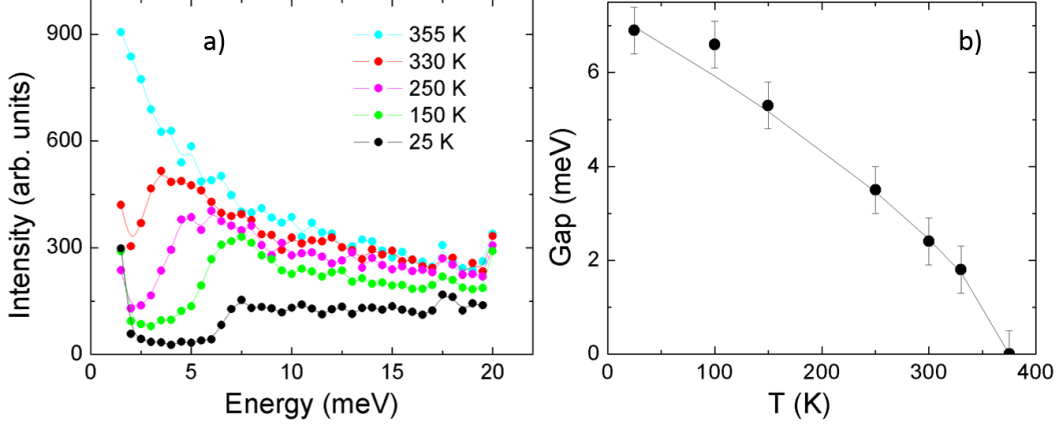
Figure 3.5: (a) Scattered neutron intensity as a function of energy at the temperatures indicated. (b) Spin gap as a function of temperature.

determined from our high resolution measurements at BT 7 (Figure 3.5). The spin gap is found to vanish at the antiferromagnetic ordering temperature T_N = 375 K.

Since our sample is polycrystalline, $\chi(q,E)$ may include significant contributions from spin waves that originate in different magnetic zones. Figure 3.3c compares $\chi(q,E)$ near the q_{210} = 3.5 $\mathring{A}^{-1}$ AF zone center to the powder averages of the theoretical dispersions for different values of SJ_1. The experimental data are also consistent with the Heisenberg model for the same value of SJ_1 = 34 meV.

Analysis of the total spin wave density of states (SWDOS), obtained by integrating over all wavevectors shown in Figure 3.3a , shows that a full description by the Heisenberg model requires the inclusion of a second neighbor interaction J_2. Theoretical spin wave dispersions along high symmetry directions in reciprocal space are presented in Fig. 3.3d for values of J_2/J_1 ranging from 0.1-0.5. When J_2 is included (see Figure 3.4b), the spin wave dispersion derived above for J_1 must be modified as outlined Chapter 5 and the resulting expression for the spin wave dispersion is:

$$\hbar\omega = 2\sqrt{(2 - \frac{J_2}{J_1}(2 - cos(2\pi q_x) - cos(2\pi q_y)))^2 - (2cos(\pi q_x + \pi q_y))^2} \quad (3.9)$$

The corresponding powder averaged SWDOS is compared to the observed DOS (Fig. 3.3d) and most resembles the experimental results when $0.2 < J_2/J_1 < 0.4$, yielding SJ_2 in the range 7-14 meV. With these values of exchange interactions, a mean-field ordering temperature $T_{MFT} = 4(J_1\text{-}J_2)S(S+1)/(3k_B)$

49

$\geq$ 760 K is expected [13], similar to the value of T_{max} determined from the analysis of the high temperature inelastic neutron scattering measurements presented above.

The temperature dependence of the magnetic susceptibility $\chi(T)$ in LaMnPO is much as expected [62, 63] for a quasi-2D Heisenberg AF. $\chi(T)$ of powdered LaMnPO crystals in a 1 T field is shown in Fig. 3.2b. While no feature is seen at $T_N = 375$ K, there is a broad maximum in $\chi(T)$ centered at ≈ 700 K above which the onset of a Curie-Weiss susceptibility $\chi \propto 1/T$ is observed [64] and above which LaMnPO may be considered a simple paramagnet with independent freely fluctuating magnetic moments. This is the same temperature where the AF correlations determined from inelastic neutron scattering measurements are projected to vanish. We also measured $\chi(T)$ between 1.8 K and 400 K on a collection of single crystals with the field oriented along the c-axis (χ_c) and with the field in the ab plane (χ_{ab}). The polycrystalline average $\chi = 2/3\chi_{ab} + 1/3\chi_c$. The normalized $T=0$ susceptibility $\chi_0 = \chi(T=0)J_1/Ng^2\mu_B^2$ [64] $= 0.063 \pm 0.01$ is in good agreement with a modified spin-wave theory [65] with $S = 3/2$ and $J_1 = 22$ meV which yields $\chi_0 = 0.058$. The experimental value of the peak susceptibility $\chi_{max} = \chi(T = T_{max})J_1/Ng^2\mu_B^2 = 0.085 \pm 0.05$ is also in good agreement with the calculated value of 0.091 ± 0.003. We conclude that this modified spin-wave theory provides a very good description of our magnetic susceptibility measurements.

Our analyses of the inelastic neutron scattering and magnetic susceptibility data reveal that the exchange interactions $J_{1,2}$ are significantly smaller than the charge gap. The ratio of the spin flip energy cost to the gap, $2S^2J/\Delta \approx 0.1$, naively implies only a ≈ 10 % reduction of Δ would occur by T = 700 K. On the other hand, if $\Delta \to 0$ at T_N, it would identify LaMnPO as a Slater insulator, where the gap is entirely due to the long range magnetic order. What is the importance of short and long range magnetic order for the stabilization of the charge gap in LaMnPO?

This question can be addressed by measuring the temperature dependence of Δ, using optical transmission measurements $T(\omega)$ through a single crystal of LaMnPO for temperatures up to 725 K. Therefore, we provided single crystals of LaMnPO to our collaborator Prof. Dimitri Basov and his graduate student Kirk Post at UC San Diego who performed optical spectroscopy measurements. The transmission as a function of photon energy $T(\omega)$ is shown in the inset to Fig. 3.6a at T = 295 K and 500 K. With increasing ω, a rapid decrease of $T(\omega)$ is observed, consistent with the onset of absorption due to optical excitations across the energy gap Δ. Fig. 3.6a presents $[\log(T)/\omega]^2$ for temperatures from 295 K to 725 K, where Δ is extracted from linear fits [66]. Δ decreases approximately linearly with increasing temperature (Fig 3.6b), by
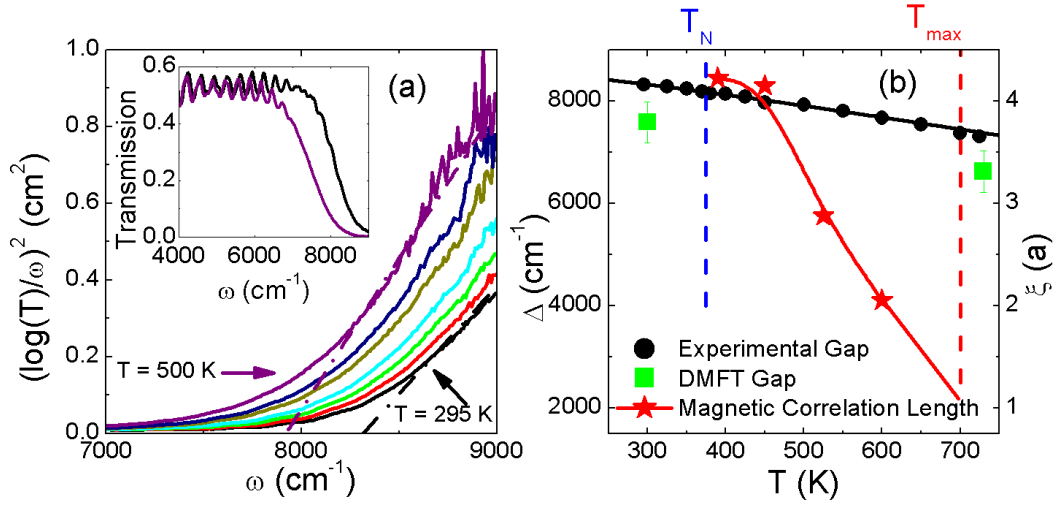
Figure 3.6: (Color online) (a) (Log(Transmission)/wavenumber)^2 at T = 295 K (-), 325 K (-), 350 K (-), 380 K (-), 425 K (-), 450 K (-), 500 K (-). Dashed lines are fits to the 295 K and 500 K data as described in the text. Inset: Transmission data for 295 K (black) and 500 K (purple) [23] (b) The temperature dependence of the experimental direct gap Δ ($\bullet$), Δ in the AF and PM states determined from DFT+DMFT calculations ($\bullet$), and the experimental AF correlation length ξ.

≈ 10% between 300 K and 725 K. These data project a 10 % reduction in Δ by 725 K, where $\xi \rightarrow$ a, just as predicted above. In addition, Δ(T) is featureless at T_N, showing that the exchange interaction alone cannot be responsible for the charge gap in LaMnPO , which is consequently not a Slater insulator. Given that the exchange interaction plays a small role in gap formation, we turned our collaborators Prof. Gabriel Kotliar and his postdoctoral researcher Dr. Zhiping Yin who performed to electronic structure calculations to investigate further the origin of the gap.

The importance of correlations for the charge gap in LaMnPO in the AF state has previously been emphasized [43]. Here, we present new DFT+DMFT calculations [23] of the electronic structure of LaMnPO that show Hund's coupling J_H plays a decisive role for the formation of a charge gap in the PM state, even when long range magnetic order is no longer present. We begin by presenting in Fig 3.7a the calculated electronic structure along high symmetry directions in the PM state, using an unreasonably large Hubbard U = 10 eV [5, 67, 68]. Here, LaMnPO is found to be a metal as there are bands crossing the Fermi level, in direct contradiction to the measured gap Δ = 1 eV. Thus, we can conclude that U is not solely responsible for the charge gap, and LaMnPO cannot be considered a conventional Mott-Hubbard insulator.

Recently, it has been established that J_H is important for the correlations in multi-orbital transition metal systems such as the Fe-pnictides [14, 50, 67, 69, 70]. The first of Hund's empirical rules is that energy is minimized for a maximum spin S on an isolated atom. For Mn^{2+} ions Hund's rule fills all five 3d orbitals with parallel spins to maximize S. This results in a significant energy cost in hopping between atoms as any doubly occupied orbitals would reduce S. Consequently, it has been emphasized that J_H stabilizes the gap at half filling, i.e. d^5 Mn, and reduces the gap for other fillings [15] as outlined in the introduction to this thesis.

The role of Hund's coupling is highlighted in Fig. 3.7b, which presents a DFT+DMFT calculation in the PM state that includes both J_H = 0.9 eV, along with a more realistic value of U = 8 eV [68]. The inclusion of J_H shifts the bands away from the Fermi level, opening a gap. Paramagnetic LaMnPO has evolved, by including Hunds coupling, from a moderately correlated metal (U = 10 eV, J_H = 0 : Fig 3.7a) to a bona fide insulator (U = 8 eV, J_H = 0.9 eV : Fig 3.7b).

Does the presence of AF order significantly affect the magnitude of the gap? Fig 3.7c presents a DFT+DMFT calculation of LaMnPO in the AF state for the same U = 8 eV, J_H = 0.9 eV (a similar calculation was previously reported but for U = 6 eV, J_H = 0.9 eV [31]). Energy cuts from Fig 3.7b,c of the spectral function $A(k,\omega)$ at high symmetry points are presented in Fig 3.7d.
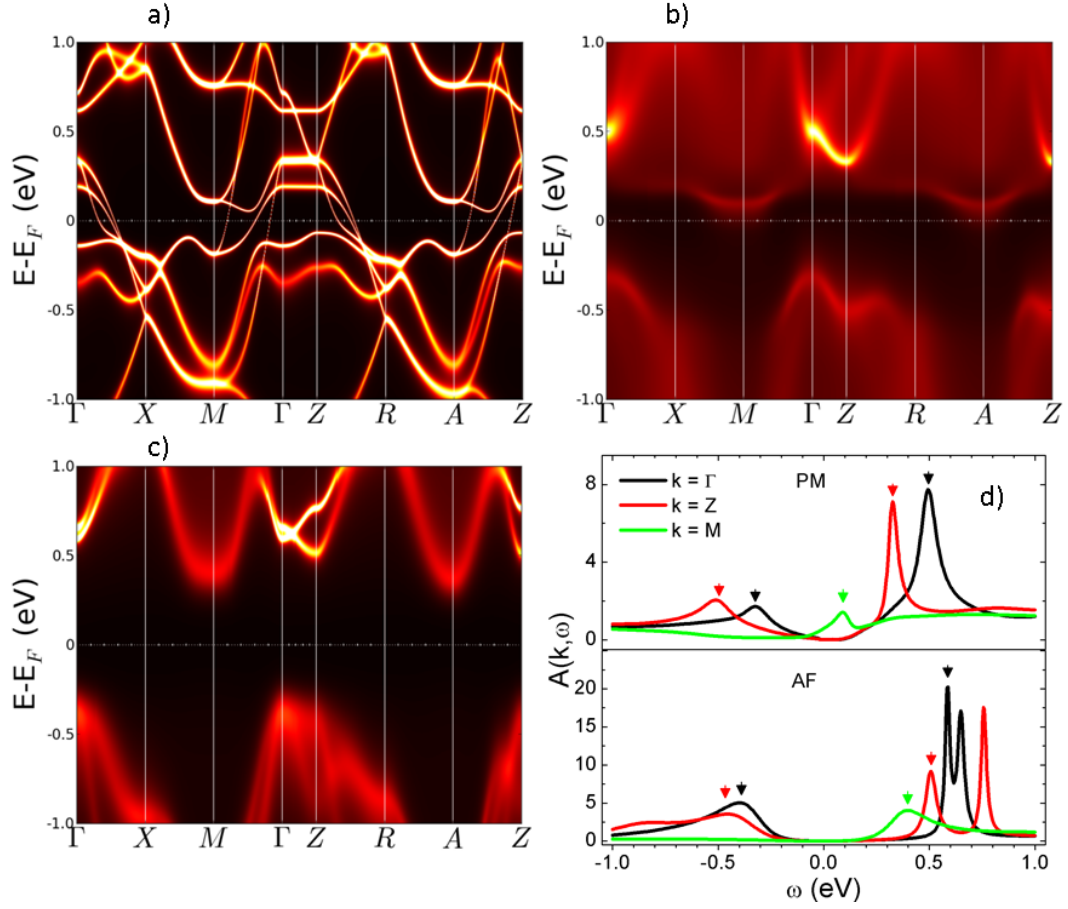
Figure 3.7: Density functional theory + dynamical mean field theory (DFT+DMFT) calculations of the band structure of LaMnPO (a) Paramagnetic (PM) state with Hubbard U = 10 eV and Hund's J_H = 0 eV (b) PM state with U = 8 eV and J_H = 0.9 eV (c) Antiferromagnetic (AF) state with U = 8 eV and J_H = 0.9 eV (d) Spectral function A(k,ω) at high symmetry points for the calculations shown in (b,c). Triangles indicate peak position of A(k,ω) [23].

The direct charge gaps, defined from the maxima of $A(k,\omega)$, are calculated to be rather insensitive to AF order and are in good agreement with the experimental values (Fig 3.6b), showing that Δ is well accounted for when J_H is considered as well as U. The indirect gap is defined from the conduction band minimum at M to the valence band maximum at Γ (Fig. 3.7d). While the indirect gap has decreased substantially from 0.74 ± 0.05 eV in the AF state to 0.4 ± 0.05 eV in the PM state, it is still much larger than the activation gap of 0.1 eV found in resistivity measurements [52], suggesting that the conduction in LaMnPO is still dominated by in-gap states in the paramagnetic phase.

3.4   Discussion

We have presented a combined experimental and theoretical study of LaMnPO that shows that exchange coupling J plays a minimal role in determining the charge gap Δ. The argument rests on three observations. First, there is only a 10% reduction in Δ between T_N and the mean field temperature, where the magnetic moments are no longer coupled. Secondly, J sets the scale for the fraction of Δ that can vanish for $T \gg T_N$ and we fit the spin waves detected in inelastic neutron scattering measurements to the Heisenberg model to show that $J \approx 0.1\,\Delta$. Finally, electronic structure calculations show that Δ persists in the absence of AF order, prompting our identification of LaMnPO as a Mott-Hunds insulator, where the intra-atomic Hubbard U and Hund's J_H are primarily responsible for the charge gap.

Although LaMnPO shares the insulating AF ground state of the cuprates, its multiorbital nature and the strong Hunds coupling J_H associated with its half-filled Mn d-shell establish that it is a more strongly correlated and thus insulating version of the metallic Fe-based pnictides. Substantial charge fluctuations are observed in LaMnPO relative to the d^5 (Mn^{2+}) state [31], and high pressures drive the transition to a metallic state, followed at higher pressures by the collapse of AF order [54]. This strong d^5 character leading to half-filled orbitals due to the strong Hund's coupling, is likely to dominate well into the metallic state, making LaMnPO substantially more correlated than isostructural LaFeAsO [15]. So far, no superconductivity has been observed in pressurized LaMnPO but superconductivity in pressurized MnP below 1 K has recently been observed [48]. While it may be tempting to ascribe this to overly strong electronic correlations, it is possible that LaMnPO, like the cuprates, requires doping as well as pressure to drive superconductivity. Often the highest superconducting transition temperatures require metallization accompanied by the collapse of AF order. Despite the multiorbital character associated with Hund's coupling, these conditions have been met in other

Mott-Hund's insulators [71].

Chapter 4

Ba$_{1-x}$K$_x$Mn$_2$As$_2$

We first present optical reflectance measurements of single crystals of the antiferromagnetic insulator BaMn$_2$As$_2$ that are rather temperature independent and do not display the broad hump centered around 60 meV that was previously interpreted as the charge gap. Instead our optical reflectance measurements reveal intereference fringes below 0.86 eV indicating that the direct charge gap in BaMn$_2$As$_2$ is 0.86 eV, an order of magnitude larger than previously reported. To clarify these results we performed optical transmission measurements, which are our most accurate measurement of the charge gap. Single crystals of BaMn$_2$As$_2$ are transparent below 0.86 eV and become opaque above this energy, further confirming the magnitude of the charge gap Δ = 0.86 eV. Density functional theory plus dynamical mean field theory (DFT+DMFT) calculations correctly reproduce this charge gap only when a strong Hund's coupling is considered, as well as Hubbard U. Thus, BaMn$_2$As$_2$ is a member of a wider class of Mn pnictide compounds that are Mott-Hund's insulators. We also present optical reflectance for metallic 2% K doped BaMn$_2$As$_2$ that we use to extract the optical conductivity at different temperatures. The optical conductivity $\sigma_1(\omega)$ exhibits a metallic response that is well described by a simple Drude term. Both $\sigma(\omega{\rightarrow}0,\ T)$ and $\rho(T)$ exhibit Fermi liquid temperature dependencies. From these measurements, we argue that a more strongly correlated Hund's metal version of the parent compounds of the iron pnictide superconductors has not yet been realized by doping this class of Hund's insulators. The work presented in this chapter has been published as [24]

4.1 Introduction

In Chapter 3, we presented an experimental and theoretical approach to evaluate the relative importance of long range magnetic order, magnetic exchange

interactions J, Hund's coupling J_H and Hubbard U for the formation of a charge gap in LaMnPO. High temperature inelastic neutron scattering and optical transmission measurements revealed that exchange interactions were much smaller than the direct charge gap of $\approx$ 1 eV in LaMnPO that persists into the high temperature paramagnetic phase. DFT+DMFT showed that a strong Hund's coupling $J_H = 0.9$ eV is crucial for the formation of the gap. Here, we present the results of applying a similar methodology to the related compound $BaMn_2As_2$.

$BaMn_2As_2$ adopts the $ThCr_2Si_2$ structure, which is qualitatively similar to the ZrCuSiAs structure adopted by LaMnPO (Figure 4.1), consisting of square nets of Mn atoms, tetrahedrally co-ordinated by pnictogen atoms [72]. $BaMn_2As_2$ is an antiferromagnetic insulator with an ordering temperature of $T_N = 625$ K and ordered magnetic moment of 3.9 μ_B/Mn [73]. This large ordered moment, compared with the 3.2 μ_B moment of LaMnPO [43], suggests valence fluctuations in $BaMn_2As_2$ are weaker than LaMnPO, and the effects of Hund's coupling should be just as important for the formation of a charge gap.

However, the direct charge gaps in $BaMn_2As_2$ previously reported from optical reflectance (0.024 eV [74]), ARPES (0.15 eV [46]) and DFT (0.1 eV [75], 0.058 eV [46]), are an order of magnitude smaller than those found in related Mn pnictide systems such as LaMnXO (X = P, As, Sb) [76]. We have shown in Chapter 3 that Hund's coupling is crucial for the formation of a charge gap on the order of 1 eV and so these reports of a drastically reduced charge gap in $BaMn_2As_2$ are inconsistent with our expectation for this class of compounds.

To clarify the magnitude and origin of the charge gap in undoped and insulating $BaMn_2As_2$ we present optical transmission and reflectance measurements and DFT+DMFT calculations. Our optical measurements determine a charge gap of 0.86 eV in undoped $BaMn_2As_2$, an order of magnitude larger than previous reports [74] and very similar to values found in other square-net Mn compounds [76]. DFT+DMFT calculations correctly reproduce the measured charge gap only when a large $J_H = 0.9$ eV is included, as well as Hubbard U = 8 eV.

We also present optical reflectance measurements on a 2% K doped single crystal of $BaMn_2As_2$ that find metallic behavior, characterized by the appearance of a Drude peak. The optical conductivity $\sigma(\omega)$ is extracted from the reflectance by Kramers-Kronig analysis and we find that $\sigma_1(\omega)$ is well described by one Drude term. The temperature T-dependence of both the electrical resistivity and $\sigma_1(\omega \to 0)$ is as expected for a Fermi liquid for T = 1.8 K - 300 K.
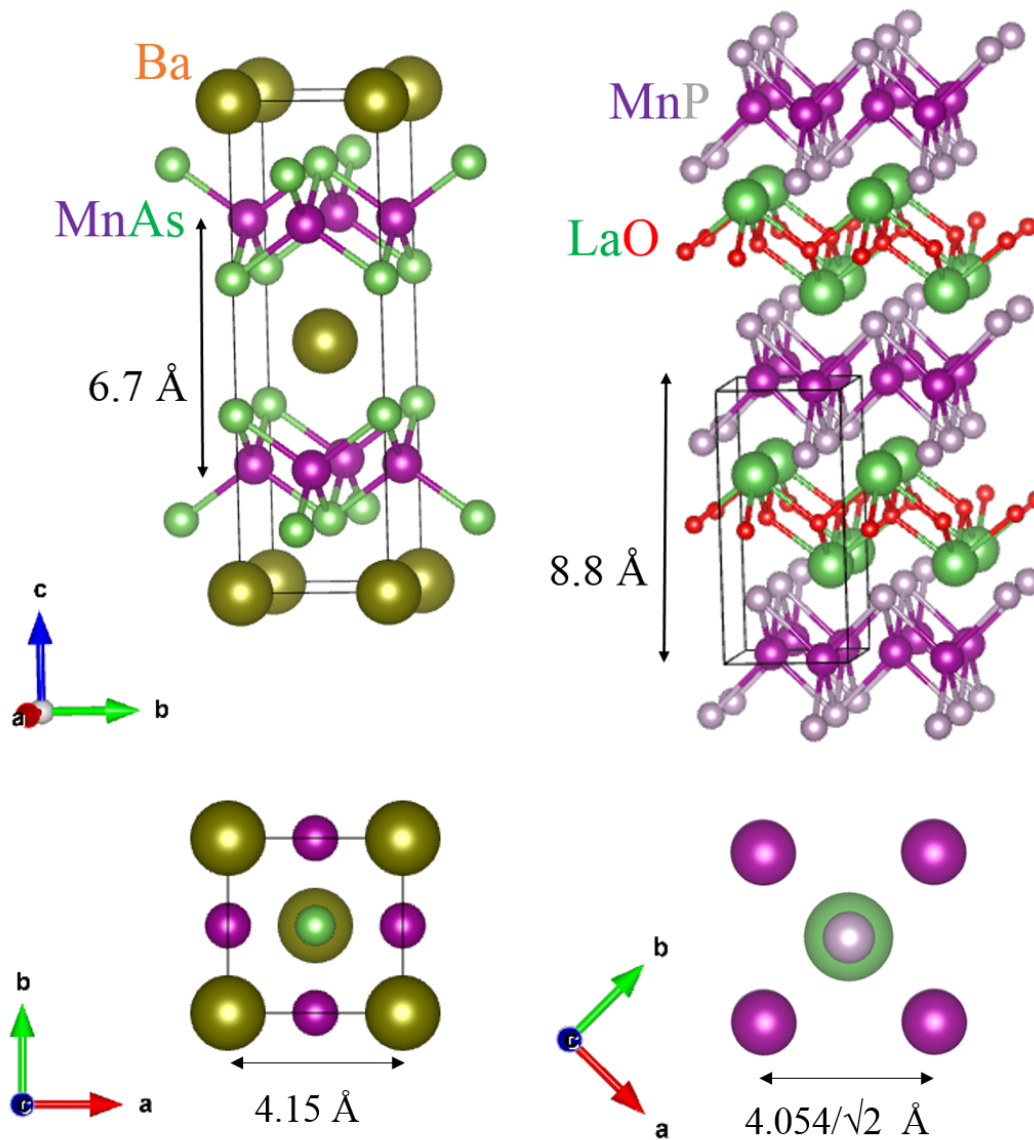
Figure 4.1: (left) The tetragonal a = b = 4.15 Å, c = 13.47 Å ThCr$_2$Si$_2$ (S.G. I4/mmm) structure adopted by BaMn$_2$As$_2$. (right) The tetragonal a = b = 4.054 Å, c = 8.834 Å ZrCuSiAs (S.G. P4/nmm) structure adopted by LaMnPO. (bottom) Top view of the crystal structures emphasizing the square nets form my Mn ions.

4.2 Experimental Details

We grew single crystals of $BaMn_2As_2$ and 2% K doped $BaMn_2As_2$ from a Sn flux as detailed in Chapter 2. The presence of 2% K was confirmed by energy dispersive x-ray spectroscopy using a SEM JEOL 7600F, and the previously reported $ThCr_2Si_2$ structure [29] was confirmed by x-ray diffraction using a Bruker D8 Advance x-ray diffractometer. Electrical resistivity and heat capacity measurements were performed using a Quantum Design Physical Properties Measurement System. Magnetization measurements were performed using a Quantum Design Magnetic Properties Measurement System.

Optical reflectance measurements were performed on Bruker IFS 113v and Vertex 80v Fourier transform spectrometers. Reflectance was measured on polished single crystal samples at a near-normal angle of incidence from 2 meV to 3 eV using an in situ overcoating (overfilling) technique [77]. Infrared transmission measurements were carried out on single crystals of $BaMn_2As_2$ using a Bruker LUMOS FT-IR Microscope with a KBr window. These data were normalized to an open channel by keeping all other conditions the same but moving the sample out of the way.

The electronic structure of $BaMn_2As_2$ was determined using DFT + DMFT [4, 78], which is based on the full-potential linear augmented plane wave method implemented in Wien2K [79], using the generalized gradient approximation to the exchange-correlation functional [80]. We use the atomic positions taken from the experimentally determined crystal structure [29]. The convergence of the calculations with respect to number of k points, charge density, total energy, Fermi level, self-energy reached a level similar to previous publications [31, 50].

4.3 Experimental Results and Analysis

Figure 4.2 presents a comparison of the magnetization and specific heat of our single crystals of $BaMn_2As_2$ and 2 % K-doped BaM_2As_2 with those previously reported. Figure 4.2a presents the previously reported magnetic susceptibility as a function of temperature in a field of 3 T applied in the ab plane and along the c-direction [72]. These data were corrected for a ferromagnetic MnAs ($T_c = 318$ K) impurity by recording magnetization curves at several temperatures, thus saturating the MnAs impurity and using the slope of high field linear magnetization as the intrinsic magnetic susceptibility of $BaMn_2As_2$. The anistropic temperature dependence of the magnetic susceptibility for fields applied in the ab plane and c-direction, as well as the low magnitude of the molar susceptibility, suggests $BaMn_2As_2$ is an antiferromagnet with moments along

59

the c-direction (see Figure 5.9 on page 95 of [12]). Indeed neutron diffraction revealed collinear long range antiferromagnetic order with moments along c-direction in $BaMn_2As_2$ with an ordering temperature $T_N = 625$ K [73]. The static magnetic susceptibility above T_N does not display a Curie-Weiss like temperature dependence up to the highest measured temperature of 1000 K (not shown here, see [13]), suggesting that spin correlations persist well above T_N, as is the case in LaMnPO (see Chapter 3). Figure 4.2c presents our measurements of the magnetic susceptibility of $BaMn_2As_2$ with a field of 3 T applied in the ab plane. The magnitude and temperature dependence of the magnetic susceptibility is similar to that previously reported (Figure 4.2a). We did not detect any ferromagnetic MnAs impurity in our crystals, so the raw data are presented. These data show that our $BaMn_2As_2$ crystals display the same magnetic behavior as previously reported [72].

Figure 4.2b presents the previously reported magnetic susceptibility of 2% K-doped (red points) and 5% K-doped (blue points) $BaMn_2As_2$ as a function of temperature in a field of 3 T applied in the ab plane [46]. Figure 4.2d presents the same measurement on our 2% K-doped $BaMn_2As_2$ crystals. For both sets of measurements the magnetic susceptibility is slightly enhanced compared to the undoped compound, likely due to the emergence of ferromagnetic fluctuations that eventually lead to ferromagnetic ordering of As holes at higher K dopings [81]. The origin of the weak feature near 50 K in both our measurements and previously reported measurements in a sample with 5% K doping may also be related to this ferromagnetism. Overall, the magnetic susceptibility of our single crystals of 2% K-doped $BaMn_2As_2$ is similar to that previously reported [46].

Figure 4.2e presents the previously reported specific heat C divided by the temperature T as a function of T^2 for 2% K-doped (red points) and 5% K-doped $BaMn_2As_2$ (green points). Figure 4.2f presents the same data for our 2% K-doped $BaMn_2As_2$ crystals. For both sets of measurements there is a non-zero vertical axis intercept, i.e. a Sommerfeld coefficient $\gamma = C/T$ for T $\rightarrow$ 0. This corresponds to a non-zero density of states at the Fermi level, consistent with the metallic behavior observed by electrical resistance and optical reflectance measurements described below. Overall, the magnetic and thermal properties of our K-doped and undoped $BaMn_2As_2$ are in very good agreement with those previously reported.

Figure 4.3 shows that $BaMn_2As_2$ is an insulator. The electrical resistivity $\rho(T)$ measured with the current in the ab plane is presented in Figure 4.3a and is found to increase with decreasing temperature T down to 1.8 K. The inset shows that at low temperatures $\rho(T)$ is well described by activated T-dependence $\rho \propto \exp(\epsilon_A/ k_B T)$, with an activation gap $\epsilon_A = 13$ meV, in
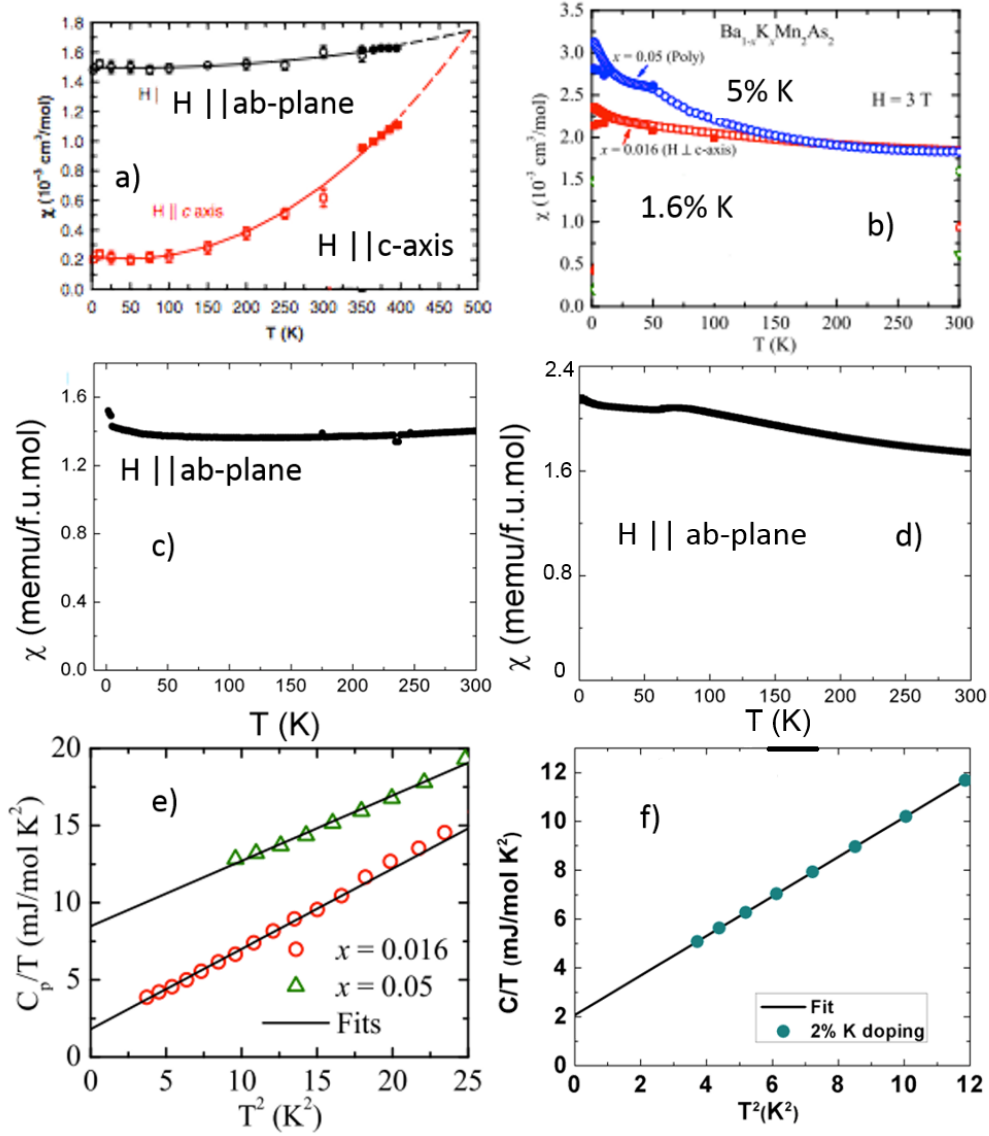
Figure 4.2: (a) Previously reported magnetic susceptibility as a function of temperature for H = 3 T for BaMn$_2$As$_2$ [72] (b) Previously reported magnetic susceptibility as a function of temperature for H = 3 T for K-doped BaMn$_2$As$_2$ [46] (c) Our magnetic susceptibility measurement as a function of temperature for H = 3 T for BaMn$_2$As$_2$ (d) Our magnetic susceptibility measurement as a function of temperature for H = 3 T for 2 % K-doped BaMn$_2$As$_2$ (e) Previously reported specific heat as a function of temperature for K-doped BaMn$_2$As$_2$ [46] (f) Our specific heat measurement as a function of temperature for 2 % K-doped BaMn$_2$As$_2$

61

reasonable agreement with previous reports [72]. To further investigate the electrical and optical properties of $BaMn_2As_2$ we provided single crystals to our collaborator Dr. Chris Homes at BNL. Figure 4.3b presents high resolution optical reflectance of a single crystal of $BaMn_2As_2$ as a function of wavenumber for T = 6 K - 295 K. The overall reflectance is rather low, consistent with insulating behavior, and exhibits little T-dependence. The sharp features at ≈ 80 cm^{-1} and 200 cm^{-1} correspond to phonons. The energy scale associated with these phonons (< 30 meV) is similar to that previously reported from powder inelastic neutron scattering measurements (Figure 3 in [13]). These phonon modes were also observed in previously reported optical reflectance measurements by Antal et al. who further provided a modelling of the phonon modes for the $ThCr_2Si_2$ structure [74]. This modelling ruled out the temperature dependent feature they observed at ≈ 500 cm^{-1} as a phonon mode, and they thus assigned this feature (marked by arrow in Figure 4.3d) to the energy gap. However, we have not been able to reproduce this T-dependent feature or the overall T-dependent reflectance [74]. Furthermore, Figure 4.3c shows the optical reflectance as a function of wavenumber, with interference fringes below 6900 cm^{-1}, indicating that $BaMn_2As_2$ is transparent and insulating below these wavenumbers. The fringes vanish above 6900 cm^{-1}, consistent with the onset of absorption for energies above the charge gap $\Delta = 0.86$ eV.

To investigate further the magnitude of the charge gap in $BaMn_2As_2$ we provided single crystals to our collaborators Prof. Basov and his graduate student Kirk Post at UC San Diego. Room temperature optical transmission as a function of wavenumber is presented in Figure 4.4a. At ≈ 6500 cm^{-1} a rapid decrease of transmission is observed, consistent with the onset of absorption due to optical excitations across a charge gap $\Delta = 0.86$ eV, significantly larger than the previously reported charge gap of 0.024 eV [74]. Figure 4.4b shows that the reduced transmission below ≈ 2000 cm^{-1} is well accounted for by a model of Lorentzian-like oscillators including some small intra-gap absorption, which may be due to in gap states or Sn inclusions [82]. We emphasize that we used single crystals for our optical spectroscopy and $\rho(T)$ (Fig 4.3a) measurements that were taken from the same batch. Overall, our optical transmission measurements are in good agreement with our optical reflectance measurements that show the charge gap in $BaMn_2As_2 = 0.86$ eV, an order of magnitude larger than previously reported.

We turned to our collaborators Prof. Gabriel Kotliar and his postdoctoral researcher Dr. Zhiping Yin at Rutgers, who performed electronic structure calculations to investigate further the origin of the gap in $BaMn_2As_2$. Figure 4.5 shows that the charge gap in $BaMn_2As_2$ results from strong Hund's coupling. First, in Figure 4.5a, we present a DFT+DMFT calculation for Hubbard U
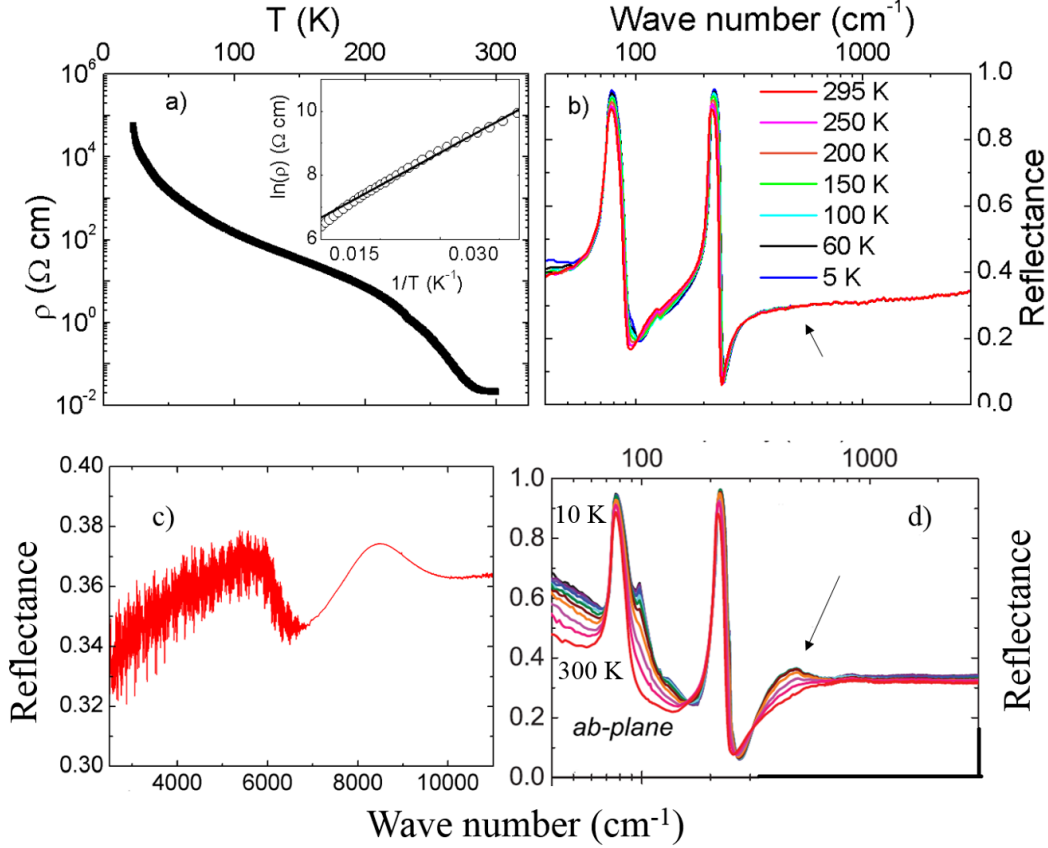
Figure 4.3: (a) Resistivity ρ of BaMn$_2$As$_2$ as function of temperature T measured in the ab plane. (inset) $\ln(\rho)$ versus T^{-1}. The solid line is a fit to the Boltzmann expression as described in the main text (b) Optical reflectance measured in the ab plane for temperatures T = 295 K (red), 250 K (magneta), 200 K (orange), 150 K (green), 100 K (cyan), 60 K (black) and 5 K (blue). (c) Optical reflectance measured in the ab plane at room temperature at higher wavenumbers. (d) Previously reported optical reflectance as a function of wavenumber for range of temperatures from 10 K to 300 K. Data reproduced from [74]. The arrow indicates the temperature-dependent feature previously assigned as the energy gap that we do not observe in our measurements presented in Figure 4.3b.
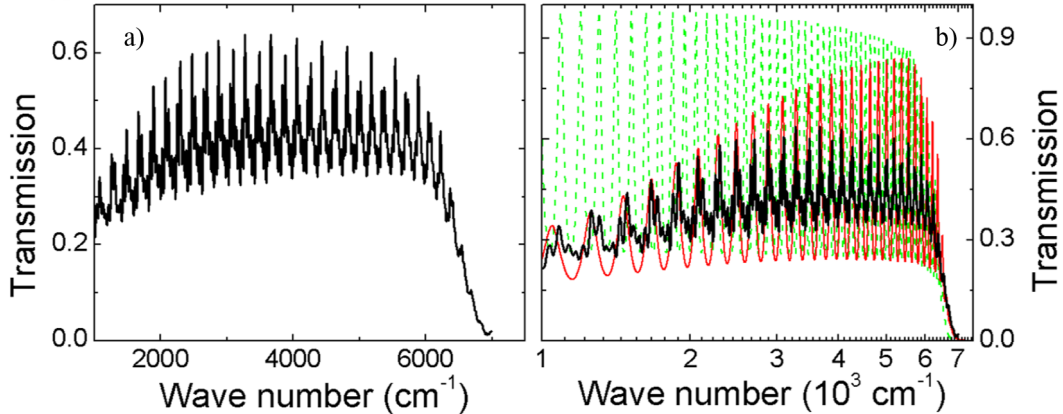
Figure 4.4: (a) Optical transmission of a single crystal of $BaMn_2As_2$ measured in the ab plane at room temperature. (b) Optical transmission measured in the ab plane at room temperature (black) and a model of the optical transmission with (red) and without (green dash) intra-gap absorption.

= 8 eV with no Hund's term ($J_H = 0$). Several bands are crossing the Fermi level, and so, in the absence of Hund's interactions, $BaMn_2As_2$ is predicted to be metallic, contrary to our resistivity and optical spectroscopy measurements that find insulating behavior. Figure 4.5b presents DFT+DMFT calculations for Hubbard U = 8 eV and $J_H = 0.9$ eV, the same parameters used for the related compound LaMnPO [23]. The inclusion of Hund's coupling severely modifies the band structure. Now, there are no bands crossing the Fermi level and $BaMn_2As_2$ is found to be insulating, in agreement with our experiments. Further, a direct charge gap of ≈ 0.8 eV (Figure 4.5c) is found at the Γ point that is in excellent agreement with the experimental value $\Delta = 0.86$ eV found from our optical measurements presented in Figures 4.3, 4.4.

Using our experimental and theoretical results, we now situate $BaMn_2As_2$ amongst archetypal layered Mn pnictide compounds LaMnXO and $BaMn_2X_2$ (X = P, As) (Figure 4.5d). First, we discuss the experimentally determined activation gaps ϵ_A and charge gaps Δ. The values of ϵ_A determined from electrical resistivity measurements with the current flowing in the ab plane range from 0.027 - 0.2 eV, while the optical gaps range from $\Delta = 0.86$ - 1.4 eV. Thus, ϵ_A likely corresponds to the energy differences between in-gap states, possibly originating from impurities, and the conduction band edge. In contrast, Δ corresponds to the direct charge gap that separates the valence and conduction bands. DFT calculations find a direct charge gap of similar magnitude to the activation gaps, which is order of magnitude smaller than the experimentally determined charge gaps. On the other hand, DFT+DMFT calculations in-

cluding a strong Hund's coupling correctly reproduce the measured charge gap. These calculations assert that including strong electronic correlations is crucial to properly understand the insulating state of Mn pnictide systems [23, 34]. It has also been emphasized that Hund's coupling is responsible for the mass enhancement observed in the parent compounds of the iron pnictide superconductors [50]. Thus, driving the strongly correlated Mn pnictide Hund's insulators across an electronic delocalization transition where $\Delta \rightarrow 0$ could potentially lead to a more correlated version of the Fe pnictides, and perhaps even higher temperature superconductivity. While a metal-insulator transition has been realized in K-doped $BaMn_2As_2$, this sample was not found to be superconducting [46]. We now present $\rho(T)$ and optical spectroscopy measurements that address the metallization of 2% K doped $BaMn_2As_2$. These measurements were performed by our collaborator Dr. Chris Homes at BNL on single crystals of K-doped $BaMn_2As_2$ that we provided.

The temperature dependence of the electrical resistivity of 2% K doped $BaMn_2As_2$ is presented in Figure 4.6a. A metallic $\rho(T) = \rho_0 + A\,T^2$ temperature dependence typical of a Fermi liquid is observed, with A = 0.09 $\mu\Omega$ cm K^{-2}. The measured T-dependence is similar to that previously reported [46] but our crystals have slightly lower $\rho_0 = 0.54$ mΩ cm and a larger residual resistivity ratio $\rho(300 \text{ K})/\rho(2 \text{ K}) \approx 12$, indicating good sample quality. The optical reflectance $R(\omega)$ of $K_{0.02}Ba_{0.98}Mn_2As_2$ at different temperatures is presented in Figure 4.6b. A strong temperature dependence is observed with the reflectance increasing as the temperature decreases, consistent with the formation of a metallic state upon chemical doping. The real part of the complex optical conductivity σ_1 was determined from $R(\omega)$ via a Kramers-Kronig analysis. Below the lowest measured frequency point, the Hagen-Rubens form has been used for the reflectance, $1 - R(\omega) \propto \sqrt{\omega}$, and above the highest-measured frequency point the reflectance was assumed to be constant up to 5×10^4 cm^{-1}, above which a free-electron $1/\omega^4$ response was assumed. Figure 4.6c shows σ_1 at selected temperatures. All the spectra exhibit clear Drude-like responses, expected for metals.

In order to quantitatively analyze the optical data, we fit $\sigma_1(\omega)$ to the Drude-Lorentz model [66],

$$\sigma_1(\omega) = \frac{2\pi}{Z_0} \left[\frac{\omega_p^2}{\tau(\omega^2 + \tau^{-2})} + \sum_j \frac{\gamma_j \omega^2 \Omega_j^2}{(\omega_j^2 - \omega^2)^2 + \gamma_j^2 \omega^2} \right] \qquad (4.1)$$

where Z_0 is the vacuum impedance. The first term describes the free-carrier Drude response, characterized by the plasma frequency $\omega_p = 4\pi ne^2/m^*$, where n is the carrier concentration and m* is an effective mass, and a scattering rate $1/\tau$. The second term corresponds to a sum of Lorentz oscillators characterized
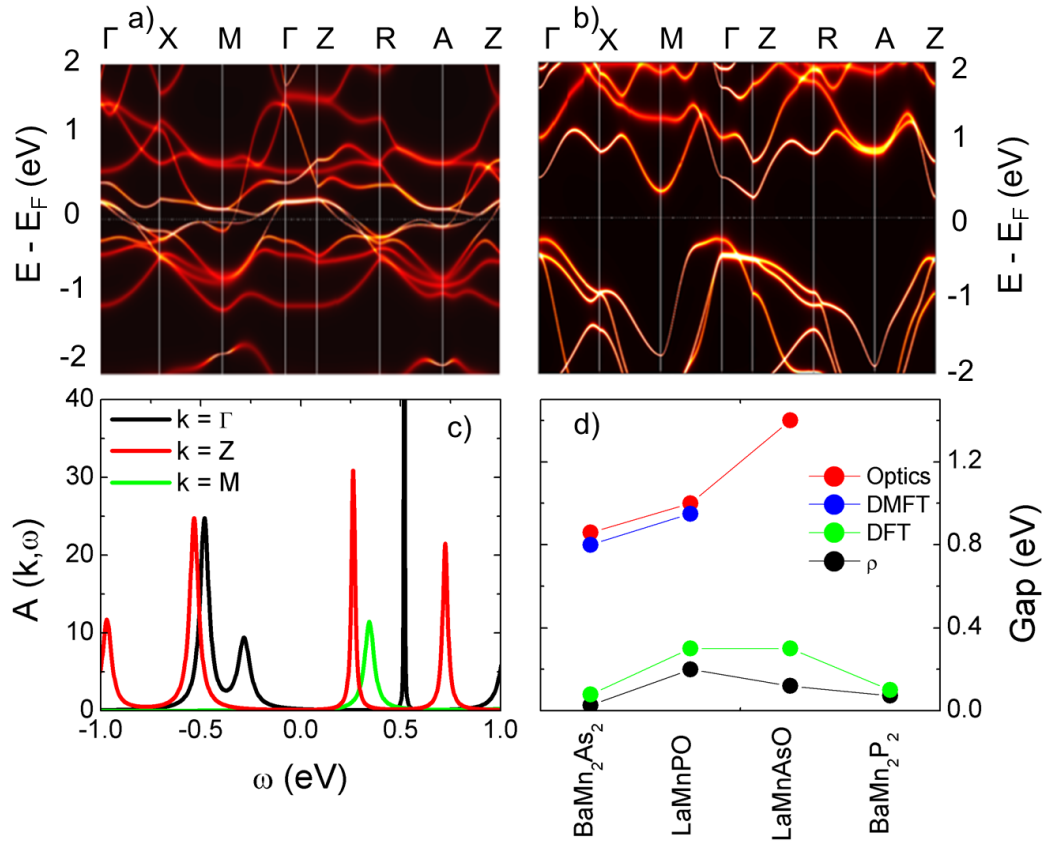
Figure 4.5: (Color online) (a) Density functional theory + dynamical mean-field theory (DFT+DMFT) calculation of the band structure of BaMn$_2$As$_2$ with Hubbard U = 8 eV and no Hund's coupling (J$_H$ = 0 eV). (b) DFT+DMFT of the band structure of BaMn$_2$As$_2$ with U = 8 eV and J$_H$ = 0.9 eV. (c) Spectral function at high symmetry points for the calculation shown in (b). (d) Summary of the activation gaps ϵ_A determined from electrical resistivity ρ measurements and charge gap Δ determined from different experimental and theoretical approaches in LaMnXO, BaMn$_2$X$_2$ (X = P, As) [23, 75, 76, 83].

by a resonance frequency ω_j, a linewidth γ_j, and an oscillator strength Ω_j.

We find that one Drude term, which we assign to the doped holes introduced by K, is sufficient to describe σ_1 (Figure 4.6c). As there are several hybridized Mn bands near the Fermi level in insulating $BaMn_2As_2$ (Figure 4.5b) one might expect several Drude terms to be necessary to describe the optical conductivity in metallic K-doped $BaMn_2As_2$. Therefore, this modelling is consistent with the observation that the ordered magnetic moment associated with Mn is not reduced by K doping [84] but remains localized while the observed metallic behavior is due to the doped holes introduced by the K, as previously emphasized [81, 85–87]. These results are in sharp contrast to $Ba_{1-x}K_xFe_2As_2$ (x=0.4), where two Drude terms corresponding to two different types of charge carriers are necessary to describe the optical conductivity, corresponding to multiple hole and electron pockets at the Fermi surface [88].
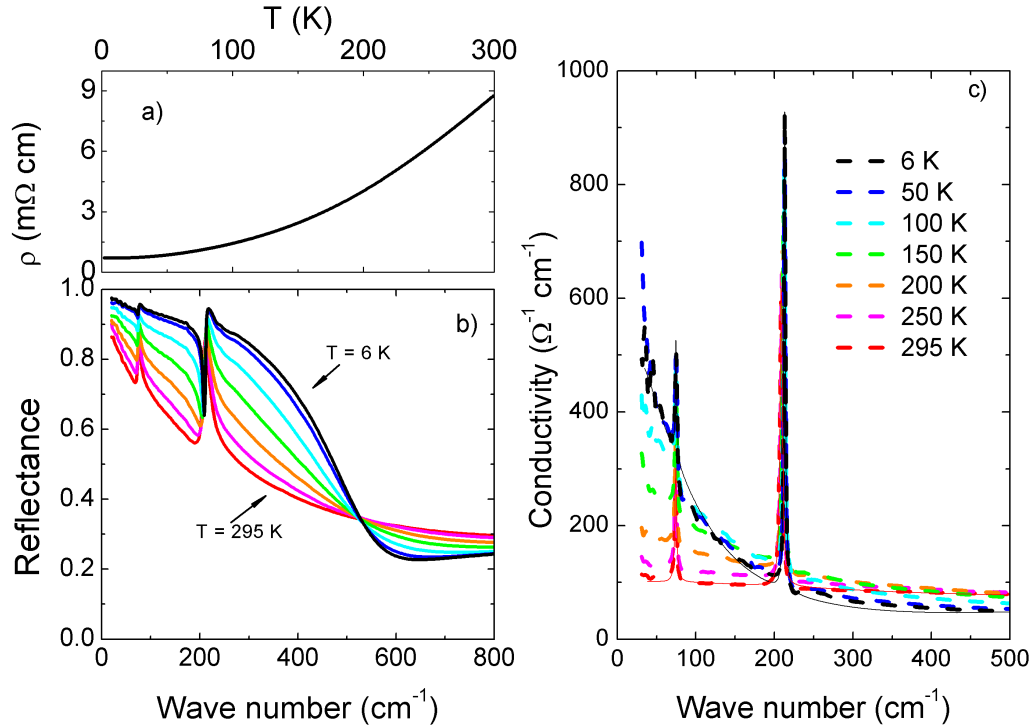
Figure 4.6: (Color online) (a) Temperature dependence of the electrical resistivity measured in the ab plane of a single crystal of $K_{0.02}Ba_{0.98}Mn_2As_2$ (b) Optical reflectance measured in the ab plane on a single crystal of $K_{0.02}Ba_{0.98}Mn_2As_2$ for temperatures indicated in (c). (c) Optical conductivity for different temperatures as indicated. Solid lines are fits to the 6 K and 295 K measurements as described in the main text.

Figure 4.7 shows the temperature dependencies of the Drude parameters taken from our fits. The plasma frequency (Figure 4.7a) is almost temperature independent, indicating that the band structure and n/m* do not change appreciably with temperature. The relatively small magnitude of the plasma frequency ≈ 1700 cm^{-1}, as well as the large value of the resistivity and the rather weak Drude peak, indicates that is a 'bad metal', as expected for only 2% K doping. This plasma frequency is substantially smaller than in the related compound Ba$_{1-x}$K$_x$Fe$_2$As$_2$ (x=0.4) where $\omega_{p1,p2} \approx 6000$ cm^{-1}, 14000 cm^{-1} [88]. Figure 4.7b presents the temperature dependence of the scattering rate of the Drude component, with $1/\tau \propto$ T^2; the dashed line denotes a T^2 fit that implies the charge carriers are described by Fermi liquid theory. The temperature dependencies of the dc optical conductivity $\sigma_1(\omega \rightarrow 0)$, resisitivity $\rho = 1/\sigma_1(\omega \rightarrow 0)$ and dc resistivity from electronic transport measurements are presented in Figure 4.7c,d. Excellent agreement is found between our optical spectroscopy and electrical resistivity measurements. In both cases, the behavior is well described by Fermi liquid theory, as previously observed and suggested to arise from hole-hole scattering [46].

4.4   Discussion

The parent state of the iron pnictide superconductors may be regarded as a Hund's metal [14, 15] and it is interesting to ask whether this is also the case for the isostructural Mn pnictide metals. There are two signature features of a Hund's metal: a reduction in the coherence scale for Fermi liquid behavior and the promotion of a metallic state away from half filling. For 2% K doped BaMn$_2$As$_2$ our optical conductivity and transport measurements find the dc resisitivity has a Fermi-liquid like T^2 dependence at all measured temperatures. Thus, 2% K doped BaMn$_2$As$_2$ may be viewed as a system of weakly interacting quasiparticles that does not display the unusual non-Fermi liquid properties $\rho(T) \propto T$ found in the metallic Fe pnictides [7]. The optical conductivity of 2% K doped BaMn$_2$As$_2$ is well described by hole conduction corresponding to the introduction of K dopants. This observation, combined with the result that the ordered magnetic moment remains robust in the K-doped metal [84], suggests the emergence of a metallic state does not promote significant valence fluctuations on the Mn site. Therefore, no signatures characteristic of a possible correlated Hund's metal state have been realized in this system.

Rather, K doping has transformed BaMn$_2$As$_2$ from a local moment antiferromagnetic insulator to a local moment antiferromagnetic metal where the doped holes are responsible for the conduction. The realization of a Hund's
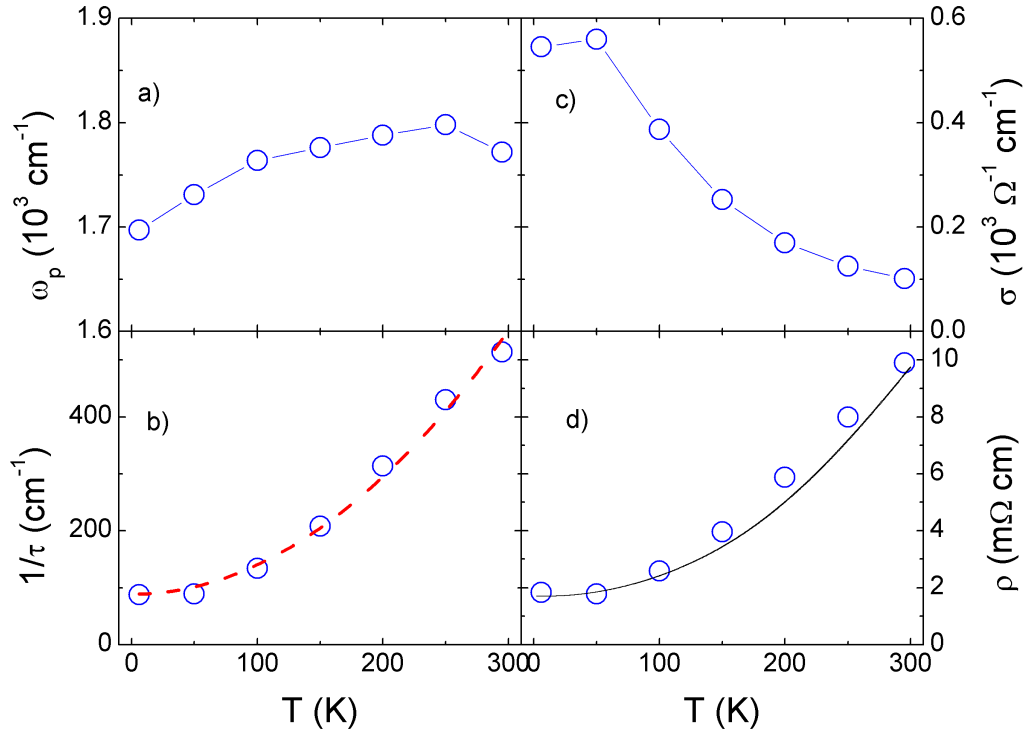
Figure 4.7: The temperature dependence of (a) the plasma frequency ω_p, (b) the scattering rate $1/\tau$, (c) the dc conductivity $\sigma(\omega{\to}0)$, and (d) the resistivity $1/\sigma(\omega{\to}0)$ and the corresponding dc resistivity from transport measurements. For clarity, the dc resistivity is offset by 1 mΩ cm compared to the same data presented in Figure 4.6a

metal and superconductivity requires the suppression of magnetic order, as well as metallization. At higher K doping in $BaMn_2As_2$ itinerant ferromagnetism due to a Stoner-type instability of the Fermi surface originating from the As 4p holes has been detected [81, 85], similar to that reported in H doped LaMnAsO [89]. Thus, doping Mn pnictide systems toward metallicity may generically lead to ferromagnetic fluctuations or even order, with limited suppression of the antiferromagnetic order. On the other hand, pressure was found to transform LaMnPO from an antiferromagnetic insulator to an antiferromagnetic metal at 20 GPa and eventually to a paramagnetic metal at 34 GPa [31, 54]. No ferromagnetism was detected and it appears to be the case that only pressure can transform Mn pnictide insulators into potentially correlated Hund's metals, a now familiar breeding ground for superconductivity. For example, recent experiments have shown the pressure-induced suppression of magnetic order in MnP reveals a superconducting state with $T_c \approx 1$ K [48].

Recently, x-ray magnetic circular dichroism measurements, combined with nuclear magnetic resonance and x-ray and neutron diffraction, have revealed that the itinerant ferromagnetism in $K_{0.4}Ba_{0.6}Mn_2As_2$ originates from holes doped into the As 4p band [81]. This is likely to also be the case in the related half-metal $Rb_{0.6}Ba_{0.4}Mn_2As_2$ [90]. There is an apparent decoupling of magnetic interactions between the As 4p states and the Mn 3d states. This is very surprising as the Mn and As atoms are in the same layer and significant hybridization between Mn and As states would be expected. These findings should stimulate further interest in chemically doping Mn pnictide compounds, such as pressurized LaMnPO and $LaMnSb_2$.

We have reported optical transmission and reflectance measurements of $BaMn_2As_2$ that find insulating behavior and a charge gap of 0.86 eV. The measured charge gap is an order of magnitude larger than previously reported and of similar magnitude to that of other Mn pnictide compounds. DFT+DMFT correctly reproduces the charge gap only when Hund's coupling is included. Using these results, we present $BaMn_2As_2$ as part of a wider class of layered Mn pnictide systems that we classify as Mott-Hund's insulators. We have also presented the optical conductivity of $K_{0.02}Ba_{0.98}Mn_2As_2$ that reveals a Drude peak, characteristic of a metallic state. A Fermi liquid like temperature dependence of $\sigma_1(\omega{\to}0,$ T$)$ and $\rho(T)$ suggests $K_{0.02}Ba_{0.98}Mn_2As_2$ should not be considered a correlated Hund's metal and thus is an unlikely candidate for high temperature superconductivity. While the outlook for suppressing the local moment antiferromagnetism in these systems by chemical doping remains challenging, the possibility of suppressing the moment by pressure is more positive. We believe a closer examination of the pressure dependence of the magnetic state of layered Mn pnictide compounds, for instance using high

pressure neutron scattering techniques, is warranted.

Chapter 5

CaMn$_2$Sb$_2$

Our single-crystal inelastic neutron scattering measurements reveal spin wave excitations in CaMn$_2$Sb$_2$ at T = 5 K << T$_N$. We will show that these excitations are well described by a Heisenberg model of spins on a corrugated honeycomb lattice, allowing us to characterize the antiferromagnetic exchange interactions J$_1$ and J$_2$, as well as the exchange interactions between nearest neighbors in the c-direction J$_c$. Using the exchange interactions determined in this way, we situate CaMn$_2$Sb$_2$ on the theoretical magnetic phase diagram, and find it is proximate to a tricritical point, and is consequently magnetically frustrated. The results presented in this chapter have been published as [25]

5.1   Introduction

As outlined in Chapter 1 magnetic frustration can occur in spin systems when constraints prevent the formation of a ground state satisfying all of the pairwise interactions [91]. The honeycomb lattice is an interesting manifestation of a spin system where frustration arises from competing further neighbor interactions, and this frustration is further enhanced by strong quantum fluctuations due to the low coordination number z=3.

   The system of interacting spins on a honeycomb lattice has attracted the attention of theorists for decades [92, 93], with more recent calculations proposing that a spin liquid state can be stabilized on this lattice [94–97]. Competition between first, second and third neighbor magnetic exchange interactions, J$_1$, J$_2$, and J$_3$, results in a rich magnetic phase diagram as shown in Figure 5.1 [92, 93]. For classical localized spins described by a Heisenberg Hamiltonian, Néel, stripy, zigzag and spiral magnetic orderings are possible depending on the relative strengths of these interactions. Further, three tricritical points marked as black squares in Figure 5.1, where three of these

types of long range magnetic order become degenerate, are predicted and the strongest frustration would be expected near these points [92].
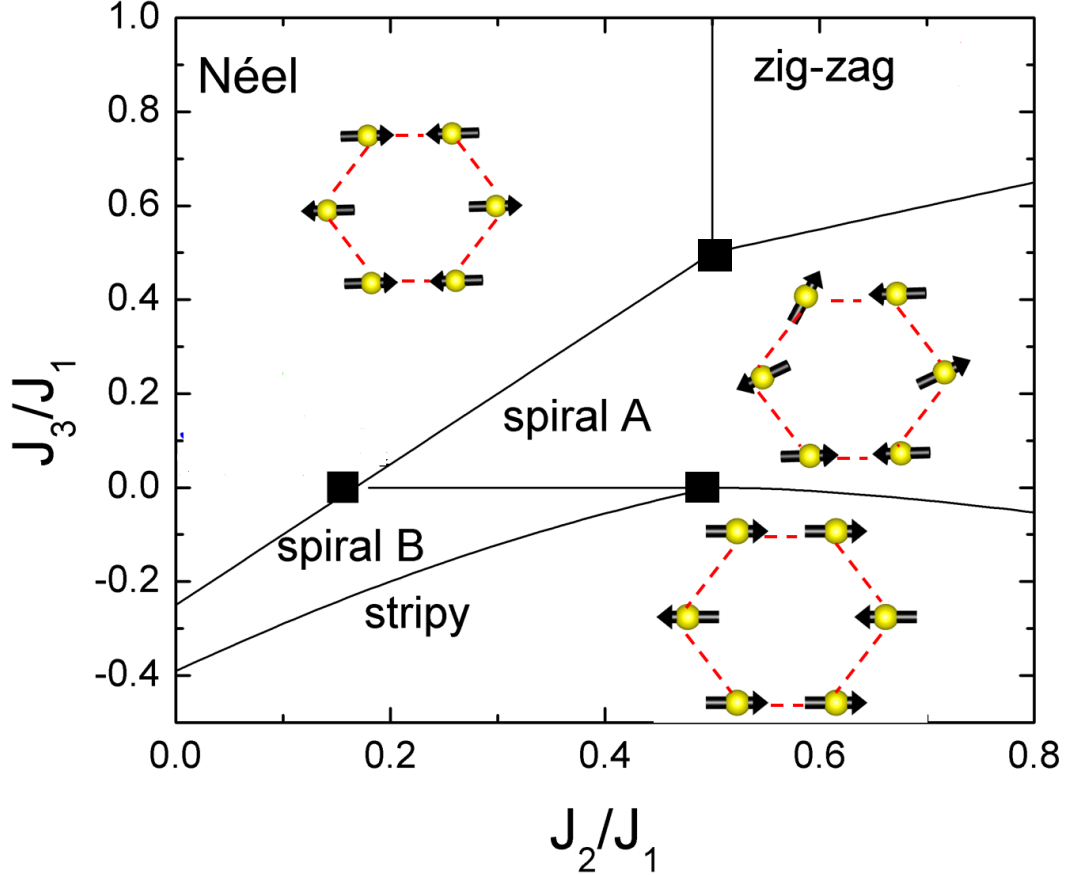
Figure 5.1: Phase diagram of the Heisenberg model for a honeycomb lattice with first, second and third neighbor exchange interactions J_1, J_2, and J_3 respectively [92]. The three black squares represent the three tricritical points, where three different types of long range magnetic order co-exist.

The honeycomb lattice compounds $MnTiO_3$ and $BaNi_2(PO_4)_2$ were discovered early on [98, 99]. Both were found to be Néel antiferromagnets with $MnTiO_3$ ordering at 64 K [100] and $BaNi_2(PO_4)_2$ ordering at 23.5 K [101], in agreement with the determined exchange interactions that place them deep in the Néel phase of the theoretical honeycomb lattice phase diagram [101, 102]. More recently, there have been several experimental realizations of frustrated honeycomb lattice systems with antiferromagnetic interactions based on transition metals, e.g. $Bi_3Mn_4O_{12}(NO_3)$ [103], $(Na/Li)_2IrO_3$ [104–106], α-$RuCl_3$ [107] SrL_2O_4 (L = Gd, Dy, Ho, Er, Tm, and Yb) [108], Cu_5SbO_6 [109],

and $Cu_3M_2SbO_6$ (M = Ni, Co) [110]. While inelastic neutron scattering measurements and complementary electronic structure calculations have placed bounds on the exchange interactions in $Bi_3Mn_4O_{12}(NO_3)$ [111–113] and Na_2IrO_3 [114, 115], determination of individual exchange interactions in these compounds has not been possible due to the lack of large single crystals and/or strong Ir absorption. Uncertainty remains over even the relative strength of the exchange interactions in these compounds. This has hindered comparison with theoretical phase diagrams, which propose spin liquid and highly frustrated phases depending on the value of the exchange interactions [94–97, 116].

We present inelastic neutron scattering results that characterize the exchange interactions in single crystals of the antiferromagnetic insulator $CaMn_2Sb_2$, which consists of honeycomb layers of Mn in which every other atom is shifted perpendicular to the ab plane (Figure 5.2a) [31, 117]. Neutron powder diffraction measurements reveal Néel-type antiferromagnetic order (Figure 5.2b) in $CaMn_2Sb_2$ below T_N = 85 - 88 K, with an ordered moment between 2.8-3.4 μ_B/Mn [118, 119]. The magnetic moment is substantially smaller than the 5 μ_B/Mn expected from the high spin state produced by Hund's rules, and this reduced moment may reflect the interplay of quantum fluctuations and hybridization [23, 43]. The moments are refined to lie in the honeycomb a-b plane, possibly with some degree of out-of-plane canting. Between T_N and 210 K a weak ferromagnetic component was detected in magnetic susceptibility measurements [31]. From 340 K - 400 K, Curie-Weiss behavior was reported with a low paramagnetic moment of 1.4 μ_B/Mn [31]. The low ordering temperature, as well as the unusual character of the intermediate temperature phase, suggest that frustration characteristic of the honeycomb lattice may be a crucial part of the magnetism of $CaMn_2Sb_2$, unaddressed until now.

5.2 Experimental Details

Single crystals of $CaMn_2Sb_2$ were prepared from a Sn flux as described in chapter 2. The trigonal crystal structure of $CaMn_2Sb_2$ (P$\bar{3}$m1, No. 164) with a = b = 4.52 Å and c = 7.46 Å was confirmed by single crystal x-ray diffraction down to temperature T = 8 K [31] (Figure 5.2a). Inelastic neutron scattering measurements were performed at the SEQUIOA time-of-flight spectrometer at the Spallation Neutron Source at Oak Ridge National Laboratory, TN. A collection of four single crystals of $CaMn_2Sb_2$ of total mass 3.2 g were coaligned on a sheet of aluminum. The crystals were mounted in a Displex helium closed cycle refrigerator with the **L** axis along the beam direction and the **H** direction perpendicular to the beam direction in the same horizontal
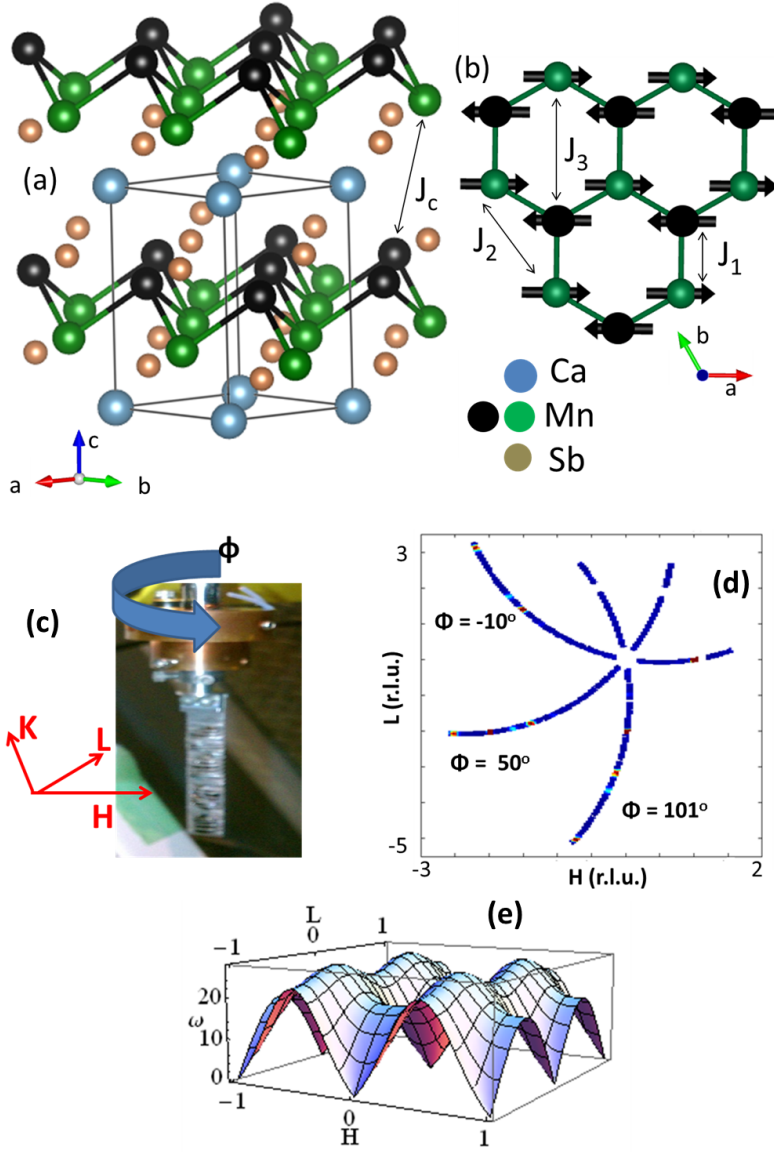
Figure 5.2: (a) The crystal structure of CaMn$_2$Sb$_2$. The corrugation of the honeycomb layer of Mn is emphasized by the black and green Mn atoms displaced along c-direction. (b) A compressed view of the Néel antiferromagnetic corrugated honeycomb lattice formed by the Mn moments in the ab plane. Exchange interactions between first neighbors J$_1$ and second neighbors J$_2$ are indicated. (c) Collection of aligned single crystals of CaMn$_2$Sb$_2$ on aluminum sheet. The angle Φ is indicated that represents rotation about an axis perpendicular to the H-L plane of CaMn$_2$Sb$_2$ (d) H-L space sampled by the detectors at SEQUIOA for incident energy of 50 meV and different Φ (e) The expected spin wave dispersion along **H** and **L**. [120]

plane (Figure 5.2c). We define $Q = \mathbf{b}_1$ h $+ \mathbf{b}_2$ k $+ \mathbf{b}_3$ l $= (\mathbf{H},\mathbf{K},\mathbf{L})$ where $\mathbf{b}_{1,2,3}$ are the reciprocal lattice vectors. The resulting Q-space coverage for our crystal at various orientations is shown in Figure 5.2d. The detectors at SEQUIOA cover a 90° area and so a limited amount of H-L space is sampled at fixed angle. To access a larger region of reciprocal space we rotate the crystal about the axis perpendicular to the H-L plane. For our measurements we rotated the sample about 111° in 1° steps. An incident energy of 50 meV with the Fermi chopper 2 set to 420 Hz and the T0 chopper set to 90 Hz was found to be optimal to sample the full excitation spectrum, with an energy resolution of 1 meV.

5.3 Experimental Results and Analysis

Figure 5.3 presents an overview of our inelastic neutron scattering measurements of $CaMn_2Sb_2$ at T = 5 K. The energy dependence of the scattered neutron intensity S(Q,E) along the H and L directions is presented in Figs. 5.3a and 5.3b. Sharp, dispersive excitations emerge from all reciprocal lattice points with integer h and l values, as expected for spin waves in the Neel phase of a honeycomb lattice (Figure 5.2e). Two spin wave branches are discernible, corresponding to an acoustic mode and an optical mode emanating from the antiferromagnetic zone center and 4 meV, respectively. The excitations are similar along the (H01) and (10L) directions, with a maximum spin wave energy of 24 meV in both cases. S(Q,E) is observed to decrease slightly as the wave vector increases, as expected from the magnetic form factor for Mn, acting in concert with the polarization-dependent scattering from the ordered magnetic moments [60, 121]. Figures 5.3c to 5.3f present two-dimensional cuts along the H and L directions for increasing energy transfers. For data summed over energy transfers 5 meV < E < 10 meV (Fig. 5.3c), we observe the most intense scattering in an oval shape centered at the Bragg position (h,k,l) = (1,0,0). For larger energy transfers (Figs. 5.3d and 5.3e), S(Q,E) has only a twofold rotational symmetry centered at the Bragg position, suggesting the spin waves disperse differently along the H and L directions. For 20 meV < E < 25 meV (Fig. 5.3f), the spin waves have dispersed to the edge of the Brillouin zone, consistent with a magnon bandwidth of 25 meV. The energy and wave-vector dependence of the scattered neutron intensity behave just as expected for three-dimensional spin waves.

$CaMn_2Sb_2$ is an insulator [31] and thus the Heisenberg model of localized moments is an appropriate starting point to describe the magnetic excitations. The corrugated honeycomb lattice formed by the magnetic Mn ions is non-Bravais and therefore the appropriate expression for the spin wave dispersion
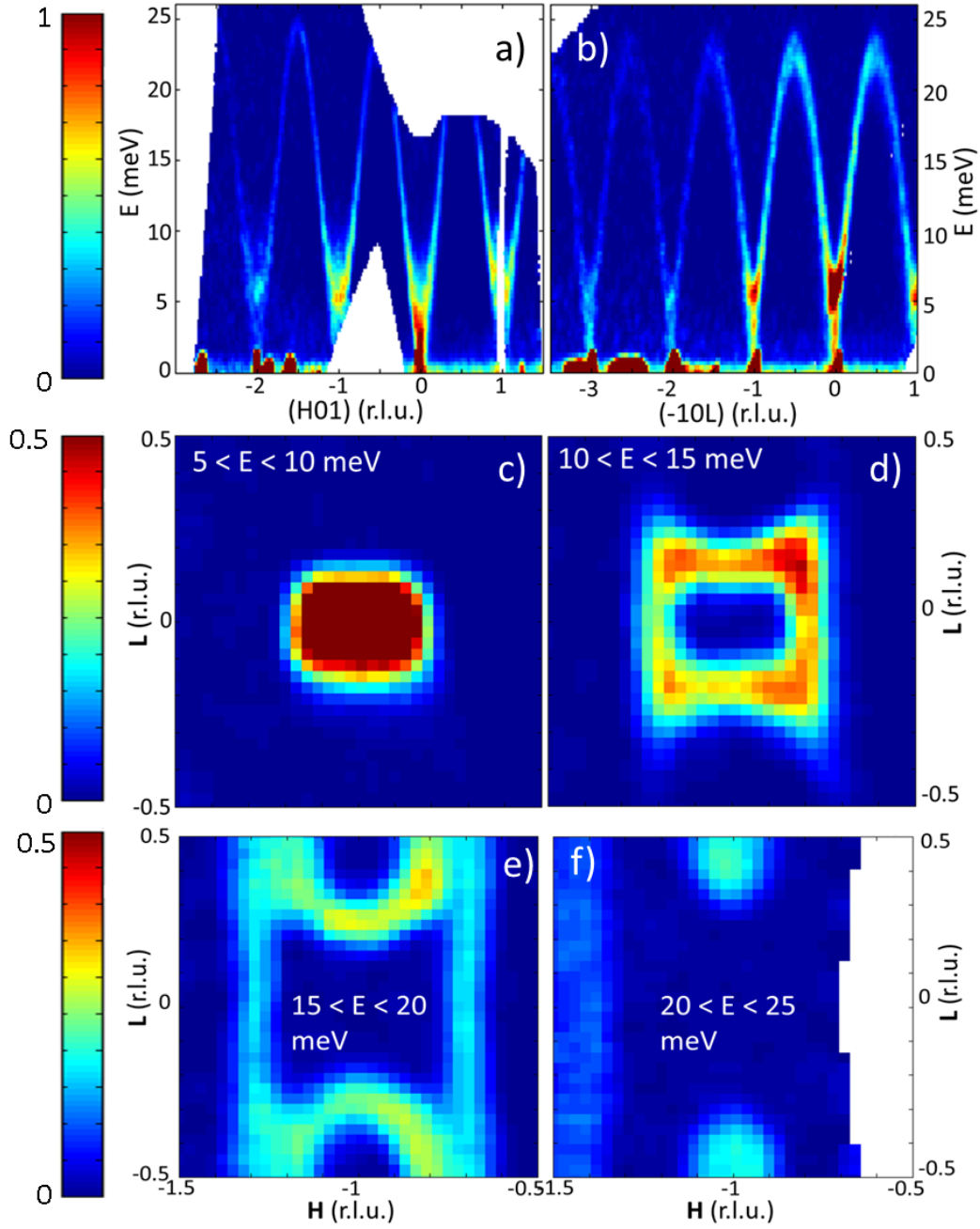
Figure 5.3: Contour plots of inelastic neutron scattering intensity at T = 5 K. Scale bars are shown on the left. Scattered neutron intensity as a function of energy E along the (a) **H** direction, (b) **L** direction. Scattered neutron intensity as a function of **H** and **L** for (c) 5 < E < 10 meV, (d) 10< E < 15 meV, (e) 15 < E < 20 meV, (f) 20 < E < 25 meV

is [122]

$$\omega(\boldsymbol{Q}) = 2S\sqrt{(J(0) - J'(0) + J'(\boldsymbol{Q}) + h_A)^2 - |J(\boldsymbol{Q})|^2}$$

Here, S is the total spin on an atom and h_A is a reduced anisotropy field. The exchange term J (Q) describes interactions betweens spins on opposite sublattices and J'(Q) describes interactions between spins on the same sublattice. We include first neighbor exchange interactions J_1 for spins that are on opposite sublattices, second neighbor interactions J_2 for spins that are on the same sublattice, and exchange interactions between nearest neighbors in different honeycomb layers J_c for spins that are on opposite sublattices (Figure 5.2). The interaction term $J'(\mathbf{Q}) = \sum_{\mathbf{n.n.n.}} J_2 e^{i\mathbf{Q}\cdot\mathbf{r}_{n.n.n.}}$, where the sum is over the 6 second neighbor atoms. The term $J(\mathbf{Q}) = \sum_{\mathbf{n.n.}} J_1 e^{i\mathbf{Q}\cdot\mathbf{r}_{n.n.}} + \sum_{\mathbf{c}} J_c e^{i\mathbf{Q}\cdot\mathbf{r}_c}$. The resulting spin wave dispersions along the H and L directions are

$$\omega(h) = 2S\sqrt{(\Delta + 4J_2\cos(2\pi h) + 3J_1 - 4J_2 + 3J_c)^2 - (4\cos(2\pi h) + 5)(J_1 + J_c)^2}$$

$$\omega(l) = 2S\sqrt{\Delta^2 + 6\Delta(J_1 + J_c) - 18J_1 J_c\cos(2\pi l) + 18J_1 J_c}$$

In Figure 5.4a,b we present H-cuts and L-cuts of the data presented in figure 5.3 at different energies. We approximate the resolution limited peaks by a Gaussian profile and our subsequent fitting of the observed scattering allows us to extract the spin wave dispersion along the **H** and **L** directions, and to characterize the magnetic exchange interactions in $CaMn_2Sb_2$. The scattered neutron intensity S(**Q**,E) for different energy transfers along the **H** direction is shown in Figure 5.4a. For summed energy transfers 6 meV $\leq$ E $\leq$ 8 meV, S(**Q**,E) is well fitted by the sum of two Gaussian functions, shifted from the magnetic Bragg peak. At larger energy transfers the peak positions of the fits move further from the Bragg peak, just as expected for dispersing spin wave excitations. For E > 24 meV we no longer observe scattering from the spin waves. Figure 5.4b presents S(**Q**,E) along the **L** direction, where we again observe dispersive spin wave excitations. Fits along **H** and **L**, centered at the average spin momenta $\pm\Delta\mathbf{Q}$(E), were performed every 2 meV . This fitting yields the spin wave momenta for different energy transfers, and the resulting spin wave dispersions, E($\Delta\mathbf{H}$) and E($\Delta\mathbf{L}$), are presented in Figures 5.4c,d.

The Mn spins in $CaMn_2Sb_2$ are in the ab-plane and so there should be two magnon branches. The first branch corresponds to spin deviations in ab-plane with a tiny gap set by a small in-plane hexagonal anisotropy. If one neglects this anisotropy, the resulting continuous symmetry with respect to spin rotations around c gives rise to a gapless Goldstone mode. The second
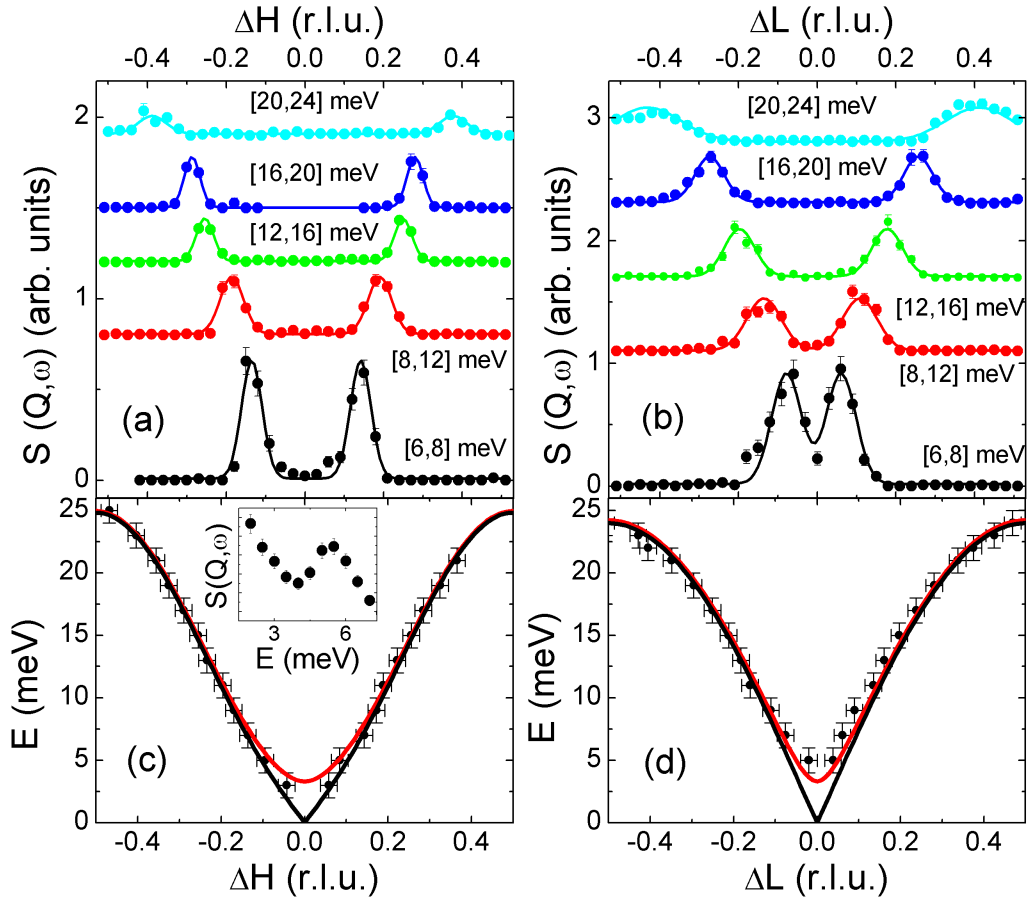
Figure 5.4: Scattered neutron intensity S($\mathbf{Q}$,E) along the $\mathbf{H}$ and $\mathbf{L}$ directions for ranges of energy transfers, as indicated. Scans are displaced for clarity. The solid lines are fits to the measured data as described in the text. (c,d) Black points represent the spin wave momenta and energies along $\mathbf{H}$ and $\mathbf{L}$ extracted from fits. Solid lines are fits to the observed dispersion with that expected from a Heisenberg spin model, as described in the text. The black line is the gapless acoustic mode and the red line is the optical mode, as described in the text.

branch corresponds to spin deviations out of plane with a larger gap. Both of these branches are seen in Figure 5.3a,b: the bottom of the gapped branch is seen as an intense spot, and another branch clearly goes to lower energies below this spot. As the q-resolution of our data is not sufficient to resolve the dispersion of the two branches individually we determined the magnitude of the spin gap by taking a constant Q-cut as shown in the inset to Figure 5.4c. We determine a spin gap of ≈ 4.5 meV.

The theoretical expressions for the spin wave dispersion for a J_1-J_2-J_c Heisenberg model were fit simultaneously to the measured dispersions along the **H** and **L** directions. Fits were performed for a gapless acoustic mode ($h_A = 0$) and a gapped optical mode and are shown respectively as black and red solid lines in Figure 5.4c,d. Excellent agreement is found between the Heisenberg model and the observed excitations. We find that $SJ_1 = 7.9 \pm 0.6$ meV and $SJ_2 = 1.3 \pm 0.2$ meV are both positive with $J_2/J_1 = 0.165$, signalling that the in-plane interactions are antiferromagnetic. The value of the ratio $J_2/J_1 = 0.165$ remains robust independent of the details of the microscopic model, that is whether or not the corrugation of the honeycomb planes or multiple anisotropy terms are included. The exchange interaction betwen nearest neighbors in different honeycomb layers $SJ_c = 0.51 \pm 0.05$ meV.

5.4 Discussion

In Figure 5.5 we use the ratio of the experimentally determined exchange interactions to situate $CaMn_2Sb_2$ on the phase diagram of the classical J_1-J_2-J_3 Heisenberg model [92] for a honeycomb lattice of spins, which is controlled by the ratios J_2/J_1 and J_3/J_1. We found that including a third neighbor exchange J_3 in our modelling of the spin wave excitations in $CaMn_2Sb_2$ did not significantly improve the quality of our fits and therefore take $J_3 = 0$. The phase diagram was constructed by calculating the ground state energies within the mean field approximation for different relative values of the exchange interactions [92]. Depending on the relative strengths of these interactions different types of antiferromagnetic ordering are expected, as indicated. Using the values of the exchange interactions determined from our inelastic neutron scattering measurements, we find that $CaMn_2Sb_2$ lies in the Néel ordered region of the phase diagram, in agreement with the magnetic structure determined from powder neutron diffraction measurements [118, 119]. Further, $CaMn_2Sb_2$ is found to be very close to the tricritical point where Néel order and two spiral antiferromagnetic configurations are predicted to co-exist. This large degeneracy of possible ground states, as well as presumed strong fluctuations among these states, is likely responsible for the relatively low ordering temperature

of $CaMn_2Sb_2$, $T_N = 85$ K [23, 31], which is much reduced from the mean field ordering temperature $T_{MFT} = (S+1)(3SJ_1+6SJ_2+2SJ_c)/3k_B = 310$ K for S=3/2 or 370K for S= 2. The close proximity of $CaMn_2Sb_2$ to the tri-critical point reported here confirms a recent prediction by Mazin [116], who speculates that the weak ferromagnetic component found in the intermediate temperature range could result from this proximity.
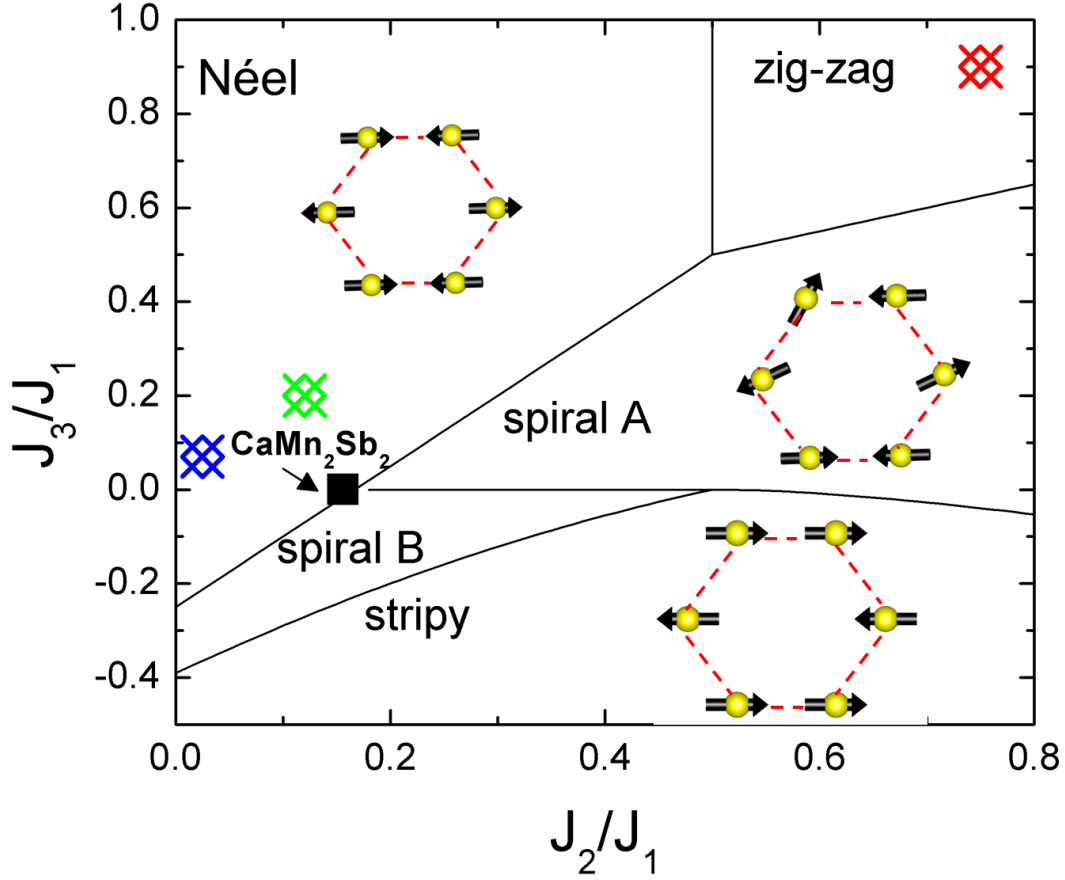
Figure 5.5: Phase diagram of the Heisenberg model for a honeycomb lattice with first, second and third neighbor exchange interactions J_1, J_2, and J_3 respectively [92]. Solid lines are phase boundaries for the different antiferromagnetic configurations indicated. The blue, green and red symbols represent $MnTiO_3$, $Bi_3Mn_4O_{12}$ and Na_2IrO_3 respectively. Filled black square is $CaMn_2Sb_2$

Until now, there has been a dearth of antiferromagnetic honeycomb lattice compounds whose exchange interactions have been determined experimentally, so as to facilitate comparison with the phase diagram in Figure

5.5. The exchange interactions determined from a single crystal inelastic neutron scattering study of $MnTiO_3$ and $BaNi_2(PO_4)_2$ place them deep in the Néel phase [101, 102], in agreement with the determined magnetic structure [100, 101]. Bounds on the exchange interactions of the effective spin 1/2 honeycomb lattice compound Na_2IrO_3 place it solidly in the zigzag antiferromagnetic phase. While this is in agreement with the experimentally determined magnetic structure, a Kitaev exchange term is important to characterize the strong magnetic frustration in this compound, and the strong spin-orbit coupling may displace this compound from the indicated position [114, 115]. Inelastic neutron scattering measurements have also been reported on the honeycomb lattice compound $Bi_3Mn_4O_{12}$ and, using the resulting bounds on exchange interactions, this compound is also situated in the Néel antiferromagnetic phase of Figure 5.5. However, long range magnetic order in $Bi_3Mn_4O_{12}$ has not been observed down to 0.4 K, indicating interlayer exchange interactions are likely necessary to understand its magnetic properties [111]. Thus, our experiments are the first to show that $CaMn_2Sb_2$ is an antiferromagnetic honeycomb lattice compound situated in close proximity to a multicritical point on the phase diagram of the Heisenberg model for a honeycomb lattice. This proximity enhances the magnetic frustration and further reduces the ordering temperature in $CaMn_2Sb_2$ from the expected mean field ordering temperature. It would be interesting to study a structurally similar compound with stronger quantum fluctuations, e.g. by replacing the large Mn moments with lower spin moments, to determine if the long range magnetic order could be completely suppressed, leading to a spin liquid state.

Chapter 6

LaMn$_x$Sb$_2$

We have synthesized large single crystals of LaMn$_x$Sb$_2$ and confirmed that it crystallizes in the ZrCuSiAs structure. Electrical resistivity measurements as a function of temperature $\rho(T)$ display metallic behavior that is confirmed by the large Sommerfeld coefficient, determined by our low temperature specific heat $C(T)$ measurements. Both $\rho(T)$ and $C(T)$ display anomalies at $T = 130$ K. To determine its origin we performed neutron diffraction measurements that show LaMn$_x$Sb$_2$ exhibits long range antiferromagnetic order below $T_N = 130$ K. We use irreducible representational analysis to model the neutron diffraction data, determining a canted antiferromagnetic structure and an ordered moment of 2.9 μ_B/Mn. The presence of a large ordered moment and Sommerfeld coefficient in this correlated metallic system suggests LaMn$_x$Sb$_2$ may be in an orbitally selective Mott phase. We then present DFT+DMFT calculations that find the d_{xy} electrons remain localized in the metallic state, in contrast to DFT calculations that find a d_{xy} band that crosses the Fermi level. These results are consistent with a strong Hund's effect that decouples the manganese orbitals leading to an orbitally selective Mott phase in LaMn$_x$Sb$_2$.

6.1   Introduction

In Chapters 3 and 4 of this thesis we showed that strong electronic correlations due to a large Hubbard U and Hund's coupling J$_H$ are responsible for the formation of an insulating state in LaMnPO and BaMn$_2$As$_2$, which are isostructural with the parent compounds of the Fe-based superconductors. There has been a large effort to metallize and suppress the magnetic moment in these systems via chemical doping, with the hope of realizing superconductivity that has not yet been observed in square-net Mn compounds. While there has been some success in reducing the gap size and even metallizing

Arsenic bands, the Mn moments have remained largely localized [43, 52, 84]. In contrast, pressurized LaMnPO becomes metallic at 16 GPa, with magnetic susceptibility measurements suggesting it remains magnetic until 34 GPa at which point the long range magnetic order vanishes [54] (see Figure 6.1). These findings are supported by electronic structure calculations [43](see Figure 6.1). Unfortunately, there has so far been no spectroscopic evidence from neutron scattering or photoemission for the nature of the antiferromagnetic metallic state in pressurized LaMnPO or $BaMn_2As_2$, due to the inherent difficulty in performing these measurements under pressure. It has been proposed that the correlation effects due to a strong Hund's coupling that lifts the band degeneracy [9, 11] may be responsible for the separation of the charge and moment delocalization transitions in Mn pnictide systems [23, 43]. In this picture, charge delocalization takes place when one of the Mn orbitals becomes delocalized, while the other orbitals remain localized. Thus, we are left with an antiferromagnetic metallic state with a significant local moment. Such an orbitally selective Mott phase, arising in the presence of strong Hund's coupling (see Figure 1.3), has been reported in the iron chalcogenide superconductors $A_xFe_{2-y}Se_2$ [123], which are generally considered as the most correlated iron-based superconductors as indicated by their large ordered moment of 3.3 μ_B/Fe, comparable to the ordered moment of 3.2 μ_B/Mn in LaMnPO.

Here we report the first physical property measurements of the Mn pnictide compound $LaMn_xSb_2$ [32], isostructural to LaMnPO and the iron-based superconductors. Intriguingly, our electrical resistivity measurements performed on single crystals of $LaMn_xSb_2$ display metallic behavior, in contrast to its isostructural counterparts. Specific heat measurements confirm a density of states at the Fermi level, with a rather large Sommerfeld coefficient suggesting strong electronic correlations associated with Mn. High temperature magnetic susceptibility measurements reveal a large fluctuating moment of 4.2 μ_B/Mn. Both resistivity and specific heat measurements display an anomaly at T = 130 K. To investigate whether this anomaly is associated with long range antiferromagnetic ordering we performed neutron diffraction measurements. These measurements revealed a canted antiferromagnetic state below T_N = 130 K with an ordered magnetic moment of 2.9 μ_B/Mn at T = 5 K.

These experimental observations of a strongly correlated metallic state with a significant ordered moment of 2.9 μ_B/Mn, rather strongly reduced from the full Hund's value of 5 μ_B/Mn, are suggestive of the co-existence of local moment and itinerant Mn states. To investigate whether this is the case, our colleagues Dr. Yin and Prof. Kotliar at Rutgers performed DFT+DMFT calculations. For the same values of Hubbard U = 8 eV and Hund's coupling J_H = 0.9 eV used for LaMnPO and $BaMn_2As_2$, these calculations reveal a

metallic state in LaMn$_x$Sb$_2$. Further, these calculations find that the d$_{xy}$ orbital, in the presence of a large U and J$_H$, remains localized in the metallic state, but contributes to the Fermi surface in DFT calculations that do not include strong correlations. Taken together, our experimental and theoretical results suggest that LaMn$_x$Sb$_2$ may be in an orbitally selective Mott phase (OSMP), due to the orbital decoupling imposed by a strong Hund's coupling.
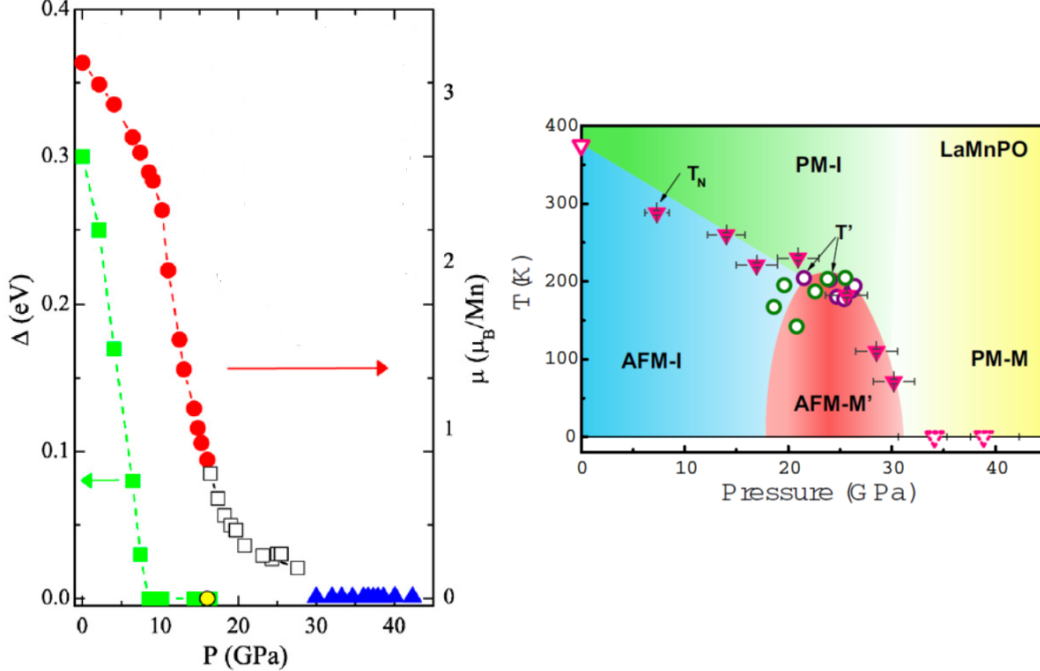
Figure 6.1: (left) Local spin density approximation (LSDA) calculations of LaMnPO: the charge gap (green squares), and the ordered magnetic moment in tetragonal (red circles), orthorhombic (open squares) and collapsed orthorhombic (blue squares) [43]. A DMFT calculation of the gap is shown as a yellow circle. (right) Temperature-pressure phase diagram of LaMnPO constructed from electrical resistivity and magnetic susceptibility measurements [54]. An antiferromagnetic insulating (AFM-I) phase gives way to an antiferromagnetic metallic phase (AFM-M) that eventually results in a paramagnetic metallic phase (PM-M) at higher pressures.

6.2 Experimental Details

Single crystals of LaMn$_x$Sb$_2$ were prepared from a Mn-Sb flux as described in chapter 2. The previously reported tetragonal crystal structure of LaMn$_x$Sb$_2$

(P4/nmm, No. 129) with a = b = 4.3864(4) Å and c = 10.799(1) Å was confirmed by single crystal x-ray diffraction at room temperature [32]. Electrical resistance measurements were performed with a 5 mA current flowing in the ab plane using a Quantum Design Physical Properties Measurement System. Heat capacity measurements were performed on a 5.2 mg single crystal using a Quantum Design Physical Properties Measurement System. Temperature dependent magnetic susceptibility measurements were performed with a 1 T field applied in the ab plane of a 30 mg single crystal using the Vibrating Sample Magnetometer option on a Quantum Design Physical Properties Measurement System. Neutron diffraction measurements were performed at the BT1 instrument at NCNR at NIST on a 6 g powder of crushed single crystals for temperatures T = 5 K - 650 K with an incident wavelength of 2.078 Å using Ge(311) monochromator, that provides the highest intensity on this instrument. Pair distribution function measurements were performed by measuring the total scattering powder diffraction on beam-line X17A at the National Synchrotron Light Source at Brookhaven National Laboratory. Data were collected in rapid acquisition mode with an x-ray energy of 67.419keV (=0.1839 Å) on a Perkin-Elmer 2D flat panel detector (2048×2048 pixels and 200×200 μm pixel size) mounted orthogonal to the beam path. The sample to detector distance was approximately 206 mm for the experiments and was calibrated using a nickel standard with the FIT2D program. A bulk powder of $LaMn_xSb_2$ was packed into a Kapton capillary and measured at 100K. The raw 2D intensity was corrected for experimental effects and azimuthally integrated and converted to 1D intensity versus Q plots using FIT2D. PDFgetX3 was used to correct and normalize the diffraction data to obtain F(Q) and Fourier transform them to obtain the PDF, G(r).

6.3   Experimental Results and Analysis

A room temperature single crystal x-ray diffraction measurement was performed on a carefully selected small ($\approx$ 100 μm) single crystal of $LaMn_xSb_2$. While single crystal diffraction has previously been reported on $LaMn_xSb_2$ [124], our results have significantly improved on the accuracy of this previous report. In addition we wished to investigate more closely whether a super-structure exists, as the reported structural unit $LaMn_xSb_2$ has only partial site occupancy on the Mn site. We assumed a triclinic unit cell and developed a strategy using the Bruker APEX II software to determine the stucture of $LaMn_xSb_2$. 1650 Bragg reflections were collected and 1466 of these were unique reflections, far more than in the previous report where only 314 unique reflections were sampled [124]. The Jana software was then used to de-

termine the space group that best satisfies the observed absorption-corrected reflections. The previously reported P4/nmm is determined to provide the best fit. Over the range of Q-space covered by our measurement we find that of the 41 reflections that should be extinct within this space group only 6 have intensities $I/\sigma(I) > 3$. These reflections are displayed in Table 6.1.

h	k	l	I	σ(I)	I/σ(I)	empirical formula	$LaMn_{0.71}Sb_2$
4	-3	0	197.4	30.3	6.5	fw	421.24
3	-2	0	127.9	20.7	6.2	temperature (K)	299(2)
						λ (Å)	0.71073
1	4	0	205.7	45.7	4.5	space group, Z	P4/nmm (no. 129), 2
-3	2	0	126.6	28.9	4.4	a (Å)	4.3783(6)
						c (Å)	10.8033(15)
2	3	0	86.8	27.6	3.1	V (Å³)	207.09(5)
-3	4	0	100.8	32.6	3.1	ρ_{calc}(g/cm³)	6.7552
						goodness-of-fit	2.18
						R [I > 3σ(I)]	0.0319
						wR [I > 3σ(I)]	0.0454

Table 6.1: (left) Forbidden reflections of P4/nmm that were observed with $I/\sigma(I) > 3$. (right) Crystallographic and refinement parameters from x-ray diffraction measurements of a single crystal.

Next, we use the Superflip charge-flipping algorithm to solve for the electronic distribution within the unit cell. We start with the initial composition $LaMn_xSb_2$ with composition determined from our EDX measurements x = 0.74 ± 0.04, where we found that the value of x can vary somewhat between crystals as previously pointed out [32]. The program repeatedly and rapidly converges to the crystal structure presented in Figure 6.2. The refinement data and crystallographic parameters are presented in Table 6.1. Figure 6.2 compares the crystal structure of the compound LaMnPO discussed in detail in Chapter 3 of this thesis with $LaMn_xSb_2$. The size of the unit cell of $LaMn_xSb_2$ is significantly larger, in particular the distance between Mn planes has increased by 2 Å. Therefore the MnSb layers are more well separated than the MnP layers in LaMnPO suggesting $LaMn_xSb_2$ is more two-dimensional. However, while the LaO layer in LaMnPO can be viewed as a charge reservoir layer, this is likely not the case for the LaSb layer in $LaMn_xSb_2$. This is reflected in the structure presented in Figure 6.2 which shows the bonding to indicate that La is nearly equidistant from both Sb sites. It is likely that this increase in the size of the cell and the height of La may be attributed to the larger size and lower electronegativity of Sb compared to O/P. We also point out that,

while $La^{+3}Mn^{+2}P^{-3}O^{-2}$ is nominally charge balanced, $La^{+3}Mn^{x\times(+2)}Sb^{2\times(-3)}$ is not.
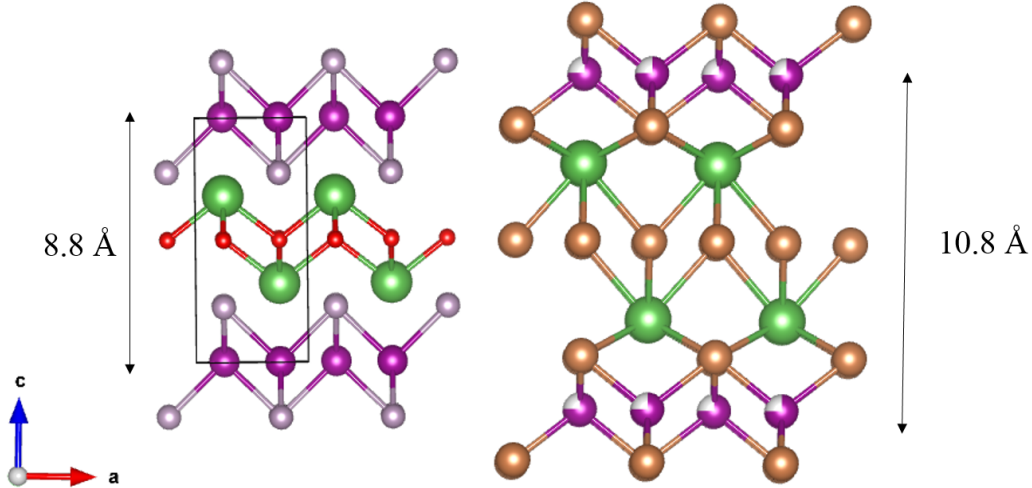
Figure 6.2: (left) LaMnPO crystal structure a = 4.054 Å, c = 8.8 Å. (right) $LaMn_xSb_2$ crystal structure a = 4.39 Å, c = 10.8 Å.

We now present room temperature powder neutron diffraction and pair distribution function measurements at 100 K that are both well described by the nuclear structure determined from our single crystal x-ray diffraction analysis. Total scattered neutron intensity as a function of angle is presented in Figure 6.3a. These measurements were performed at the high-resolution BT1 instrument at NIST using the Ge(311) monochromator (λ = 2.078 Å). The best fit of this diffraction pattern to the pattern expected from our single crystal structure is presented as a black line. Good agreement with the single crystal structure is found as indicated by the low R and χ^2 values shown in Figure 6.3a. Our refinement finds best agreement for Mn site occupancy x = 0.77, larger than the single crystal value of 0.71 but consistent with our EDX observations that there is a distribution of possible site occupancies as previously reported [32]. Figure 6.3b presents pair distribution function (PDF) measurements that were performed on a powder sample of $LaMn_xSb_2$ that we provided to Prof. Billinge and his graduate student Soham Banerjee. PDF measurements can be sensitive to local structural order, such as local dimer formation, as well as the formation of superstructures that may not be detectable by conventional single crystal x-ray diffraction [125]. For $LaMn_xSb_2$ the PDF is well described by the average crystal structure from our single crystal x-ray diffraction measurements over a large range of distances 1.5 Å - 50 Å, as indicated by a low R value = 0.073. Overall, our determinations of

the long range and short range nuclear structure of LaMn$_x$Sb$_2$ indicate that the occupancy of the Mn site is fully random.

Figure 6.3: (a) Room temperature neutron diffraction on a powder sample of LaMn$_x$Sb$_2$ with incident wavelength of 2.078 Å. (b) Pair distribution function measurements of LaMn$_x$Sb$_2$ at 100 K.

Previously, only the crystal structure of LaMn$_x$Sb$_2$ was reported. In Fig-

ure 6.4 we present the basic physical properties of single crystals of $LaMn_xSb_2$. Electrical resistivity as a function of temperature $\rho(T)$ (Figure 6.4a) increases as the temperature T increases, consistent with metallic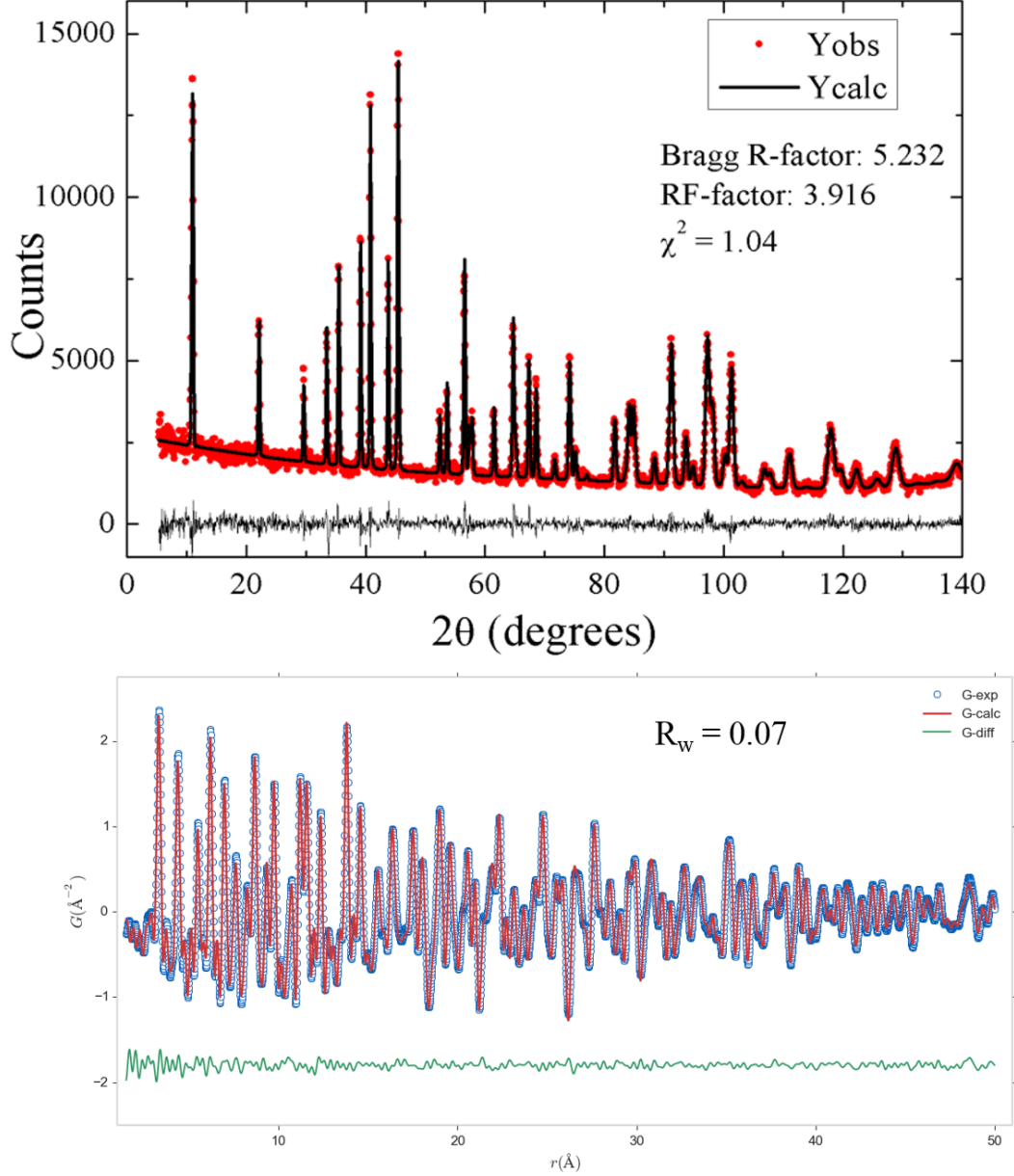 behavior. The temperature derivative $d\rho(T)/dT$ is presented in the inset of Figure 6.4a and displays a clear minimum at T $\approx$ 130 K. We find Fermi liquid behavior, $\rho = \rho(T=0) + A\ T^2$ at low temperatures in $LaMn_{0.7}Sb_2$ with A = 6.1×10^{-3} $\mu\Omega$ cm K^{-2} (Figure 6.4b). These measurements were repeated on three different single crystals of $LaMn_xSb_2$ with similar results, indicating that the metallic character of $LaMn_xSb_2$ is intrinsic, and is not associated with inclusions of the MnSb contaminant phase.

Specific heat as a function of temperature C(T) is presented in Figure 6.4c. Of particular note is an anomaly that is observed at 130 K (inset of Figure 6.4c), the same temperature where $d\rho(T)/dT$ displays a local minimum. The low temperature specific heat has both electronic and phonon contributions $C/T = \gamma + \beta T^2$. Figure 6.4d presents a linear fit to C/T as a function of T^2. The slope of this linear fit corresponds to β while the y-axis intercept corresponds to the Sommerfeld coefficient γ. We find a rather large $\gamma = 19.2$ mJ/f.u. mol K^2 suggestive of strong correlations and a large density of states at the Fermi level. The low temperature phonon contribution $\beta = 12\ \pi^4$ r R/(5 $T_D{}^3$) where r is the number of atoms and R is the gas constant yields a Debye temperature T_D = 277 K. However, this Debye temperature drastically underestimates the intermediate temperature phonon contribution. Accordingly, we used the full Debye expression C = 9 r R $(T/T_D)^3$ $\int_0^{T_D/T}$ x^{4}e^x/(e^x - 1)^2 where x = T/T_D to more accurately model the data. This modelling yielded a Debye temperature T_D = 217 K, which can rather accurately account for the phonon contribution to the experimental C(T) over the full temperature range as shown in Figure 6.4b. Figure 6.4e presents the magnetization M of a single crystal of $LaMn_xSb_2$, obtained over wide temperature and field ranges. As described in Chapter 2 of this thesis, these measurements are likely to be affected by ferromagnetic MnSb contaminants. However, above the ordering temperature of MnSb ($T_c \approx$ 600 K) the moments associated with $LaMn_xSb_2$ should dominate. Figure 6.4f presents the inverse high temperature susceptibility of a single crystal of $LaMn_xSb_2$ that reveals Curie-Weiss like behavior with an effective moment μ_{eff} = 4.2 μ_B/Mn, indicating the presence of large local moments with spin between S = 3/2 (μ_{eff} = 3.87 μ_B/Mn) and S = 2 (μ_{eff} = 4.9 μ_B/Mn). This fit also revealed a large negative Weiss temperature of θ_W = 307 K that indicates the presence of strong antiferromagnetic interactions between local magnetic moments.

We now present neutron diffraction measurements obtained at 6 K on a powder sample of $LaMn_xSb_2$ that reveal the presence of long range antiferro-
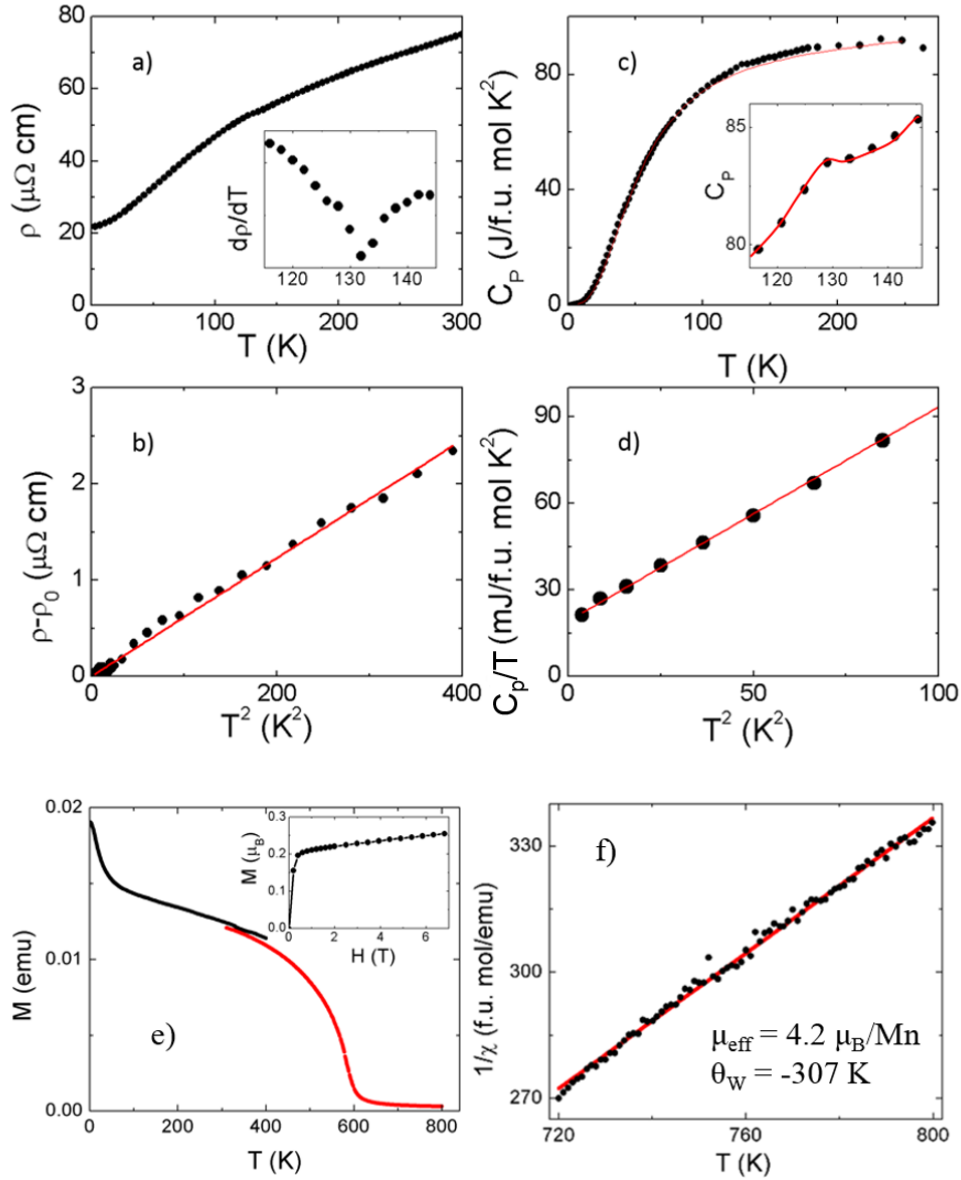
Figure 6.4: Measurements on single crystals of LaMn$_x$Sb$_2$ (a) Electrical resistivity as a function of temperature ρ(T) (b) Low temperature fit to Fermi-liquid model (c) Specific heat as a function of temperature. Solid line is fit to the Debye model plus low temperature electronic contribution. (inset 1) closer look at the anomaly at 130 K (d) Electronic and phonon fit to the low temperature specific heat. (e) Magnetic susceptibility as a function of temperature (inset) magnetization as a function of field H (f) Inverse magnetic susceptibility as a function of temperature with Curie-Weiss fit

91

magnetic order below T_N = 130 K (Figure 6.5). The inset of this figure is a comparison of the 6 K and 300 K neutron diffraction patterns at low angles. It is clear that at low temperature we have new peaks (marked with black dots) that do not correspond to the nuclear structure at 300 K, as well as enhanced intensity at select nuclear peaks. The intensity of these peaks decreases as the angle increases, consistent with the magnetic form factor for Mn (see Figure 3.4). We therefore attribute these additional peaks to the formation of long range magnetic order. We define a wavevector $Q = \hat{a} \frac{2\pi}{a} h + \hat{b} \frac{2\pi}{a} k + \hat{c} \frac{2\pi}{c} l$. The additional peaks, as well as the peaks that have enhanced intensity, may be conveniently indexed in terms of the wavevector $Q = (1\ 0\ \frac{l}{2})$ where l is a positive integer.
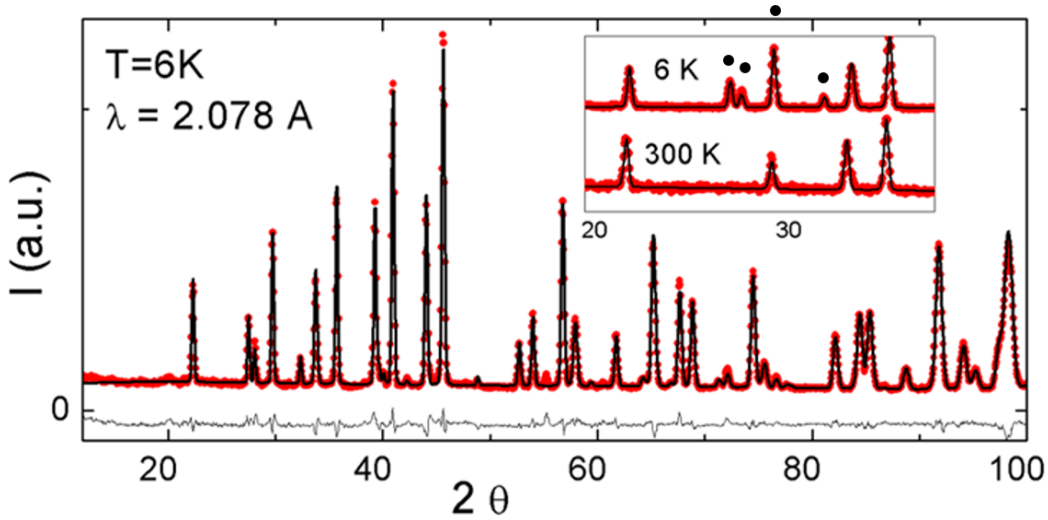
Figure 6.5: Neutron diffraction of powder of LaMn$_x$Sb$_2$ (red dots) with refinement as described in the text (black line). The inset compares the low angle diffraction pattern at T = 6 K and T = 300 K. The black dots indicate peaks that are wholly are partially due to the onset of long range antiferromagnetic order.

We now analyze our T = 6 K neutron diffraction data using magnetic representational theory to determine the magnetic structure and ordered magnetic moment. Before one proceeds with representation analysis, it is necessary to first find the "k-vector" $\boldsymbol{k}$ that determines how moments transform when translating between unit cells $\psi_j = \psi_i \exp(i\ \boldsymbol{k}\ \boldsymbol{t}_{ij})$ where i,j are different unit cells, and t$_{ij}$ is a lattice vector. Within the FullProf suite [126] there is a ksearch tool that allows the user to determine the $\boldsymbol{k}$ for the magnetic diffraction pattern. The input for this search tool is the crystallographic space group as well as the diffraction angles and intensities of the magnetic diffraction peaks. We

find that no single commensurate $\boldsymbol{k}$ can account for the magnetic diffraction pattern of LaMn$_x$Sb$_2$. An incommensurate magnetic structure means that at least one component of $\boldsymbol{k}$ is an irrational number. We find best agreement when all three components of $\boldsymbol{k}$ are irrational. While magnetic structures with incommensurate k-vectors are rather common and can indicate spin density wave magnetism, for example in chromium metal or 1D organic salts [127], we do not consider this possibility here due to the large local moments revealed by the Curie-Weiss behavior in Figure 6.4.

As described earlier the observed magnetic diffraction peaks from our neutron diffraction measurements of LaMn$_x$Sb$_2$ may be indexed as $(1\ 0\ \frac{l}{2})$. From a survey of the literature, we find that there are two common types of antiferromagnetic order in manganese pnictide compounds that adopt the same ZrCuSiAs structure as LaMn$_x$Sb$_2$. Figure 6.6a presents a measured neutron diffraction measurement of LaMnPO at different temperatures [43, 53]. In the antiferromagnetically ordered state below 375 K, additional magnetic diffraction peaks appear that can be indexed as $(1\ 0\ L)$. The authors then determined a $\boldsymbol{k_1} = (0\ 0\ 0)$ and the magnetic structure shown in Figure 6.6c that consists of collinear antiferromagnetic planes stacked ferromagnetically. Figure 6.6b presents the results of a neutron diffraction measurement of BaMnAsF in the antiferromagnetically ordered state [128]. Additional magnetic diffraction peaks are present that can be indexed as $(1\ 0\ \frac{2l+1}{2})$. The authors then determined a $\boldsymbol{k_2} = (0\ 0\ 1/2)$ and the magnetic structure shown in Figure 6.6d that consists of collinear antiferromagnetic planes stacked antiferromagnetically. We realized that by considering two propagation vectors $\boldsymbol{k_1}$ and $\boldsymbol{k_2}$, we could index the magnetic diffraction diffraction peaks observed in LaMn$_x$Sb$_2$. The same conclusion may be reached using the k-vector search tool in the SARAh-Refine software [129, 130] that allows the user to search for multiple propagation vectors.

The irreducible representations that leave the space group elements invariant under $\boldsymbol{k}$ may be found using the Kovalev tables as tabulated in SARAh. The basis vectors of the irreducible representations of the magnetic space groups of P4/nmm with $\boldsymbol{k_1} = (0\ 0\ 0)$ and $\boldsymbol{k_2} = (0\ 0\ \frac{1}{2})$ are the same and are presented in Table 6.2. A detailed prescription of how an irreducible representation is decomposed into basis vectors is provided in the help files of the SARAh program. Using these two propagation vectors, there are now 16 possible combinations of irreducible representations. However, only four of these combinations, (k$_1$ → Γ_6, k$_2$ → Γ_6) or (k$_1$ → Γ_6, k$_2$ → Γ_{10}) or (k$_1$ → Γ_{10}, k$_2$ → Γ_6) or (k$_1$ → Γ_{10}, k$_2$ → Γ_{10}), produce the desired magnetic reflections at $(1\ 0\ \frac{l}{2})$ and therefore we only consider these. Two of these combinations yield ferrimagnetic solutions that we do not consider, because we have only one Mn
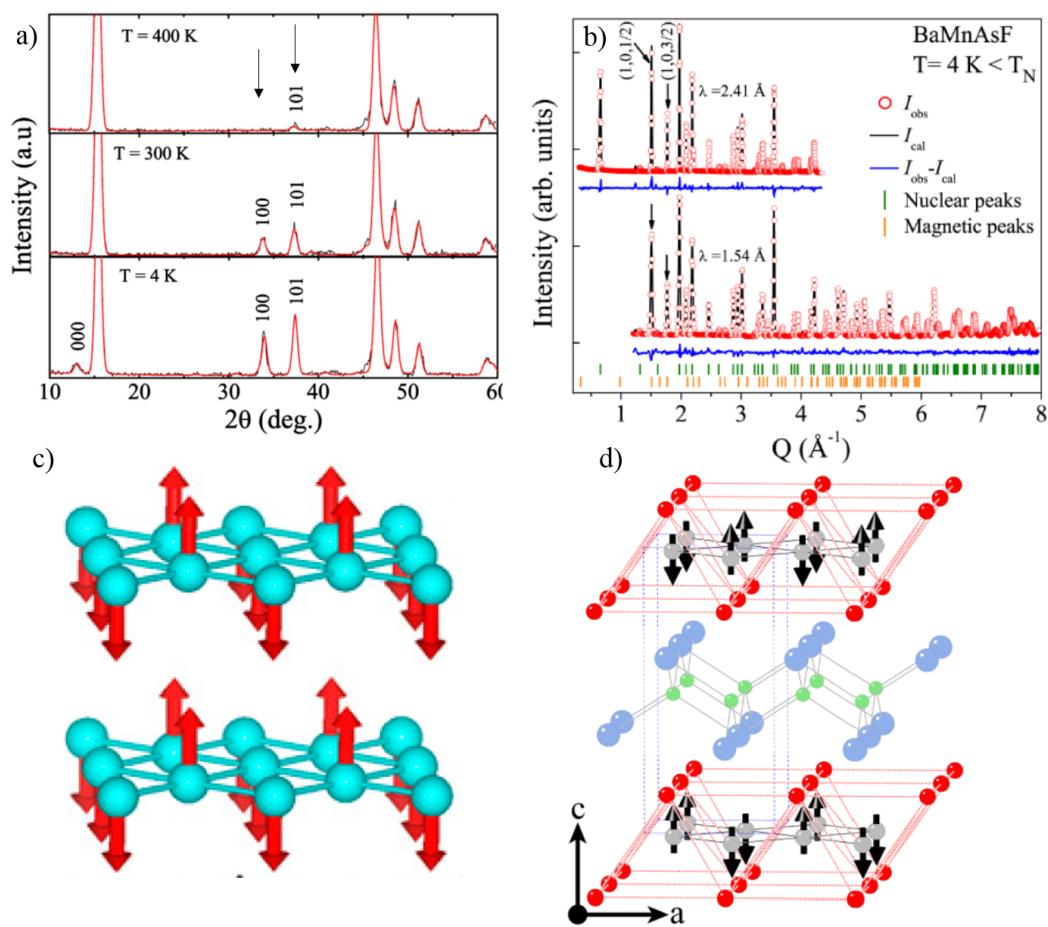
Figure 6.6: (a,c) Neutron diffraction pattern and refined magnetic structure of LaMnPO [43] (b,d) Neutron diffraction pattern and refined magnetic structure of BaMnAsF [128]

site symmetry. Thus all Mn ions have the same local environment and should have the same valence and moment via Hund's rules.

IR	BV	Atom	BV components					
			$m_{\|a}$	$m_{\|b}$	$m_{\|c}$	$im_{\|a}$	$im_{\|b}$	$im_{\|c}$
Γ_3	ψ_1	1	0	0	8	0	0	0
		2	0	0	8	0	0	0
Γ_6	ψ_2	1	0	0	8	0	0	0
		2	0	0	-8	0	0	0
Γ_9	ψ_3	1	4	0	0	0	0	0
		2	4	0	0	0	0	0
	ψ_4	1	0	-4	0	0	0	0
		2	0	-4	0	0	0	0
Γ_{10}	ψ_5	1	0	4	0	0	0	0
		2	0	-4	0	0	0	0
	ψ_6	1	-4	0	0	0	0	0
		2	4	0	0	0	0	0

Table 6.2: Basis vectors for the space group P 4/n m m:2 with $\mathbf{k} = (0, 0, 0)$ or $\mathbf{k} = (0, 0, 0.5)$. The decomposition of the magnetic representation for the Mn site (.75, .25, 0) is $\Gamma_{Mag} = 0\Gamma_1^1 + 0\Gamma_2^1 + 1\Gamma_3^1 + 0\Gamma_4^1 + 0\Gamma_5^1 + 1\Gamma_6^1 + 0\Gamma_7^1 + 0\Gamma_8^1 + 1\Gamma_9^2 + 1\Gamma_{10}^2$. The atoms of the nonprimitive basis are defined according to 1: (.75, .25, 0), 2: (.25, .75, 0).

Only two possible solutions remain and we present the fits of these solutions to our measured T = 6 K diffraction pattern in Figure 6.7. The ($k_1 \rightarrow \Gamma_6$, $k_2 \rightarrow \Gamma_{10}$) is a better fit with ($R_p$, R_{wp}) = (0.0488, 0.0634) for the combined magnetic and nuclear structure compared to (R_p, R_{wp}) = (0.054, 0.0721) for ($k_1 \rightarrow \Gamma_{10}$, $k_2 \rightarrow \Gamma_6$). The resulting magnetic structure of LaMn$_x$Sb$_2$ is presented in Figure 6.8. The magnetic unit cell is doubled with respect to the nuclear unit cell. The structure consists of collinear antiferromagnetic spins in the ab plane with the moment direction canted 36° from the c-axis. This plane is then repeated along the c-direction but with the moments pointing -36° from the c-axis in the repeated unit. Due to powder averaging the orientation of the moment in the ab plane may not be uniquely determined.

The overall picture that emerges from our experimental results presented above is that LaMn$_x$Sb$_2$ is a strongly correlated antiferromagnetic metal below T_N = 130 K. The presence of strong correlations inferred from a large electronic contribution to the specific heat suggests that bands with substantial Mn 3d character are present at the Fermi level. However, our neutron diffraction measurements reveal a rather large ordered magnetic moment of 2.9
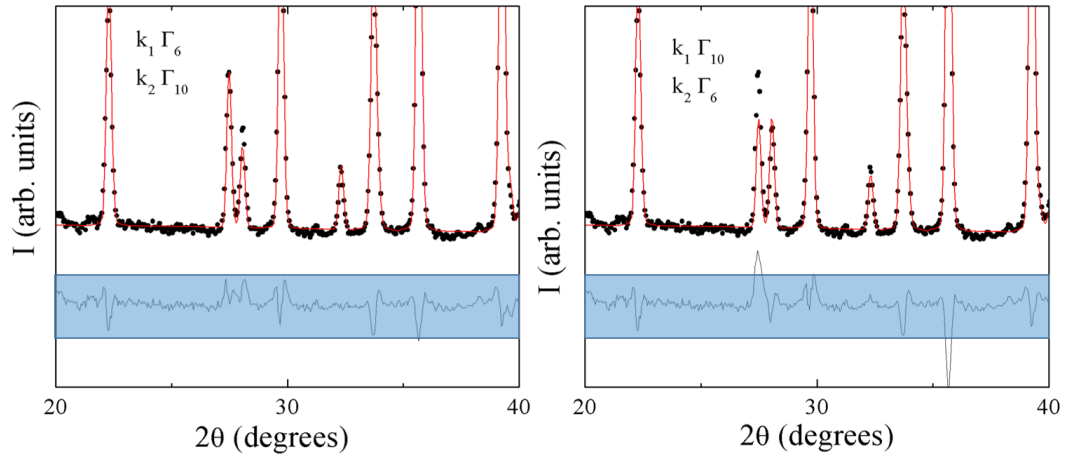
Figure 6.7: Neutron diffraction pattern of LaMn$_x$Sb$_2$ at T = 6 K with refined magnetic model for the propagation vectors k$_{1,2}$ and irreducible representation $\Gamma_{6,10}$ indicated.
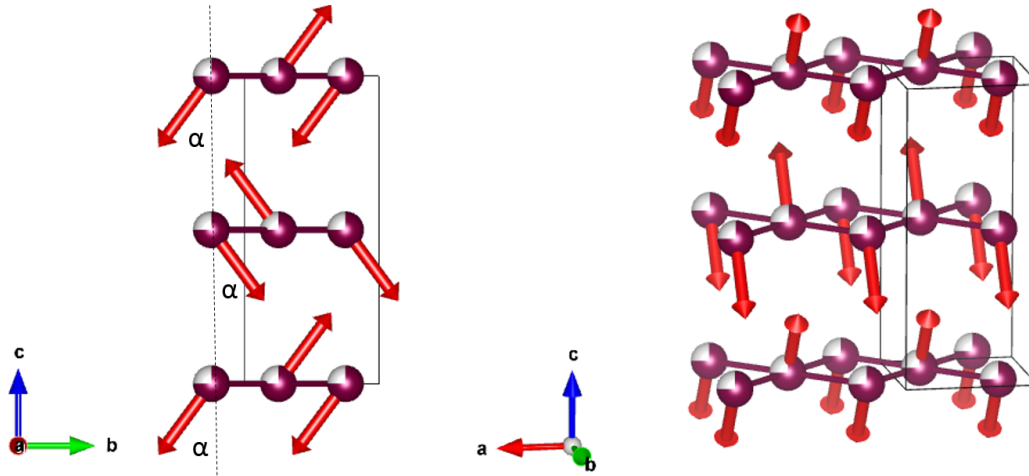
Figure 6.8: Two different projections of the magnetic structure of LaMn$_x$Sb$_2$ determined from irreducible representation analysis of neutron diffraction pattern. The angle α between the c-axis and direction of magnetic moment is α = 36°. The magnitude of the ordered magnetic moment is 2.9 μ_B/Mn.

μ_B/Mn, albeit one that is substantially reduced from the 5 μ_B/Mn expected from Hund's rules. Taken together, these observations suggest the coexistence of substantial localized Mn magnetic moments with itinerant bands of Mn character.

We now turn to electronic structure calculations performed by Dr. Zhiping Yin in the group of Prof. Kotliar to investigate further the electronic properties of LaMn$_x$Sb$_2$. Although these calculations are performed for stoichiometric LaMnSb$_2$, they appear to qualitatively capture the physics of LaMn$_x$Sb$_2$, as will now be discussed.

A DFT calculation of the electronic density of states of LaMnSb$_2$ along high symmetry directions in reciprocal space is presented in Figure 6.9a. It is clear that there are bands crossing the Fermi level and LaMnSb$_2$ is found to be metallic. The orbitally resolved density of states for the same calculation is presented in Figure 6.9c. The bands crossing the Fermi level are found to be predominantly associated with the t$_{2g}$ orbitals (d$_{xy}$ (green) d$_{xz,yz}$ (brown/red)), as would be expected for tetrahedrally co-ordinated Mn ions. While DFT correctly predicts metallic behavior in LaMn$_x$Sb$_2$, we emphasize that the experimental observation of strong correlations in this compound suggests that DFT may not be an appropriate method to describe material, as has been shown in structurally similar Mn pnictide compounds [23, 25]. Thus, we now present DFT+DMFT which can more accurately capture the physics of strongly correlated electron systems.

Figure 6.9b presents a DFT+DMFT calculation of the electronic density of states of LaMnSb$_2$ along high symmetry directions including a Hubbard U = 8 eV and Hund's J$_H$ = 0.9 eV, the same values used for isostructural LaMnPO and BaMn$_2$As$_2$ [23, 25]. Unlike LaMnSb$_2$, those two compounds are insulating. The band structure of LaMnSb$_2$ has clearly been severely modified compared to the DFT calculation, which does not properly account for electronic correlation effects. Figure 6.9d presents the orbitally resolved density of states for the same calculation shown in Figure 6.9b. Of particular note, the d$_{xy}$ band, which DFT predicted crosses the Fermi level, is now completely gapped out. This gapping out of the d$_{xy}$ band is likely a direct consequence of the strong Hund's coupling that tunes the correlations in different orbitals [9, 11]. The contribution of the different Mn 3d bands is presented more clearly in Figure 6.9e, that presents the k-space integrated partial density of states for the same calculation. It is clear that the d$_{xz,yz}$ electrons dominate at the Fermi level.

Figure 6.9f presents the partial density of states for different atoms obtained from the same calculation as Figure 6.9b. While the Mn 3d ions dominate, there is a significant contribution from electrons originating from Sb and La atoms. As would be expected, there is considerable hybridization be-
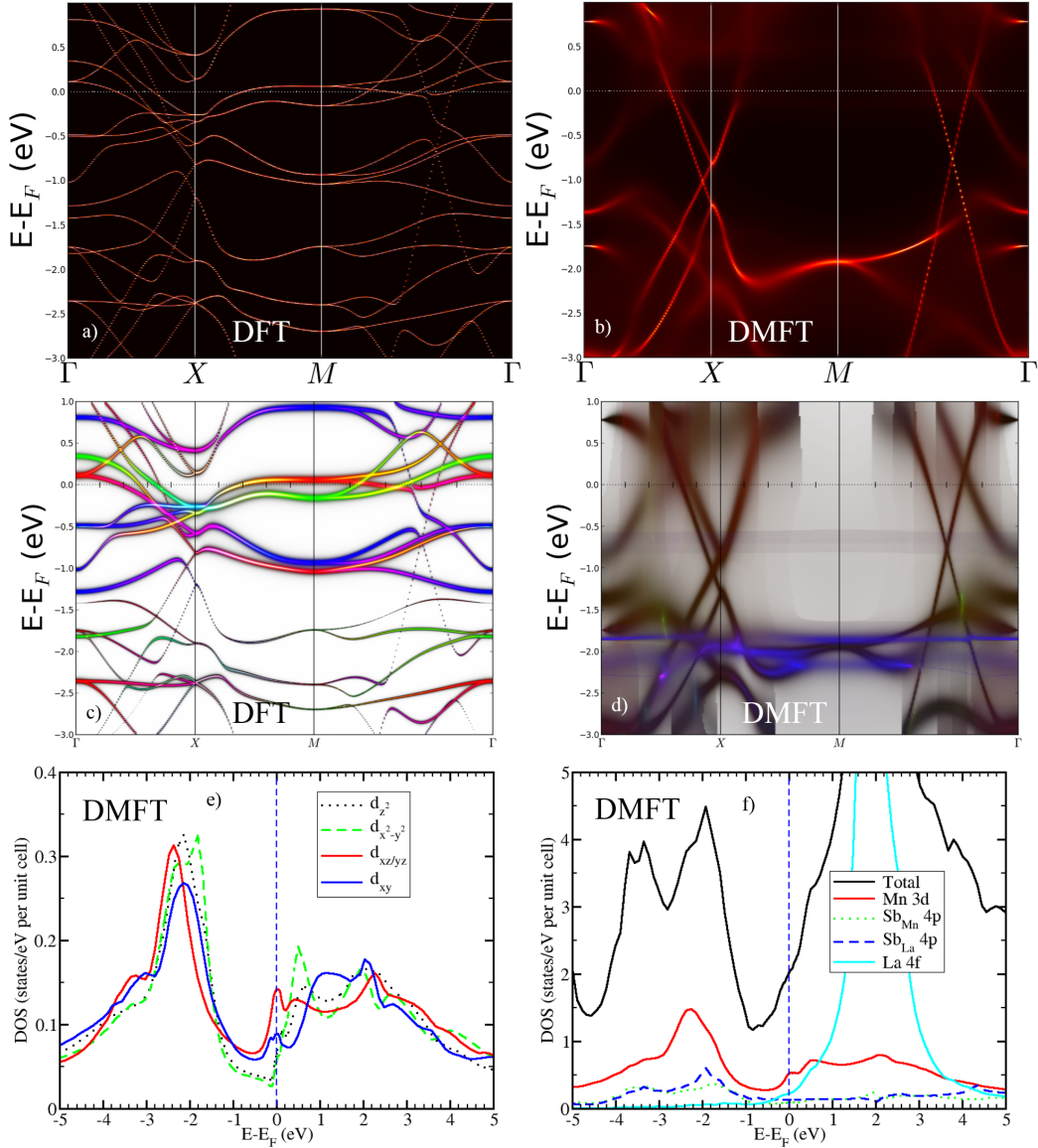
Figure 6.9: (a) DFT calculation of LaMnSb$_2$. (b) DFT+DMFT calculation of LaMnSb$_2$. (c) DFT calculation of LaMnSb$_2$ with different colors for different bands d$_{xy}$ (green) d$_{xz,yz}$ (brown/red) and d$_{z^2,x^2-y^2}$ (blue). (d) DFT+DMFT calculation of LaMnSb$_2$ with different colors for different bands d$_{xy}$ (green) d$_{xz,yz}$ (brown/red) and d$_{z^2,x^2-y^2}$ (blue). (e,f) Partial density of states for the calculation presented in (b,d) calculated using the muffin-tin approximation. Figures courtesy of Z.P. Yin (unpublished)

tween Mn and the Sb that tetrahedrally co-ordinates it. Moreover we have a contribution from the La-Sb layer. This is in contrast to pressurized metallic LaMnPO, where there is no contribution to the density of states at the Fermi level from the LaO layer [131]. This observation may be rationalized by considering our earlier comparison of the La position in the crystal structures of LaMnPO and $LaMn_xSb_2$, as presented in Figure 6.2. The larger size and lower electronegativity of Sb shifts the La in $LaMn_xSb_2$ to be equidistant from both Sb sites, unlike in LaMnPO where the LaO layer may be considered as a charge reservoir for the MnP layer.

6.4   Discussion

The experimental and theoretical results on $LaMn_xSb_2$ presented here suggest orbital selectivity due to a strong Hund's coupling is responsible for promoting a correlated metallic state. Previous studies of manganese pnictides have revealed mostly insulating behavior at ambient pressure as shown in Chapters 3, 4. However, it has been shown experimentally that LaMnPO becomes metallic by 16 GPa, with calculations suggesting an ordered moment of ≈ 1.5 μ_B at this pressure (see Figure 6.1). This much smaller ordered moment indicates the metallic phase in LaMnPO is less correlated than ambient pressure $LaMn_xSb_2$ that has ordered moment 2.9 μ_B/Mn. Indeed we have shown here that there is significant contribution to the Fermi surface from the La-Sb layer in $LaMn_xSb_2$, while no such bands due to the LaO layer are present at the Fermi surface in pressurized LaMnPO [131].

These results also draw immediate comparison to the iron chalcogenide superconductors, whose parent compounds are the most correlated of iron-based materials. In these compounds a high temperature orbitally selective Mott phase is reported to give way to a superconducting phase at low temperature [123, 132]. Our identification of $LaMn_xSb_2$ as an ambient pressure metallic manganese pnictide should allow for angle resolved photoemission measurements on $LaMn_xSb_2$ to determine whether the d_{xy} orbital is fully gapped and the degree of band renormalization. Our DMFT calculations above predict a d_{yz} band renormalization of 33 in $LaMn_xSb_2$, far larger than the band renormalizations between 4 and 5 reported in the iron chalcogenides [132]. This suggests $LaMn_xSb_2$, even though metallic, may still be overly correlated compared to its superconducting isostructural iron counterparts.

We have reported transport, specific heat and neutron diffraction measurements that reveal a correlated antiferromagnetic metallic state below $T_N = 130$ K. The metallic nature of this compound sets it apart from most square-net manganese pnictide compounds that are correlated insulators. DFT+DMFT

calculations of the electronic density of states, including a strong Hubbard U and Hund's J_H, find that $LaMn_xSb_2$ may be an orbitally selective Mott phase. We believe a closer examination of the electronic density of states near the Fermi level is warranted; for instance, by using angle-resolved photoemission spectroscopy.

Chapter 7

Concluding Remarks

An understanding of the key ingredients necessary for high temperature super-conductivity (HTSC) and the discovery of a room temperature superconductor have been two big open questions in science since the serendipitous discovery of HTSC in copper-based materials in 1986. This field was re-invigorated in 2008 with the, also serendipitous, discovery of HTSC in a new class of iron-based materials. Intensive experimental investigation of these two classes of materials have revealed somewhat similar phase diagrams (see Figure 1.2). One topic of much current debate is the importance of electron correlations in the metallic parent compounds of the iron-based HTSC and their proximity to Mott insulating phase [8]. In contrast, strong correlations are widely accepted as crucial to understand HTSC in copper-based materials [1].

In this work, we have presented results on three different manganese-based compounds, LaMnPO, $BaMn_2As_2$ and $LaMn_xSb_2$, that are isostructural with the parent compounds of the iron-based HTSC. No one technique can possibly characterize the complex interplay between spin, charge, lattice and orbital degrees of freedom (DOF) in strongly correlated materials. We have there-fore combined the resources in our lab with those of national user facilities and our experimental and theoretical collaborators to understand the inter-play between these DOF in manganese pnictide compounds. As outlined in detail in Chapters 3, 4, 6 we find that strong electronic correlations asso-ciated with intra-atomic Hund's coupling must be considered to understand the electronic and magnetic ground states of these nominally half-filled (d^5) manganese pnictide compounds.

Figure 7.1 provides a summary of the degree of correlation in these man-ganese pnictide systems and compares them to known iron pnictide and chalco-genide superconductors. The top panel of Figure 7.1 presents the renormal-ization of the d_{yz} band as a function of the filling of the 3d orbitals. For the manganese pnictide compounds the band renormalization and filling have

been calculated in the paramagnetic state using DFT+DMFT [133], while band renormalization for iron pnictide and chalcogenides have been reported from ARPES measurements [123, 132]. The parent compounds LaMnPO and BaMn$_2$As$_2$ are both found to be very strongly correlated with the lower bounds of the band renormalization between 35-50 and filling of the d-electron shell between 5.05-5.1. These large renormalization factors are consistent with our findings that these compounds are correlated Hund's insulators. In contrast the known iron-based superconductors are more moderately correlated with band renormalizations between 2.5-8. In addition superconductivity occurs between fillings of $\approx$5.5 (KFe$_2$As$_2$) and $\approx$ 6.15 (BaFe$_{1.7}$Co$_{0.3}$As$_2$), that is by electron or hole doping the antiferromagnetic metal BaFe$_2$As$_2$ to suppress the antiferromagnetism and induce superconductivity.

Measurements of the properties of LaMnPO under pressure have been reported in an attempt to drive it toward this region of superconductivity [54]. While these measurements showed promise in inducing an antiferromagnetic metallic and eventually paramagnetic metallic phase, no superconductivity was observed. DFT+DMFT calculations presented in figure 7.1 show that the band renormalization of $\approx$ 2.4 for this paramagnetic metallic phase that has filling of $\approx$ 5.4 is too small to allow for the same type of superconductivity that occurs in the iron compounds. This may be understood by considering the bottom panel of Figure 7.1 that presents the band renormalization as a function of transition metal-anion distance. The effect of 30 GPa on LaMnPO is to induce a structural transition from tetragonal to collapsed orthorhombic phase with drastic reduction in this distance [43]. Consequently the Mn-P hybridization becomes very strong and hence 30 GPa LaMnPO is rather weakly correlated and paramagnetic like non-superconducting LaFePO.

Our group has also tried extensively to chemically dope LaMnPO toward a metallic and perhaps superconducting state. No suitable dopant was identified, and LaMnPO was still antiferromagnetic and insulating after the introduction of $\approx$ 30 % fluorine [52]. Johnston et al. have also tried extensively to dope BaMn$_2$As$_2$, initially with limited success [135]. Eventually, potassium was identified as an appropriate dopant to metallize BaMn$_2$As$_2$ but with no effect on the local moment antiferromagnetism [46, 85], with ARPES measurements showing that K states are present at the Fermi level and dominate the transport. We would therefore expect the band renormalization and filling in metallized BaMn$_2$As$_2$ to be similar to that in the undoped compound. A similar metallic state is present in LaMn$_x$Sb$_2$ that is a strongly correlated metal as indicated in Figure 7.1 with antimony states likely dominating the transport properties.

The above results suggest that, so far, manganese compounds cannot be
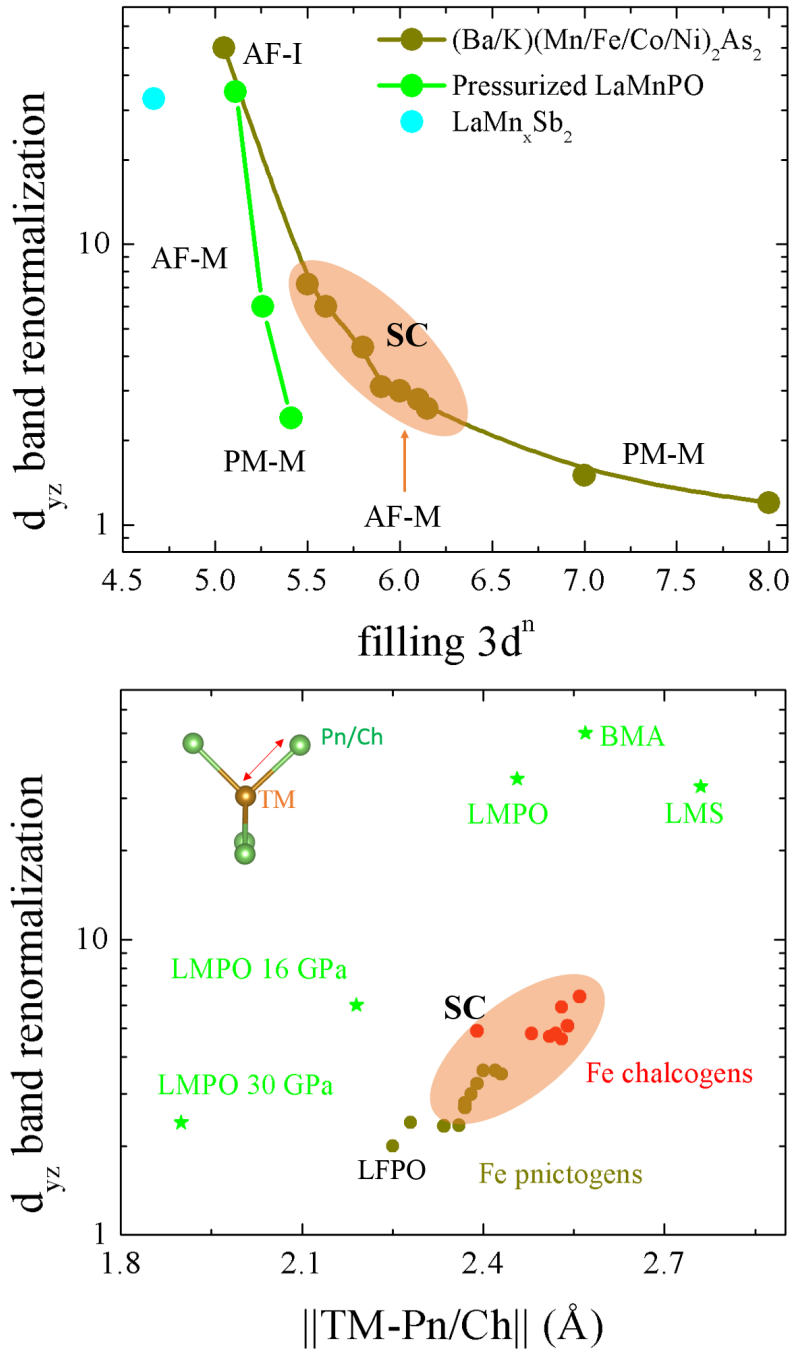
Figure 7.1: Band renormalization as a function of filling (top) and transition metal-anion distance (bottom). The highlighted region indicates where superconductivity is found. AF-M is antiferromagnetic metal, PM-M is paramagnetic metal, SC is superconductor, AF-I is antiferromagnetic insulator. LMPO is LaMnPO, BMS is $BaMn_2As_2$, LMS is $LaMn_xSb_2$. Data points taken from [50, 134]

driven into the moderately correlated region where superconductivity would be expected. However, there has been a recent report that the superconductor NaFeAs may be driven toward an insulating state by doping copper ions on iron sites [136]. This supports the idea that superconductivity in the iron pnictide compounds appears near a correlated insulating state and that manganese pnictide compounds could still be a source of new superconductors, if a suitable chemical dopant can be identified.

So far, the discovery of new superconducting materials has been overwhelmingly by chance. This is largely because we have not had the tools necessary to properly account for and predict materials properties, especially when strong correlations are present. In this work, we performed experiments that allowed us to guide our theoretical colleagues who used advanced electronic structure methods (DFT+DMFT), that include electron correlations, to properly account for the correlated insulating state in LaMnPO and $BaMn_2As_2$, i.e. they calculated the electronic density of states as would be measured by angle-resolved photoemission (ARPES). In addition, we find that DFT+DMFT can account for the correlated metallic state of $LaMn_xSb_2$ as shown in Chapter 6. Furthermore, in recent years these computational methods have also correctly predicted inelastic neutron scattering spectra [137] and optical conductivity data [67], as well as the stability of different structures [138]. The next step is then to identify common structures and spectral features in the afore-mentioned scattering methods, as well as rapidly developing techniques such as resonant inelastic x-ray scattering (RIXS) [139], that correlate with useful material properties such as superconductivity. With more advanced computational tools being made available to a wider user base, we may then rapidly identify candidate materials that host the desired structures and excitations, thereby overcoming serendipity in finding new useful materials.

It is then clear that the work in Chapters 3, 4, 6 quite generally contributes to our understanding of the conditions under which superconductivity may occur, as well as the goal of theory-assisted design of new high temperature superconductors. A common framework based on orbital filling and orbital selectivity due to Hund's coupling may be employed to understand the correlations in the manganese pnictide systems studied here, as well as in the iron pnictide and chalcogenide superconductors. Future superconductor materials design approaches should employ a wide array of scattering techniques in concert with computational methods that can account for strong electronic correlations, as these are common to all known types of HTSC.

Finally, in the course of our investigations we also identified large single crystals of $CaMn_2Sb_2$. This compound does not adopt a structure that hosts

the square nets of 3d transition metals common to all HTSC. Rather, the Mn ions form on a corrugated honeycomb lattice. There is significant interest currently in honeycomb lattice materials in the context of spin liquids and Kitaev physics. We noted there are very few honeycomb lattice compounds for which individual exchange interactions had been determined due to several factors such as a lack of large single crystals. We therefore undertook inelastic neutron scattering measurements of $CaMn_2Sb_2$ and analyzed these data to determine exchange interactions. Interestingly we found that, while $CaMn_2Sb_2$ orders antiferromagnetically at 85 K, our determination of the exchange interactions situates it very near to a tricritical point where three different types of long range magnetic order co-exist. This proximity frustrates the formation of long range magnetic order from its mean field value. The identification of a compound with similar structure type but with smaller magnetic moments may lead to the identification of a spin liquid phase on this lattice.

Bibliography

[1] M. Imada, A. Fujimori, and Y. Tokura. Metal-insulator transitions. *Rev. Mod. Phys.*, 70:1039, 1998.

[2] J.H. de Boer and E.J.W. Verwey. Semiconductors with partially and with completely filled 3d lattice bands. *Proc. Phys. Soc.*, 49:59, 1937.

[3] N.F. Mott. The Basis of the Electron Theory of Metals, with Special Reference to the Transition Metals. *Proc. Phys. Soc. A*, 62:416, 1949.

[4] G. Kotliar, S.Y. Savrasov, K. Haule, V.S. Oudovenko, O. Parcollet, and C.A. Marianetti. Electronic structure calculations with dynamical mean-field theory. *Rev. Mod. Phys.*, 78, 2006.

[5] G. Kotliar and D. Vollhardt. Strongly Correlated Materials: Insights From Dynamical Mean Field Theory. *Phys. Today*, 57:53, 2004.

[6] S.M. Griffin, P. Staar, T.C. Schulthess, M. Troyer, and N.A. Spaldin. A Bespoke Single-Band Hubbard Model Material. *arXiv*, page 1508.04357, 2015.

[7] D.C. Johnston. The puzzle of high temperature superconductivity in layered iron pnictides and chalcogenides. *Adv. Phys.*, 59:803, 2010.

[8] P.D. Johnson, G. Xu, and W.G. Yin. Iron-Based Superconductivity. *Springer*, 2015.

[9] L. de' Medici. Hunds coupling and its key role in tuning multiorbital correlations. *Phys. Rev. B*, 83:205112, 2011.

[10] D.N. Basov and A.V. Chubukov. Manifesto for a higher T_c. *Nat. Phys.*, 7:272, 2011.

[11] L. de' Medici, S.R. Hassan, M. Capone, and X. Dai. Orbital-Selective Mott Transition out of Band Degeneracy Lifting. *Phys. Rev. Lett.*, 102:126401, 2009.

[12] S. Blundell. Magnetism in Condensed Matter. *Oxford University Press*, 2011.

[13] D.C. Johnston, R.J. McQueeney, B. Lake, A. Honecker, M.E. Zhitomirsky, R. Nath, Y. Furukawa, V.P. Antropov, and Y. Singh. Magnetic exchange interactions in $BaMn_2As_2$: A case study of the J_1-J_2-J_c Heisenberg model. *Phys. Rev. B*, 84:094445, 2011.

[14] K. Haule and G. Kotliar. Coherence-incoherence crossover in the normal state of iron oxypnictides and importance of Hund's rule coupling. *New J. Physics*, 11:025021, 2009.

[15] A. Georges, L. de' Medici, and J. Mravlje. Strong Correlations from Hund's Coupling. *Ann. Rev. Cond. Mat. Phys.*, 4:137, 2013.

[16] I. Lo Vecchio, A. Perucchi, P. Di Pietro, O. Limaj, U. Schade, Y. Sun, M. Arai, K. Yamaura, and S. Lupi. Infrared evidence of a Slater metal-insulator transition in $NaOsO_3$. *Nature Scientific Reports*, 3:2990, 2013.

[17] Hyun-Jung Kim, Jun-Ho Lee, and Jun-Hyung Cho. Antiferromagnetic Slater Insulator Phase of Na_2IrO_3. *Nat. Sci. Rep.*, 4:5253, 2014.

[18] N.W. Ashcroft and N.D. Mermin. Solid State Physics. *Brookes Cole*, 1976.

[19] C. Dekker, A.F.M. Arts, H.W. de Wijn, A.J. van Duyneveldt, and J.A. Mydosh. Activated Dynamics in the Two-Dimensional Ising Spin-Glass $Rb_2Cu_{1-x}Co_xF_4$. *Phys. Rev. Lett.*, 61:1780, 1988.

[20] K. Ross. Neutron Scattering Studies of $Yb_2Ti_2O_7$. *PhD thesis McMaster University*, 2012.

[21] J.S. Helton, K. Matan, M.P. Shores, E.A. Nytko, B.M. Bartlett, Y. Qiu, D.G. Nocera, and Y.S. Lee. Dynamic Scaling in the Susceptibility in the Susceptibility of the Spin-1/2 Kagome Lattice Antiferromagnet Herbertsmithite. *Phys. Rev. Lett.*, 104:147201, 2010.

[22] A.P. Ramirez. Strongly Geometrically Frustrated Magnets. *Annu. Rev. Mater. Sci.*, 24:453–480, 1994.

[23] D.E. McNally, J.W. Simonson, K.W. Post, Z.P. Yin, M. Pezzoli, G.J. Smith, V. Leyva, C. Marques, L. DeBeer-Schmitt, A.I. Kolesnikov, Y. Zhao, J.W. Lynn, D.N. Basov, G. Kotliar, and M.C. Aronson. Origin of the charge gap in LaMnPO. *Phys. Rev. B*, 90:180403(R), 2014.

[24] D. E. McNally, S. Zellman, Z. P. Yin, K. W. Post, Hua He, K. Hao, G. Kotliar, D. Basov, C. C. Homes, and M. C. Aronson. From Hund's insulator to Fermi liquid: Optical spectroscopy of K doping in $BaMn_2As_2$. *Phys. Rev. B*, 92:115412, 2015.

[25] D. E. McNally, J. W. Simonson, J. J. Kistner-Morris, G. J. Smith, J. E. Hassinger, L. DeBeer-Schmidt, A. I. Kolesnikov, I. A. Zaliznyak, and M. C. Aronson. CaMn2Sb2: Spin waves on a frustrated antiferromagnetic honeycomb lattice. *Phys. Rev. B*, 91:180407, 2015.

[26] I.R. Fisher, M.C. Shapiro, and J.G. Analytis. Principles of crystal growth of intermetallic and oxide compounds from molten solutions. *Philosophical Magazine*, 92(19–21):2401–2435, 2012.

[27] J. Boltersdorf, N. King, and P.A. Maggard. Flux-mediated crystal growth of metal oxides: synthetic tunability of particle morphologies, sizes, and surface features for photocatalysis research. *CrystEngComm*, 17:2225, 2015.

[28] A.T. Nientiedt. Quaternary equiatomic manganese pnictide oxides AMnPO (A = La-Nd, Sm, Gd-Dy), AMnAsO (A = Y, La-Nd, Sm, Gd-Dy, U), and AMnSbO (A = La-Nd, Sm, Gd) with ZrCuSiAs type structure. *Zeitschrift fur Naturforschung B*, 52B:560–564, 1997.

[29] E. Brechtel, G. Cordier, and H. Schaefer. Neue ternre Erdalkaliverbindungen des Arsens mit Mangan. *Z. Naturforsch. B*, 33, 1978.

[30] S. Bobev, J. Merz, A. Lima, V. Fritsch, J.D. Thompson, J.L. Sarrao, M. Gillessen, and R. Dronkowski. Unusual MnMn Spin Coupling in the Polar Intermetallic Compounds $CaMn_2Sb_2$ and $SrMn_2Sb_2$. *Inorg. Chem.*, 45:4047, 2006.

[31] J.W. Simonson, G.J. Smith, K Post, M Pezzoli, J.J. Kistner-Morris, D.E. McNally, J.E. Hassinger, C.S. Nelson, G. Kotliar, D.N. Basov, and M.C. Aronson. Magnetic and structural phase diagram of $CaMn_2Sb_2$. *Phys. Rev. B*, 86:184430, 2012.

[32] G. Cordier, H. Schaefer, and P. Woll. Besetzungsvarianted der CaMnBi2-Struktur: Zur Kenntnis der Verbindungen $LaZn_{0.52}Sb2$, $LaCo_{0.68}Sb_2$, $LaMn_xSb_2$ (0.68-x-0.76) und LaC_xSb_2 (0.82-x-0.87). *Zeitschrift fuer Naturforschung B*, 40:1097, 1985.

[33] T. Okita and Y. Makino. Crystal Magnetic Anisotropy and Magnetization of MnSb. *Journal of the Physical Society of Japan*, 25:120, 1968.

[34] Q.D. Gibson, H. Wu, T. Liang, M.N. Ali, N.P. Ong, Q. Huang, and R.J. Cava. Magnetic and electronic properties of $CaMn_2Bi_2$: A possible hybridization gap semiconductor. *Phys. Rev. B*, 91, 2015.

[35] Quantum Design, Physical Property Measurement System: Heat Capacity Option User's Manual.

[36] L.S. Wu. Quantum Critical Behaviors in Magnetic Systems: Yb_3Pt_4, YFe_2Al_{10} and Yb_2Pt_2Pb.

[37] I.A. Zaliznyak and J.M. Tranquada. Neutron Scattering and Its Application to Strongly Correlated Systems. In A. Avella and F. Mancini, editors, *Strongly Correlated Systems: Experimental Techniques*. Springer, Switzerland, 2015.

[38] G.L. Squires. Chapter 7: Magnetic scattering - basic theory. In *Introduction to the theory of Thermal Neutron Scattering*. Cambridge University Press, Cambridge, 1978.

[39] G. Shirane, S.M. Shapiro, and J.M. Tranquada. Neutron Scattering with a Triple-Axis Spectrometer: Basic Techniques. *Cambridge University Press*, 2006.

[40] G.E. Granroth, A.I. Kolesnikov, T.E. Sherline, J.P. Clancy, K.A. Ross, J.P.C. Ruff, B.D. Gaulin, and S.E. Nagler. SEQUIOA: a newly operating chopper spectrometer at the SNS. *J. Phys.: Conf. Ser.*, 251:012058, 2010.

[41] W. Bronger and P. Müller. Framework structures in metal chalcogenides and the characterization of their bonding by magnetic properties. *J. Less Common Metals*, 100:241, 1984.

[42] A. Continenza, S. Picozzi, W.T. Geng, and A.J. Freeman. Coordination and chemical effects on the structural, electronic, and magnetic properties in Mn pnictides. *Phys. Rev. B*, 64:085204, 2001.

[43] J.W. Simonson, Z.P. Yin, M Pezzoli, K. Guo, J. Post, A. Efimenko, N. Hollmann, Z. Hu, H.-J. Lin, C.T. Chen, C. Marques, V. Leyva, G. Smith, J.W. Lynn, L.L. Sun, G. Kotliar, D.N. Basov, L.H. Tjeng, and M.C. Aronson. From antiferromagnetic insulator to correlated metal in pressurized and doped LaMnPO. *Proc. Nat.*, 109:E1815, 2012.

[44] P.A. Lee, N. Nagaosa, and X.G. Wen. Doping a Mott insulator: Physics of high-temperature superconductivity. *Rev. Mod. Phys.*, 78:17, 2006.

[45] Y. Kamihara, T. Watanabe, M. Hirano, and H. Hosono. Iron-Based Layered Superconductor La[$O_{1-x}F_x$]FeAs (x = 0.050.12) with T_c = 26 K. *J. Am. Chem. Soc.*, 130:3296, 2008.

[46] A. Pandey, R.S. Dhaka, J. Lamsal, Y. Lee, and A. Kreyssig V.K. Anand, T.W. Heitmann, R.J. McQueeney, A.I. Goldman, B.N. Harmon, A. Kaminski, and D.C. Johnston. $Ba_{1x}K_xMn_2As_2$: An Antiferromagnetic Local-Moment Metal. *Phys. Rev. Lett.*, 108:087005, 2012.

[47] B. Saparov and A.S. Sefat. Crystals, magnetic and electronic properties of a new $ThCr_2Si_2$-type $BaMn_2Bi_2$ and K-doped compositions. *J. Sol. St. Chem.*, 204:32, 2013.

[48] J.-G. Cheng, K. Matsubayashi, W. Wu, J.P. Sun, F.K. Lin, J.L. Luo, and Y. Uwatoko. Pressure Induced Superconductivity on the border of Magnetic Order in MnP. *Phys. Rev. Lett.*, 114:117001, 2015.

[49] A. Georges, G. Kotliar, W. Krauth, and M.J. Rozenberg. Dynamical mean-field theory of strongly correlated fermion systems and the limit of infinite dimensions. *Rev. Mod. Phys.*, 68:13, 1996.

[50] Z. P. Yin, K. Haule, and G. Kotliar. Kinetic frustration and the nature of the magnetic and paramagnetic states in iron pnictides and iron chalcogenides. *Nature Materials*, 10:932, 2011.

[51] H. Yanagi, K. Fukuma, T. Kamiya, M. Hirano, and H. Hosono. Electrical and magnetic properties of quaternary compounds LnMnPO (Ln = Nd, Sm, Gd) with ZrCuSiAs-type structure. *Materials Science and Engineering B*, 173:47, 2010.

[52] J.W. Simonson, K. Post, C. Marques, G. Smith, O. Khatib, D.N. Basov, and M.C. Aronson. Gap states in insulating $LaMnPO_{1x}F_x$ (x=0,0.3). *Phys. Rev. B*, 84:165129, 2011.

[53] H. Yanagi, T. Watanabe, K. Kodama, S. Iikubo, S. Shamoto, T. Kamiya, M. Hirano, and H. Hosono. Antiferromagnetic bipolar semiconductor LaMnPO with ZrCuSiAs-type structure. *J. Appl. Phys.*, 105:093916, 2009.

[54] J. Guo, J.W. Simonson, L.L. Sun, Q. Wu, P. Gao, C. Zhang, D. Gu, G. Kotliar, M.C. Aronson, and Z. Zhao. Observation of antiferromagnetic order collapse in the pressurized insulator LaMnPO. *Nat. Sci. Rep.*, 3:2555, 2013.

[55] J.W. Lynn, Y. Chen, S. Chang, Y. Zhao, S. Chi, W. Ratcliff II, B.G. Ueland, and R.W. Erwin. Double Focusing Thermal Triple Axis Spectrometer at the NCNR. *J. Research NIST*, 117:61, 2012.

[56] A. Zheludev. Reslib. *Oak Ridge National Lab, TN*, 2001.

[57] M.J. Cooper and R. Nathans. The resolution function in neutron diffractometry. I. The resolution function of a neutron diffractometer and its application to phonon measurements. *Acta Cryst.*, 23:357, 1967.

[58] N.J. Chesser and J.D. Axe. Determination and experimental verification of the normalized resolution function for inelastic neutron scattering. *Acta Cryst.*, page 160, 1973.

[59] M.F. Collins. Magnetic Critical Scattering. *Oxford University Press*, 1989.

[60] P.J. Brown. Magnetic form factors. *International tables for crystallography vol. C (A.J.C. Wilson, ed.).*

[61] S.W. Lovesey. Theory of Neutron Scattering from Condensed Matter: Volume 2. *Clarendon Press*, 1986.

[62] B.I. Chakravarty, B.I. Halperin, and D.R. Nelson. Two-dimensional quantum Heisenberg antiferromagnet at low temperatures. *Phys. Rev. B*, 39:2344, 1989.

[63] D.C. Johnston. Unified molecular field theory for collinear and non-collinear Heisenberg antiferromagnets. *Phys. Rev. B*, 91:064427, 2015.

[64] D.C. Johnston. . *Handbook of Magnetic Materials*, 10:1, 1997.

[65] M. Takahashi. Modified spin-wave theory of a square-lattice antiferromagnet. *Phys. Rev. B*, 40:2494, 1989.

[66] E. Rosencher and B. Vinter. Optoelectronics. *Cambridge University Press*, 2002.

[67] Z.P. Yin, K. Haule, and G. Kotliar. Magnetism and charge dynamics in iron pnictides. *Nature Physics*, 7:294, 2011.

[68] A. Kutepov, K. Haule, S.Y. Savrasov, and G. Kotliar. Self-consistent GW determination of the interaction strength: Application to the iron arsenide superconductors. *Phys. Rev. B*, 82:045105, 2010.

[69] J. Mravlje, M. Aichhorn, T. Miyake, K. Haule, G. Kotliar, and A. Georges. Coherence-Incoherence Crossover and the Mass-Renormalization Puzzles in Sr_2RuO_4. *Phys. Rev. Lett.*, 106:096401, 2011.

[70] Z.P. Yin, K. Haule, and G. Kotliar. Fractional power-law behavior and its origin in iron-chalcogenide and ruthenate superconductors: Insights from first-principles calculations. *Phys. Rev. B*, 86:195141, 2012.

[71] J. Kunes, V. Yukoyanov, V.I. Anisimov, R.T. Scalettar, and W.E. Pickett. Collapse of magnetic moment drives the Mott transition in MnO. *Nat. Mater.*, 7:198, 2008.

[72] Y. Singh, A. Ellern, and D.C. Johnston. Magnetic, transport, and thermal properties of single crystals of the layered arsenide $BaMn_2As_2$. *Phys. Rev. B*, 79:094519, 2009.

[73] Y. Singh, M.A. Green, Q. Huang, A. Kreyssig, R.J. McQueeney, D.C. Johnston, and A.I. Goldman. Magnetic order in $BaMn_2As_2$ from neutron diffraction measurements. *Phys. Rev. B*, 80:100403, 2009.

[74] A. Antal, T. Knoblacuh, Y. Singh, P. Gegenwart, D. Wu, and M. Dressel. Optical properties of the iron-pnictide analog $BaMn_2As_2$. *Phys. Rev. B*, 86:014506, 2012.

[75] J. An, A.S. Sefat, D.J. Singh, and Mao-Hua Du. Electronic structure and magnetism in $BaMn_2As_2$ and $BaMn_2Sb_2$. *Phys. Rev. B*, 79:075120, 2009.

[76] K. Kayanuma, H. Hiramatsu, T. Kamiya, M. Hirano, and H. Hosono. Epitaxial film growth and optoelectrical properties of layered semiconductors, LaMnXO (X = P, As, and Sb). *J. Appl. Phys.*, 105:073903, 2009.

[77] C.C. Homes, M. Reedyk, D.A. Crandles, and T. Timusk. Technique for measuring the reflectance of irregular, submillimeter-sized samples. *Appl. Opt.*, 32(16):2976, 1993.

[78] K. Haule, C.H. Yee, and K. Kim. Dynamical mean-field theory within the full-potential methods: Electronic structure of $CeIrIn_5$, $CeCoIn_5$, and $CeRhIn_5$. *Phys. Rev. B*, 81, 2010.

[79] P. Blaha, K. Schwarz, G. Madsen, D. Kvasnicka, and J. Luitz. . *K. Schwarz, Techn. Univ. Wien*, 2001.

[80] J.P. Perdew, K. Burke, and M. Ernzerhof. Generalized Gradient Approximation Made Simple. *Phys. Rev. Lett*, 77, 1996.

[81] B. G. Ueland, A. Pandey, Y. Lee, A. Sapkota, Y. Choi, D. Haskel, R. A. Rosenberg, J. C. Lang, B. N. Harmon, D. C. Johnston, A. Kreyssig, and A. I. Goldman. Itinerant ferromagnetism in the As 4p conduction band of $Ba_{0.6}K_{0.4}Mn_2As_2$ identified by X-ray magnetic circular dichroism. *Phys. Rev. Lett.*, 114:217001, 2015.

[82] A.B. Kuzmenko. Kramers-Kronig constrained variational analysis of optical spectra. *Rev. Sci. Instrum.*, 76, 2005.

[83] S.L. Brock, J.E. Greedan, and S.M. Kauzlarich. Resistivity and Magnetism of AMn_2P_2 (A = Sr, Ba): The Effect of Structure Type on Physical Properties. *Journal of Solid State Chemistry*, 113, 1994.

[84] J. Lamsal, G.S. Tucker, T.W. Heitmann, A. Kreyssig, A. Jesche, A. Pandey, W. Tian, R.J. McQueeney, D.C. Johnston, and A.I. Goldman. Persistence of local-moment antiferromagnetic order in $Ba_{1x}K_xMn_2As_2$. *Phys. Rev. B*, 87, 2013.

[85] A. Pandey, B. G. Ueland, S. Yeninas, A. Kreyssig, A. Sapkota, Yang Zhao, J. S. Helton, J.W. Lynn, R. J. McQueeney, Y. Furukawa, A. I. Goldman, and D. C. Johnston. Coexistence of half-metallic itinerant ferromagnetism with local-moment antiferromagnetism in $Ba_{0.60}K_{0.40}Mn_2As_2$. *Phys. Rev. Lett.*, 111:047001, 2013.

[86] S. Yeninas, A. Pandey, V. Ogloblichev, K. Mikhalev, D.C. Johnston, and Y. Furukawa. Metal-insulator transition in antiferromagnetic $Ba_{1-x}K_xMn_2As_2$ (0x0.4) single crystals studied by ^{55}Mn and ^{75}As NMR. *Phys. Rev. B*, 88, 2013.

[87] Jin-Ke Bao, Hao Jiang, Yun-Lei Sun, Wen-He Jiao, Chen-Yi Shen, Han-Jie Guo, Ye Chen, Chun-Mu Feng, Hui-Qiu Yuan, Zhu-An Xu, Guang-Han Cao, Ryo Sasaki, Toshiki Tanaka, Kazuyuki Matsubayashi, and Yoshiya Uwatoko. Weakly ferromagnetic metallic state in heavily doped $Ba_{1-x}K_xMn_2As_2$. *Phys. Rev. B*, 85, 2012.

[88] Y.M. Dai, B. Xu, B. Shen, H. Xiao, H.H. Wen, X.G. Qiu, C.C. Homes, and R.P.S.M. Lobo. Hidden T-Linear Scattering Rate in $Ba_{0.6}K_{0.4}Fe_2As_2$ Revealed by Optical Spectroscopy. *Phys. Rev. Lett.*, 111, 2013.

[89] T. Hanna, S. Matsuishi, K. Kodama, T. Otomo, S.I. Shamoto, and H. Hosono. From antiferromagnetic insulator to ferromagnetic metal: Effects of hydrogen substitution in LaMnAsO. *Phys. Rev. B*, 87, 2013.

[90] Abhishek Pandey and D.C. Johnston. $Ba_{0.4}Rb_{0.6}Mn_2As_2$: A Prototype Half-Metallic Ferromagnet. *arXiv*, 2015.

[91] L. Balents. Spin liquids in frustrated magnets. *Nature*, 464:199–208, 2010.

[92] E. Rastelli, A. Tassi, and L. Reatto. Non-simple magnetic order for simple Hamiltonians. *Physica B*, 97:1, 1979.

[93] Katsura, S. and Ide, T. and Morita, T. The ground states of the classical heisenberg and planar models on the triangular and plane hexagonal lattices. *J. Stat. Phys.*, 42(3–4):381, 1986.

[94] Z.Y. Meng, T.C. Lang, S. Wessel, F.F. Assad, and A. Muramatsu. Quantum spin liquid emerging in two-dimensional correlated Dirac fermions. *Nature*, 464:847, 2010.

[95] R. Flint and P.A. Lee. Emergent honeycomb lattice in $LiZn_2Mo_3O_8$. *Phys. Rev. Lett.*, 111:217201, 2013.

[96] S.S. Gong, D.N. Sheng, O.I. Motrunich, and M.P.A. Fisher. Phase diagram of the spin 1/2 J_1-J_2 Heisenberg model on a honeycomb lattice. *Phys. Rev. B*, 88:165138, 2013.

[97] Z. Zhu, D.A. Huse, and S.R. White. Weak plaquette valence bond order in the S = 1/2 honeycomb J_1-J_2 Heisenberg model. *Phys. Rev. Lett.*

[98] Y. Ishikawa and S. Akimoto. Magnetic property and crystal chemistry of Ilmenite ($MeTiO_3$) and Hematite (αFe_2O_3) System II. Magnetic Property. *J. Phys. Soc. Jap.*

[99] S. Eymond and A. Durif. Donnees cristallographiques sur quelques composes isomorphes du monoarseniate de baryum-nickel : $BaNi_2(AsO_4)_2$. *Mat. Res. Bull.*, 4:595, 1969.

[100] G Shirane, S.J. Pickart, and Y. Ishikawa. Neutron diffraction study of antiferromagnetic $MnTiO_3$ and $NiTiO_3$. *J. Phys. Soc. Jap.*, 14(10):1352, 1959.

[101] L.P. Regnault, J. Rossat-Mignod, J.Y. Henry, and L.J. DeJongh. Magnetic properties of the quasi-2D easy plane antiferromagnet $BaNi_2(PO_4)_2$. *J. Magn. Magn. Mater.*, 31–34:1205, 1983.

[102] Y. Todate, Y. Ishikawa, K. Tajima, S. Tomiyoshi, and H. Takei. Spin dynamics in a quasi-two dimensional antiferromagnet $MnTiO_3$. *J. Phys. Soc. Jap.*, 55(12):4464, 1986.

[103] O. Smirnova, M. Azuma, N. Kumada, Y. Kusano, M. Matsuda, Y. Shimakawa, T. Takei, Y. Yonesaki, and N. Kinomura. Synthesis, crystal structure and magnetic properties of $Bi_3Mn_4O_{12}(NO_3)$ oxynitrate comprising S = 3/2 honeycomb lattice. *J. Am. Chem. Soc.*, 131:8313–8317, 2009.

[104] Y. Singh and P. Gegenwart. Antiferromagnetic Mott insulating state in single crystals of the honeycomb lattice material Na_2IrO_3. *Phys. Rev. B*, 82:064412, 2010.

[105] X. Liu, T. Berlijn, W.-G. Yin, W. Ku, A. Tsvelik, Young-June Kim, H. Gretarsson, Y. Singh, P. Gegenwart, and J.P. Hill. Long-range magnetic ordering in Na_2IrO_3. *Phys. Rev. B*, 83:220403(R), 2011.

[106] Y. Singh, S. Manni, J. Reuther, T. Berlijn, R. Thomale, W. Ku, S. Trebst, and P. Gegenwart. Relevance of the Heisenberg-Kitaev model for the honeycomb lattice iridates A_2IrO_3. *Phys. Rev. Lett.*, 108:127203, 2012.

[107] K.W. Plumb, J.P. Clancy, L.J. Sandilands, V.V. Shankar, Y.F. Hu, K.S. Burch, Hae-Young Kee, and Young-June Kim. α-$RuCl_3$: A spin-orbit assisted Mott insulator on a honeycomb lattice. *Phys. Rev. B*, 90:041112, 2014.

[108] H. Karunadasa, Q. Huang, B.G. Ueland, J.W. Lynn, P. Schiffer, K.A. Regan, and R.J. Cava. Honeycombs of triangles and magnetic frustration in SrL_2O_4 (L = Gd, Dy, Ho, Er, Tm, and Yb). *Phys. Rev. B*, 71:144414, 2005.

[109] E. Climent-Pascual, P. Norby, N.H. Andersen, P.W. Stephens, H.W. Zandbergen, J. Larsen, and R.J. Cava. Spin 1/2 delafossite honeycomb compound Cu_5SbO_6. *Inorg. Chem.*, 51:557–565, 2012.

[110] J.H. Roudebush, N.H. Andersen, R. Ramlau, V.O. Garlea, R. Toft-Petersen, P. Norby, R. Scheider, J.N. Hay, and R.J. Cava. Structure

and magnetic properties of $Cu_3Ni_2SbO_6$ and $Cu_3Co_2SbO_6$ delafossites with honeycomb lattices. *Inorg. Chem.*, 52:6083–6095, 2013.

[111] M. Matsuda, M. Azuma, M. Tokunaga, Y. Shimakawa, and N. Kumada. Disordered ground state and magnetic field-induced long-range order in an S = 3/2 antiferromagnetic honeycomb lattice compound $Bi_3Mn_4O_{12}(NO_3)$. *Phys. Rev. Lett.*, 105:187201, 2010.

[112] H.C. Kandpal and J. van den Brink. Calculation of magnetic exchange couplings in the S = 3/2 honeycomb system $(Bi_3Mn_4O_{12})NO_3$ from first principles. *Phys. Rev. B*, 83:140412(R), 2011.

[113] H. Wadati, K. Kato, Y. Wakisaka, T. Sudayama, D.G. Hawthorn, T.Z. Regier, N. Onishi, M. Azuma, Y. Shimakawa, T. Mizokawa, A. Tanaka, and G.A. Sawatzky. Magnetic frustration in a Mn honeycomb lattice induced by Mn-O-O-Mn pathways. *arXiv:1101.2847*, 2011.

[114] S.K. Choi, R. Coldea, A.N. Kolmogorov, T. Lancaster, I.I. Mazin, S.J. Blundell, P.G. Radaelli, Y. Singh, P. Gegenwart, K.R. Choi, S.-W Cheong, P.J. Baker, C. Stock, and J. Taylor. Spin waves and revised crystal structure of honeycomb iridate Na_2IrO_3. *Phys. Rev. Lett.*, 108: 127204, 2012.

[115] H. Gretarsson, J.P. Clancy, Y. Singh, P. Gegenwart, J.P. Hill, Jungho Kim, M.H. Upton, A.H. Said, D. Casa, T. Gog, and Young-June Kim. Magnetic excitation spectrum of Na_2IrO_3 probed with resonant inelastic x-ray scattering. *Phys. Rev. B*, 87:220407(R), 2013.

[116] I.I. Mazin. $CaMn_2Sb_2$: A fully frustrated classical magnetic system. *arXiv:1309.3744*, 2013.

[117] G. Cordier and H.Z. Schafer. Neue intermetallische Verbindungen im anti-Ce_2O_2S-Strukturtyp. *Naturforsch*, 31B:1459, 1976.

[118] W. Ratcliff II, A.L. Lima, A.M. Gomes, J.L. Gonzalez, Q. Huang, and J. Singleton. The magnetic ground state of $CaMn_2Sb_2$. *J. Magn. Magn. Mater.*, 321:2612, 2009.

[119] C.A. Bridges, V.V. Krishnamurthy, S. Poulton, M.P. Paranthaman, B.C. Sales, C. Myers, and S. Bobev. Short and long range magnetic order in $CaMn_2Sb_2$ studied via powder neutron diffraction. *J. Magn. Magn. Mater.*, 321:3653, 2009.

[120] I.A. Zaliznyak. Spin structures and spin wave excitations. *Handbook of Magnetism and Advanced Magnetic Materials*, 2007.

[121] I.A. Zaliznyak and S.-H. Lee. Magnetic neutron scattering. *Modern Techniques for Characterizing Magnetic Materials, Edition: 1, Chapter: 1, Publisher: Springer, Editors: Y. Zhu*, page 3, 2005.

[122] G.J. MacDougall, D. Gout, J.L. Zaretsky, G. Ehlers, A. Podlesnyak, M.A. McGuire, and S.E. Mandrus, D Nagler. Kinetically inhibited order in a diamond-lattice antiferromagnet. *Proc. Nat. Ac. Sci.*, 108:15693, 2011.

[123] M. Yi, D.-H. Lu, R. Yu, S.C. Riggs, J.-H. Chu, B. Lv, Z.K. Liu, M. Lu, Y.-T. Cui, M. Hashimoto, Z. Hussain S.-K. Mo, Q. Si C.W. Chu, I.R. Fisher, and Z.-X. Shen. Observation of Temperature-Induced Crossover to an Orbital-Selective Mott Phase in $A_xFe_{2-y}Se_2$ (A = K,Rb) Superconductors). *Phys. Rev. Lett.*, 110:067003, 2013.

[124] P. Wollesen, W. Jeitschko, M. Brylak, and L. Dietrich. Ternary antimonides $LnM_{1-x}Sb_2$ with Ln = La-Nd, Sm, Gd, Tb and M = Mn, Co, Au, Zn, Cd. *Journal of Alloys and Compounds*, 245:L5–L8, 1996.

[125] E.S. Bozin, A.S. Masadeh, Y.S. Hor, J.F. Mitchell, and S.J.L. Billinge. Detailed Mapping of the Local Ir^{4+} Dimers through the Metal-Insulator Transitions of $CuIr_2S_4$ Thiospinel by X-Ray Atomic Pair Distribution Function Measurements. *Phys. Rev. Lett.*, 106:045501, 2011.

[126] J. Rodriguez-Carvajal. Recent advances in magnetic structure determination by neutron powder diffraction. *Physica B*, 192:55, 1993.

[127] Eric Fawcett. Spin density wave antiferromagnetism in chromium. *Rev. Mod. Phys.*, 60:209, 1988.

[128] B. Saparov, D.J. Singh, O.V. Garlea, and A.S. Sefat. Crystal, magnetic, and electronic structures, and properties of new BaMnPnF (Pn = As, Sb, Bi). *Scientific Reports*, 3:2154, 2013.

[129] A.S. Wills. SARAh - Representational Analysis. 1999.

[130] A.S. Wills. SARAh - Refine for GSAS, FullProf and TOPAS. 1999.

[131] Private communication with Z.P. Yin (Rutgers) and K.W. Post (UCSD). .

[132] M. Yi, Z.-K. Liu, Y. Zhang, R. Yu, J.-X. Zhu, J.J. Lee, R.G. Moore, F.T. Schmitt, S.C. Riggs, J.-H. Chu, M. Hashimoto, S.-K. Mo, Z.Q. Mao Z. Hussain, C.W. Chu, I.R. Fisher, Q. Si, Z.-X. Shen, and D.H. Lu. Observation of Universal Strong Orbital-dependent Correlation Effects in Iron Chalcogenides. *Nat. Comm.*, 6:7777, 2015.

[133] Private communication with Z.P. Yin (Rutgers). .

[134] Private communication with Ming Yi (UC Berkeley).

[135] A. Pandey, V.K. Anand, and D.C. Johnston. Large miscibility gap in the Ba($Mn_x Fe_{1x}$)$_2$As$_2$ system. *Phys. Rev. B*, 84:014405, 2011.

[136] Yu Song, Z. Yamani, C. Cao, Y. Li, C. Zhang, J. Chen, Q. Huang, H. Wu, J. Tao, Y. Zhu, W. Tian, S. Chi, R. Yu, A.H. Nevidomskyy, E. Morosan, Q. Si, and P. Dai. A Mott insulator induced near iron pnictide superconductors. *arXiv*, 1504, 2015.

[137] M. Wang, C. Zhang, X. Lu, G. Tan, H. Luo, Y. Song, M. Wang, X. Zhang, E.A. Goremychkin, T.G. Perring, T.A. Maier, Z. Yin, K. Haule, G. Kotliar, and P. Dai. Doping dependence of spin excitations and its correlations with high-temperature superconductivity in iron pnictides. *Nat. Comm.*, 4:2874, 2013.

[138] Chuck-Hou Yee and G. Kotliar. Tuning the charge-transfer energy in hole-doped cuprates. *Phys. Rev. B*, 89:094517, 2014.

[139] J. Schlappa, K. Wohlfeld, K.J. Zhou, M. Mourigal, M.W. Haverkort, V.N. Strocov, L. Hozoi, C. Monney, S. Nishimoto, S. Singh, A. Revcolevschi, J.-S. Caux, L. Patthey, H.M. Ronnow, J. van den Brink, and T. Schmitt. Spin-orbital separation in the quasi-one-dimensional Mott insulator Sr$_2$CuO$_3$. *Nature*, 485:82, 2012.

Appendix A

High Temperature Inelastic Neutron Scattering Measurements of $CaMn_2Sb_2$

We present here the high temperature inelastic neutron scattering of $CaMn_2Sb_2$ measured under the same conditions as those described in Chapter 4. Combined with other experimental or theoretical insight, these data may be able to shed some light on the origin of the weak ferromagnetic phase observed in AC magnetic susceptibility measurements of $CaMn_2Sb_2$ [31].

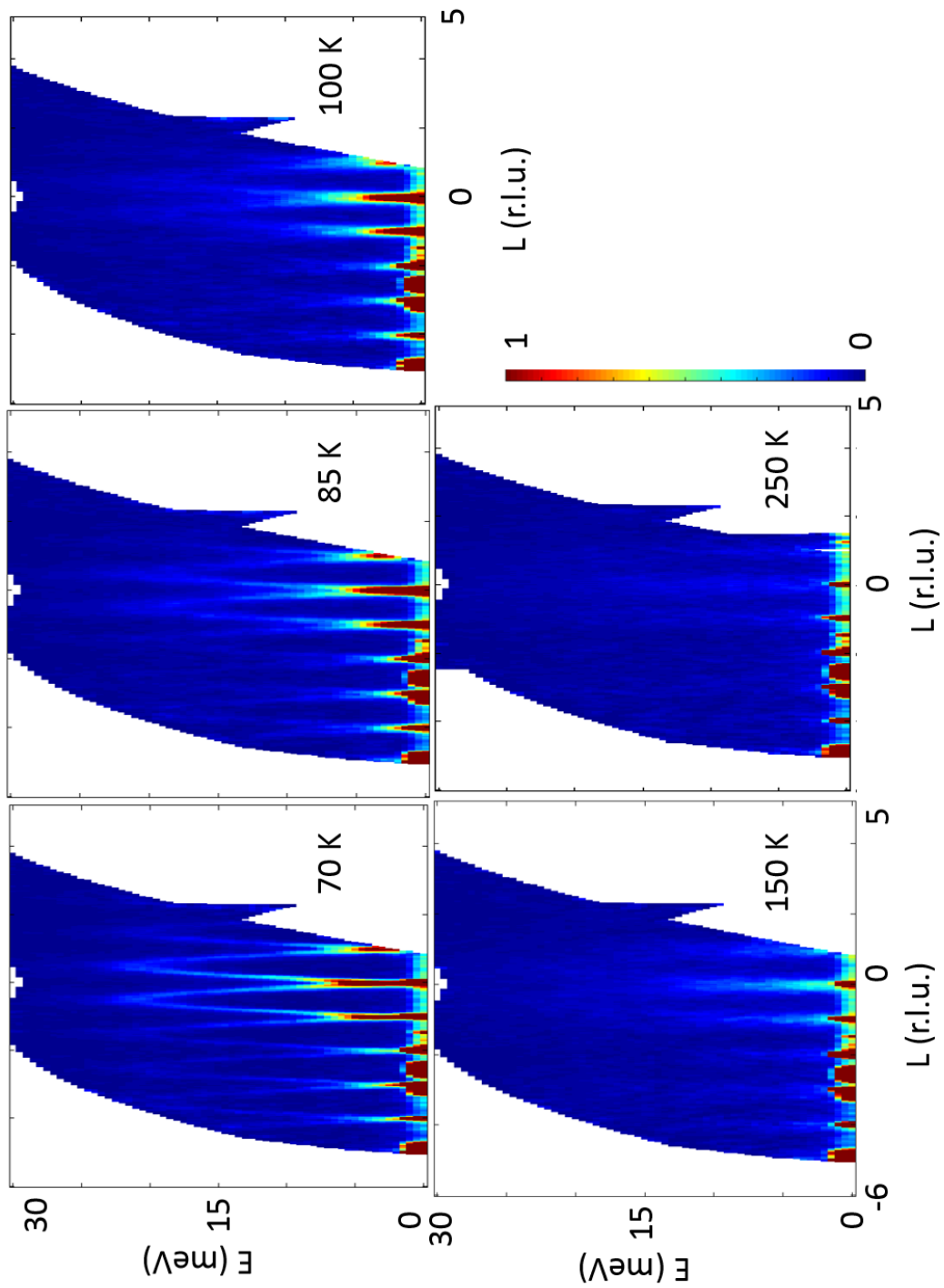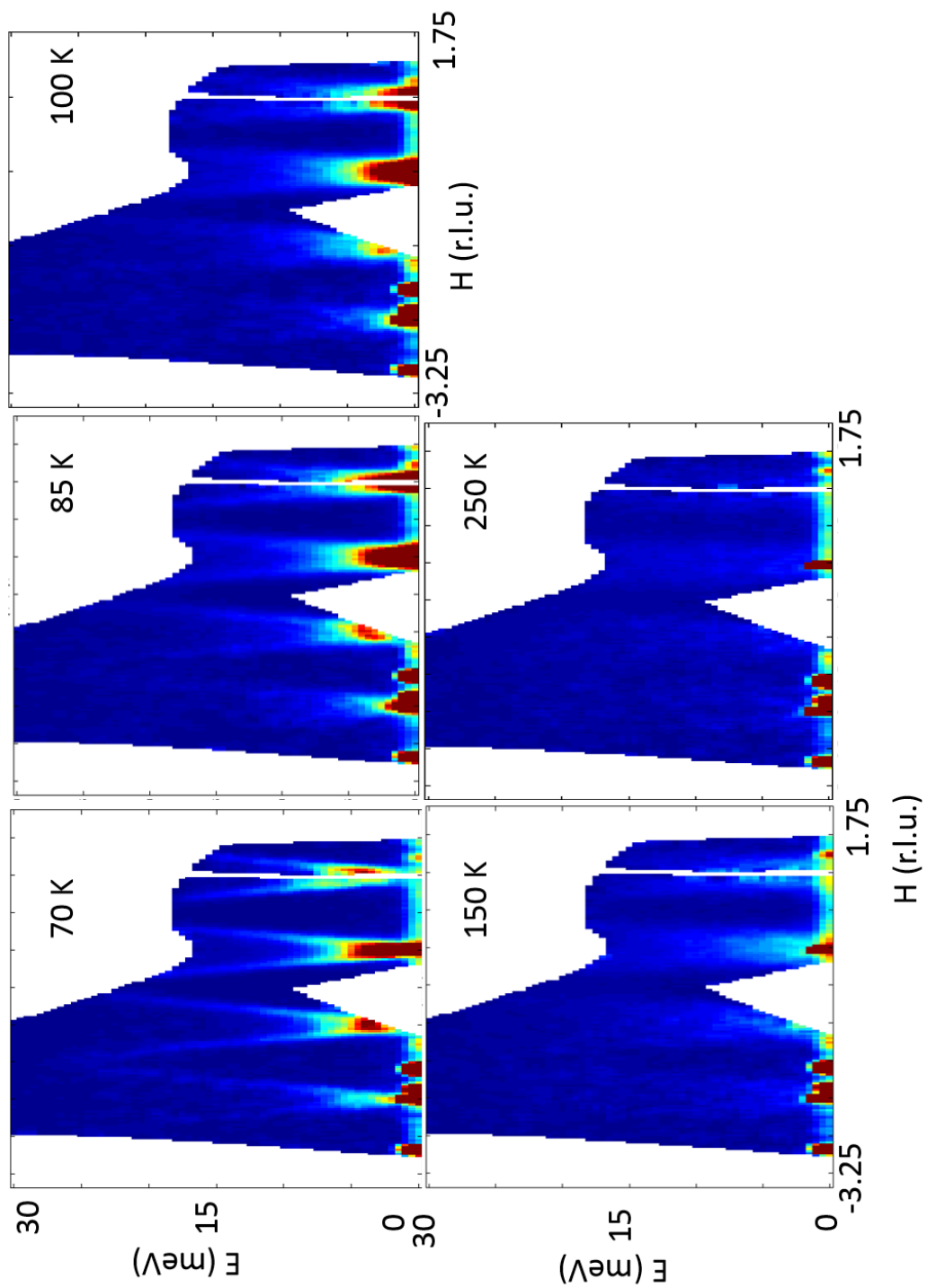Figure A.1: Contour plots of inelastic neutron scattering S(Q,L) for temperatures indicated

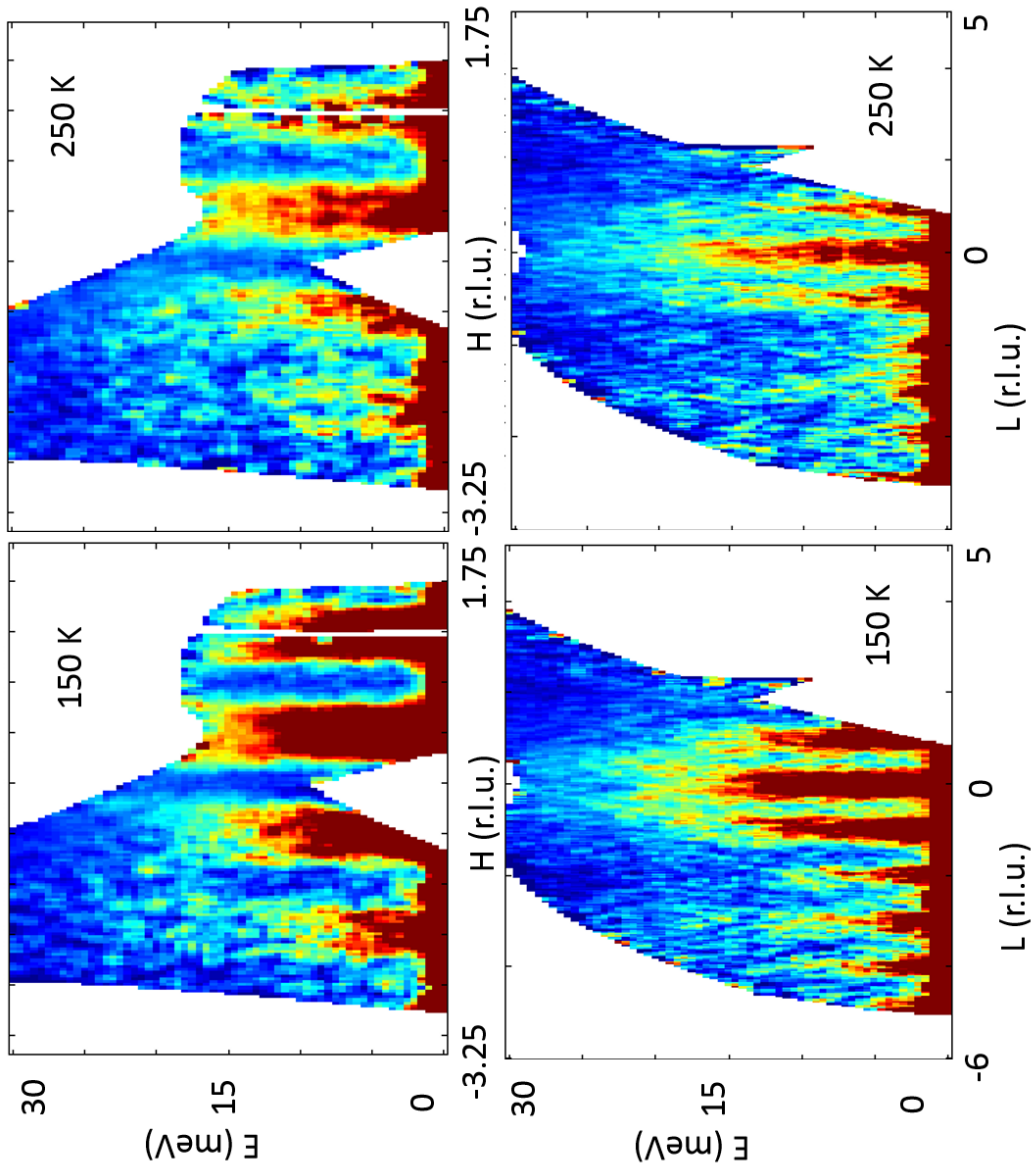Figure A.2: Contour plots of inelastic neutron scattering S(Q,H) for temperatures indicated

Figure A.3: Contour plots with reduced scale of inelastic neutron scattering S(Q, H) and S(Q,L) for temperatures indicated